Day 2: Special and advanced topics

Sondipon Adhikari, FRAeS

Zienkiewicz Centre for Computational Engineering, College of Engineering, Swansea University, Bay Campus, Swansea, Wales, UK, Email: S.Adhikari@swansea.ac.uk
Twitter: @ProfAdhikari, Web: http://engweb.swan.ac.uk/~adhikaris

SPARC Course: Metamaterial and metasandwich for energy harvesting and vibration control

March 27, 2021

Current topic in mechanical metamaterials

1. Wave propagation in mass embedded and pre-stressed hexagonal lattices
2. Bloch waves in parallelly connected periodic slender structures
3. Anisotropy tailoring in geometrically isotropic multi-material lattices
4. Buckling of 2D nano hetero structures with moire patterns
5. A fractional calculus approach to metadamping in phononic crystals and acoustic metamaterials

Composite Structures 256 (2021) 113087

Contents lists available at ScienceDirect

Composite Structures

journal homepage: www.elsevier.com/locate/compstruct

Wave propagation in mass embedded and pre-stressed hexagonal lattices

Danilo Karličić [a,b], Milan Cajić [b,*], Tanmoy Chatterjee [a], Sondipon Adhikari [a]

[a] College of Engineering, Swansea University, United Kingdom
[b] Mathematical Institute of the Serbian Academy of Sciences and Arts, Belgrade, Serbia

ARTICLE INFO

Keywords:
Embedded lattices
Attached point masses
Pre-stressed Timoshenko beams
Bloch waves
Hurty-Craig-Bampton method
Veering phenomena

ABSTRACT

This paper investigates the elastic wave propagation, mode veering, and in-plane vibration of pre-stressed hexagonal lattice embedded in an elastic medium and composed of axially loaded Timoshenko beams with attached point masses. The frequency band structure of the lattice system is obtained by solving the corresponding eigenvalue problem based on the Bloch theorem and the finite element method. The parametric study is performed by investigating the effects of the pre-stress magnitude, stiffness of elastic medium, and attached point masses on the band structure of a lattice unit cell. For simulating the free vibration behavior of the proposed lattices with different topologies, the Hurty-Craig-Bampton method is introduced to reduce the number of degrees of freedom. Based on the reduced finite element model, the natural frequencies are determined for various boundary conditions. The additional interface reduction technique, called system-level reduction, has been observed to achieve accurate results compared to that of the full model. Numerical experiments demonstrated a significant influence of the additional masses, pre-stress, and stiffness of elastic medium on Bloch waves and eigenvalues of the proposed lattice systems. The effects of different parameters on the emergence of mode veering phenomenon and band gaps are investigated in detail.

1. Introduction

A lattice material is an artificially constructed enlarged crystal with carefully tuned properties to attain desired functionality for engineering applications [1]. The concept of lattice materials is naturally inspired by concepts from crystal physics where instead of atoms, lattices are formed by a spatially periodic network of interconnected beams, rods, plates or other slender structures. Their advantage lies in the fact that their unit-cell architecture can be tailored to achieve unique mechanical, elastodynamic or acoustic properties to satisfy specific application demands that may not be achievable with conventional materials. Particularly, periodic [2] and quasi-periodic [3] hexagonal lattice structures may exhibit interesting wave propagation properties in different directions due to its anisotropy, even for shorter wavelengths [4]. Traditionally, lattice structures are classified as two-dimensional (2D) and three-dimensional (3D) lattices. The 2D lattices are formed by filling the plane from a regular polygon while 3D spatial lattices are formed by occupying the space from polyhedra. In this study, only 2D lattice structures are considered and analysed by adopting two different geometries of unit cells. The interesting wave phenomena that appear in such organized structures can lead to the advanced design of artificial materials for wave propagation control using their specific filtering, direction preference, localization or/and polarization properties. It was demonstrated in [2] that for linear waves in two-dimensional lattices, the dispersion relation depends on the orientation of a lattice vector with respect to the wavenumbers. The methods and analytical techniques used in the analysis of lattice structures apply to periodic materials in general, including phononic crystals and elastic metamaterials.

Some earlier studies demonstrated that in mechanical lattice structures there are intervals of frequencies for which there is no propagation of elastic waves [5,6]. In some of them two-dimensional periodic structures were considered with phononic band-gap phenomena studied based on the assumption of an infinite linear system and Bloch condition in such a manner that the analysis is restricted to a single unit-cell. Later in [7], plane wave propagation in hexagonal and re-entrant lattices, modelled as an assembly of rigidly connected beam elements, was investigated using the Bloch theorem and finite element method. To study the directional behaviour of hexagonal lattices for varying construction angles, two-dimensional dispersion relations were obtained and analysed. The authors devoted special attention to the determination of phase and group wave velocities. Similarly, a novel design of a honeycomb lattice geometry based on a combination of conventional and auxetic cores is proposed in [8] to improve the band

* Corresponding author.
E-mail addresses: danilo.karlicic@swansea.ac.uk (D. Karličić), mcajic@mi.sanu.ac.rs (M. Cajić).

https://doi.org/10.1016/j.compstruct.2020.113087
Received 9 July 2020; Revised 10 September 2020; Accepted 1 October 2020
Available online 10 October 2020

structure of such periodic structures. The computational analyses of bandgap properties of the proposed systems are performed by using a spectral finite element approach combined with Bloch wave boundary conditions and the use of a Wittrick-Williams method [9]. In contrast to Bloch waves analysis of general two-dimensional lattices using approximate methods such as Ritz, finite element or plane wave expansion, an exact wave-based approach is proposed in [10]. The validity of the method is demonstrated on the simple example of an aperiodic bi-material beam, and for more complex examples of the square, diamond, and hexagonal honeycomb lattices. Moreover, in [11] the authors have questioned the applicability of Bloch analysis for band structure investigation of discrete systems with asymmetry. The conclusions from solid-state physics claim that extremum of frequencies exclusively occurs on the boundary of the irreducible Brillouin zone. However, using the new transformation technique and asymmetrical counter-example of honeycomb lattice, the authors have shown that this is not strictly valid for a general wave propagation problem.

Investigating the vibration behaviour of periodic and quasi-periodic lattice beam structures is important for their complete dynamic analysis and potential design of vibration insulators [12–14]. One of the popular methods for analyzing dynamic systems is component mode synthesis (CMS), which is essentially a physics-based sub-structuring and model reduction technique. In general, it operates by modelling the sub-components individually and their reduced dynamic models are assembled to form a global system. Thus, it captures the global dynamic behaviour within a significantly reduced computational effort. This is discussed later in detail (Section 3). The literature related to CMS methods is well developed and they have been utilized to solve structural dynamic problems over the past few decades. Extensive reviews of CMS methods can be found in [15,16]. However, their usefulness for analyzing periodic structures has only been explored recently. Few applications of CMS in analyzing periodic structures are as follows: Dynamics of two gradient honeycomb structure was investigated in [17] by considering the full-scale finite element model with CMS sub-structuring to determine the frequency response functions (FRF). The wave finite element (WFE) and Craig-Bampton method were used for assessing the harmonic response of coupled mechanical systems that involve one-dimensional periodic structures and coupling elastic junctions in [18]. A numerical approach was proposed in [19] to compute the dynamic response of periodic structures with cyclic symmetry, and assemblies made up of periodic structures. An efficient topology optimization method for periodic structures with static condensation was developed in [20] such that the macrostructure is identically partitioned into several scale-related sub-structures represented by the zero contours of a level set function.

The vibration transmission and isolation properties of the tri-chiral lattice structure was studied in [21] for the uniform and gradient types of geometry parameters. The finite element method in conjunction with the Bloch theorem was employed to analyse the band structure and identify the corresponding stop and passbands. Moreover, by considering the full finite element model of the lattice structure, the harmonic response is estimated and significant attenuation in the vibration transmission is found with the width corresponding to the frequency range of bandgap region. In [22], the authors observed an important problem of the in-plane impact and dynamic response of the gradient hexagonal lattice by studying the deformation modes and energy absorption capacity in details. By considering the strain gradient elasticity theory and homogenization technique, the band buckling and vibration of a two-dimensional triangular lattice and a sandwich structure based on the Euler–Bernoulli and Timoshenko beam theories were studied in [23]. It is found that the bending rigidity, critical buckling load and natural frequency are strongly affected by the lattice microstructure properties and these dependencies are captured by the generalized simple beam model. On the other hand, in [24] the authors have analysed the base excited beam-like periodic lattice structure with internal resonators, where the model exhibits high stiffness and damping. It was demonstrated that for the specially designed geometry based on chiral topology, the system can be in resonance at selected frequencies with vibration attenuation capabilities obtained over desired frequency ranges.

Investigations in the previously mentioned studies mostly relied on dynamic models and Bloch wave analysis of bandgap and directional behaviour properties of cellular lattices. The other methodologies to study the dynamic behaviour of periodic solids includes homogenization techniques, which yield an equivalent continuum representation with the information about the properties and geometry of the unit cell. Among these techniques, there are several approaches but two major directions applied in lattice structures include numerical multi-scale methods [25] and asymptotic expansion methods [26,27]. Another class of lattice structures that excludes Bloch analysis belongs to strongly nonlinear periodic lattices, where suitable methods for nonlinear differential equations are used to calculate amplitude-dependent dispersion curves [28,29]. The hierarchical [30] and undulated [31] structural lattices are also studied in the literature using finite element method and Bloch theory [31]. However, the aforementioned analyses are out of the scope of this research and are not detailed here.

Pre-stress effect introduced into the lattice beam elements can boost the bandgap properties by controlling the dispersion characteristics through the alternation of the structural effective stiffness. Such pre-stressed beams assembled in the hexagonal lattice are investigated in [32], where finite element method and Bloch's theorem are employed to generate dispersion curves. This effect is also examined on dispersion diagrams for the axial and flexural waves in quasi-periodic infinite beam structures [33]. It was noticed that a tensile axial pre-stress causes a length reduction of passbands by leaving the length of stop-band intervals almost unaltered. More general analysis of periodic and quasi-periodic structures can be found in [34–36].

The literature on periodic Timoshenko beams based lattice structures without [9,37] and with pre-stress [38,36,39] is sparse and as per the author's knowledge, there is no work addressing the problem of lattice structures with pre-stressed Timoshenko beams embedded in elastic medium and with attached point masses. A few studies investigated the veering of dispersion branches in waveguides [40] and lattice structures [4,7,41–43]. According to [44], mode localization phenomenon has often been observed in periodic structures [45–47], where small disturbances in the periodicity may lead to the confinement of one or more vibration modes to some small regions. Mode veering can also occur in non-conservative mechanical systems with dissimilar components [48,49]. Moreover, in [50], the authors studied the emergence and disappearance of veering, cut-off/cut-on, and branch overtaking phenomena in periodic structures with various topologies representing microtubule-like networks. They also investigated the effect of damping and analysed both in-plane and out-of-plane motions as well as dependence between their modes. Very recently, close mode approximation in near-periodic structures was investigated in [51]. Therefore, the analysis of mode veering phenomenon is significant for practical applications since mode localisation can cause unexpectedly high levels of response in periodic structures, as shown in the first experimental study [52]. In general, this study shows that this phenomenon plays an important role in the analysis of dispersion curves as demonstrated on the frequency band structure diagrams, which are determined for the reduced model of the lattice structures. Some studies [4] reported that the mode veering phenomenon comes from the weak modal coupling in the system but such kind of analysis is not elaborated in this work.

Motivated by the lack of studies that address more complex lattice systems, we have sought to study the dynamic and band structure properties of the hexagonal lattice systems embedded in the elastic medium with attached point masses and beam elements subjected to pre-load at

the same time. The finite element method and Bloch theorem are utilized to determine dispersion curves while finite element and reduction technique are used for dynamic analysis. The suggested design results in different band structure properties and dynamic behaviour of hexagonal lattices that can be tuned only by changing the parameters such as the value of point masses, pre-load magnitude or stiffness of the surrounding medium and without changing the topology of the lattice itself. This is demonstrated through a comprehensive parametric study, where the effects of different parameters on the appearance or disappearance of higher/zero-frequency band gaps and mode veering are discussed in details. This paper is organized as follows: the mechanical model of a hexagonal structure composed of interconnected Timoshenko beams surrounded by an elastic medium and included pre-stress effect and point masses is presented in Section 2. The procedure for the Bloch wave solution and the finite element method to obtain the dispersion relations is outlined. The methodology to generate the the model for dynamic analysis of the proposed system with model reduction technique is given in Section 3. The verification study and effect of lattice angle, point masses and pre-stress on dispersion characteristic of the system is discussed in Section 4. Finally, Section 5 summarizes the main contributions and results of this work.

2. Problem formulation

2.1. Mechanical model of a lattice structure

To analyse the free in-plane wave propagation in a two-dimensional periodic structure, a hexagonal type of lattice embedded in an elastic Winkler medium is considered as shown in Fig. 1(a). The presented hexagonal structure is formed by a periodically distributed three-pointed star-like unit cells consisting of three rigidly connected pre-stressed beams with attached point masses Fig. 1(b). The pre-stress is realized through linear springs placed in the beam's axial direction, which possess compressive or tensile properties with the value N_0. The proposed elastic medium is modelled as a Winkler's medium and it is represented by the parallelly distributed springs with stiffnesses in the axial k_u and transverse k_w directions of the beam. Here, the Timoshenko beam model is adopted by taking into account the shear effects and rotational inertia. The local beam coordinates are adopted in such a way that the x-coordinate is considered along the length of the beam and the z-coordinate is considered along the thickness direction.

Additional details of the geometrical model of a hexagonal periodic structure unit cell, with its characteristic dimensions and vectors, are given in Fig. 2(a). The internal angle of a unit cell is defined as θ. Therefore, by changing the internal angle θ, a hexagonal lattice structure can be transformed into the re-entrant one, where θ can be taken as a negative value. The main geometrical characteristic of the unit cell is the wall's slenderness ratio defined as $\beta = d/L$. In the literature, the regular hexagonal and re-entrant lattice structures are having internal angles of $\theta = 30^\circ$ and $\theta = -30^\circ$, respectively. As stated before, the hexagonal lattice structures are based on periodically distributed unit cells, where connection nodes are known as lattice points. The vectors defining primitive unit cells and their connection with other unit cells are called basis vectors $(\mathbf{e}_1,\ \mathbf{e}_2)$, which also defines the direct lattice space [7], as given in Fig. 2(a). Therefore, the problem of wave propagation in periodic lattice structures can be reduced to a typical unit cell problem by introducing the periodic boundary conditions according to the Bloch theorem. For the unit cell of the hexagonal lattice structure with positive internal angle θ the basis vectors $(\mathbf{e}_1,\ \mathbf{e}_2)$ are defined in local Cartesian coordinates with unit vectors $(\mathbf{i}_1,\ \mathbf{i}_2)$ as

$$\begin{aligned}\mathbf{e}_1 &= (L\cos\theta, L(1+\sin\theta))^T,\\ \mathbf{e}_2 &= (-L\cos\theta, L(1+\sin\theta))^T.\end{aligned} \tag{1}$$

As mentioned before and based on concepts from the solid-state physics, the lattice points with the corresponding base vectors $(\mathbf{e}_1,\ \mathbf{e}_2)$ define the direct lattice space, which determines the periodic structure. For such given direct lattice space, one can define the reciprocal lattice space based on the following relation

$$\mathbf{e}_i \cdot \mathbf{e}_j^* = 2\pi\delta_{ij}, \tag{2}$$

where $\mathbf{e}_j^*$ represents the basis vector of the reciprocal lattice and δ_{ij} denotes Kronecker delta. For the proposed hexagonal lattice structure and unit cell architecture, the reciprocal lattice vectors takes the following form

$$\begin{aligned}\mathbf{e}_1^* &= \left(\frac{1}{2L\cos\theta}, \frac{1}{2L(1+\sin\theta)}\right)^T,\\ \mathbf{e}_2^* &= \left(-\frac{1}{2L\cos\theta}, \frac{1}{2L(1+\sin\theta)}\right)^T.\end{aligned} \tag{3}$$

In the following sections, the applicability of the proposed concepts will be demonstrated by introducing the Bloch theorem and related periodic boundary conditions.

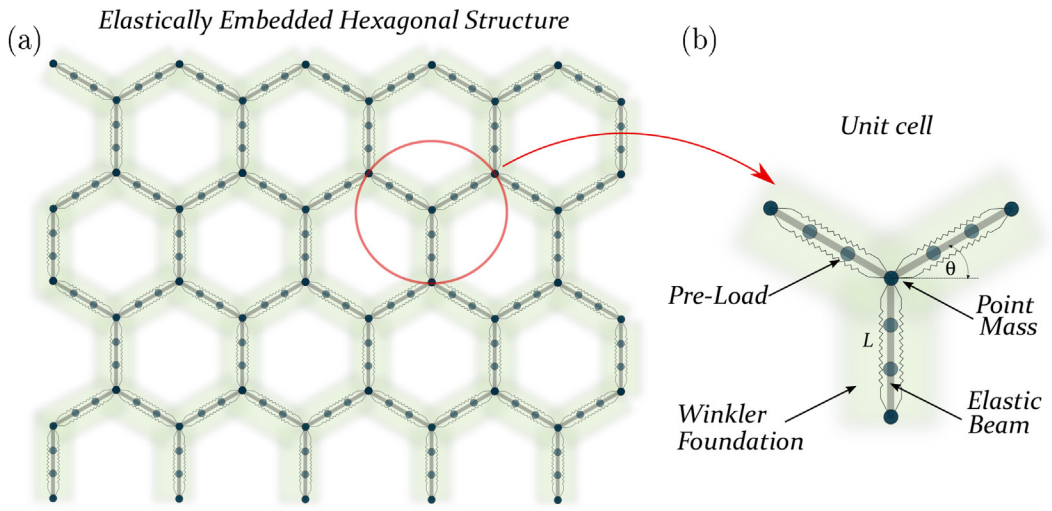

Fig. 1. Mechanical model of a hexagonal lattice composed of Timoshenko beams with attached point masses and embedded in an elastic medium, a) two-dimensional hexagonal lattice, and b) three-pointed star shape of a unit cell.

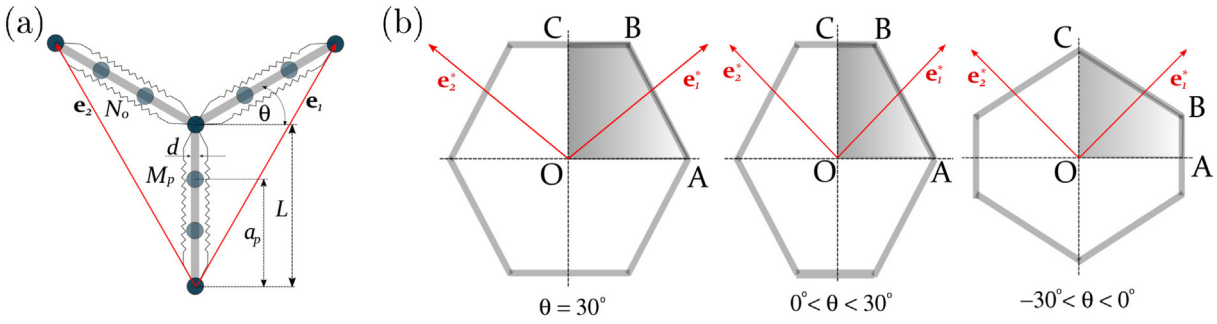

Fig. 2. The geometrical characteristics of a unit cell and the first Brioullin zone.

2.2. Bloch's theorem

By assuming the propagation of an elastic wave through an infinite periodic lattice structure formed by tessellating the unit cell along the basis vectors $(\mathbf{e}_1,\ \mathbf{e}_2)$ and connected through lattice points, this kind of an infinite structure can be reduced by introducing the concept of Bloch theorem and the primitive unit cell. In order to select the proper unit cell, we are going to use the methodology developed for elastic periodic structures [10,7], where position of the primitive unit cell is determined by the vector $\mathbf{s} = \mathbf{r} + n\mathbf{e}_1 + m\mathbf{e}_2$ placed in the plane of a lattice structure. The set of numbers (n, m) taking the integer values defines the number of unit cells placed along the basis vectors $(\mathbf{e}_1,\ \mathbf{e}_2)$. Therefore, the vector $\mathbf{s}$ is going from the $(0, 0)$ unit cell until the unit cell defined as (n, m). The vector $\mathbf{r}$ is related to the position of any point inside the reference primitive unit cell defined as $(0, 0)$. Now, according to the Bloch theorem, introducing the displacement vector $\mathbf{w}(\mathbf{r}) = \mathbf{w}_r e^{i\omega t - \mathbf{k}\cdot\mathbf{r}}$ at some arbitrary point inside the reference unit cell corresponds to the wave that propagates at frequency $\omega(rad/s)$. It should be noted that $\mathbf{w}_r$ is related to the wave amplitude and $\mathbf{k}$ is the wave vector of plane wave. By considering the chosen unit cell determined by the set of numbers (n, m), where n and m are the numbers of unit cells considered in the $\mathbf{e}_1$ and $\mathbf{e}_2$ directions, respectively, the displacement vector of an arbitrary point inside the chosen unit cell is defined as

$$\mathbf{w}(\mathbf{s}) = \mathbf{w}(\mathbf{r})e^{\mathbf{k}\cdot(\mathbf{s}-\mathbf{r})} = \mathbf{w}(\mathbf{r})e^{\mathbf{k}\cdot(n\mathbf{e}_1+m\mathbf{e}_2)}, \tag{4}$$

where $\mathbf{k}\cdot(n\mathbf{e}_1 + m\mathbf{e}_2) = nk_1 + mk_2$.

According to the Bloch's theorem [53], amplitude of a propagating wave of a lattice structure without attenuation is independent of a unit cell location within the periodic system. Therefore, elastic wave propagation properties of a periodic system can be completely described by a single representative unit cell with corresponding boundary conditions. Therefore, application of Bloch's theorem can save significant computational efforts and it can be viewed as a kind of (physics-based) model reduction technique applicable to ideally periodic structures. According to Eq. (4), wavenumbers $k_i,\ (i = 1, 2)$ are complex values given as $k_i = \phi_i + i\varepsilon_i,\ (i = 1, 2)$, where the real part ϕ_i is related to the amplitude attenuation due to wave propagation from one unit cell to another. The imaginary part ε_i is related to phase changes across cells and it is known as the phase constant. When analysing the Bloch waves, it is assumed that they are propagating without attenuation since the real part ϕ_i is set to 0. Further, it will be shown how Bloch's theorem is used for setting the periodic boundary conditions in the finite element (FE) model of a unit cell.

To analyse the elastic wave propagation without attenuation, values of the wave vector $\mathbf{k}$ are considered to be imaginary with its values varied within the first Brillouin zone. The concept of Brillouin zone is introduced by considering the reciprocal periodic lattice determined by the vectors defined in Eq. (3), which restricts the value of the wave vector $\mathbf{k}$. According to [7,54], the free wave propagation can be reduced to an eigenvalue problem with the frequency of wave propagation determined by varying the parameters $(k_1,\ k_2)$. The relation between ω and $(k_1,\ k_2)$ is known as dispersion surface, where each surface is related to a different mode of elastic wave propagation through the periodic structure. To analyse the wave propagation in hexagonal and re-entrant lattice structures, the relation between frequency and wave vectors will be determined by considering the Timoshenko beam element and periodic boundary conditions introduced through the Bloch's theorem.

2.3. The equations of motion of an embedded Timoshenko beam

The partial differential equations of motion of the elastically embedded and pre-stressed Timoshenko beam with attached point masses are derived by using the Hamilton's principle. Based on the displacement fields of Timoshenko beam and elastic constitutive relation given in [55] the variations of kinetic $\tilde{\delta}K$ and potential $\tilde{\delta}U$ energies are given as

$$\delta K = \int_0^L \left[\rho A\dot{u}\tilde{\delta}\dot{u} + \rho I\dot{\psi}\tilde{\delta}\dot{\psi} + \rho A\dot{w}\tilde{\delta}\dot{w} + \sum_{p=1}^{M} M_p\delta(x-a_p)\dot{u}\tilde{\delta}\dot{u} + \sum_{p=1}^{M} M_p\delta(x-a_p)\dot{w}\tilde{\delta}\dot{w}\right]dx, \tag{5}$$

$$\delta U = \int_0^L \left[EA\frac{\partial u}{\partial x}\tilde{\delta}\frac{\partial u}{\partial x} + EI\frac{\partial \psi}{\partial x}\tilde{\delta}\frac{\partial \psi}{\partial x} + GAk_s\left(\psi - \frac{\partial w}{\partial x}\right)\tilde{\delta}\left(\psi - \frac{\partial w}{\partial x}\right) + k_w w\tilde{\delta}w + k_u u\tilde{\delta}u - N_0\frac{\partial w}{\partial x}\tilde{\delta}\frac{\partial w}{\partial x}\right]dx, \tag{6}$$

where $\tilde{\delta}$ is the variation operator and $\delta(x - a_p)$ is the Dirac delta function defining the position of masses on the beam.

Using Eq. (5) and Eq. (6) and Hamilton's principle yields

$$\int_{t_1}^{t_2} (\tilde{\delta}K - \tilde{\delta}U)dt = 0, \tag{7}$$

After partial integration process, the system of partial differential equations for longitudinal and transverse vibrations is obtained as

$$\left[\rho A + \sum_{p=1}^{M} M_p\delta(x-a_p)\right]\ddot{u} - EA\frac{\partial^2 u}{\partial x^2} + k_u u = p(x,t) \tag{8}$$

$$\left[\rho A + \sum_{p=1}^{M} M_p\delta(x-a_p)\right]\ddot{w} + GAk_s\left(\frac{\partial \psi}{\partial \psi} - \frac{\partial^2 w}{\partial x^2}\right) + k_w w + N_0\frac{\partial^2 w}{\partial x^2} = q(x,t) \tag{9}$$

$$EI\frac{\partial^2 \psi}{\partial x^2} - GAk_s\left(\psi - \frac{\partial w}{\partial x}\right) - \rho I\ddot{\psi} = 0 \tag{10}$$

where $u(x, t)$ is the axial displacement, $w(x, t)$ is the transverse displacement and $\psi(x, t)$ is rotation of the cross section. Here, the symbol $\dot{(\cdot)}$ is used to represent $\partial(\cdot)/\partial t$. Material characteristics of the proposed beam model are defined by mass density ρ, modulus of elasticity E, shear

modulus $G = E/(2(1+\nu))$ and Poisson ratio ν. The width of a beam is defined with h. The pre-stress of a lattice structure is introduced through axial springs connected to each beam in the lattice and it is denoted by N_0. The stiffness of Winkler's type elastic medium is introduced in x- and z-directions and denoted by k_u and k_w, respectively. The shear correction factor k_s is adopted in the following form $k_s = 10(1+\nu)/(12+11\nu)$, [10]. In this study, the influence of external axial $p(x,t)$ and transverse $q(x,t)$ excitation forces is neglected.

2.4. The finite element model of the unit cell

One of the most applied structural analysis techniques is the finite element method that is often used to obtain the stiffness matrix of the beam. Here, the FE method is introduced to discretize the motion equations of a unit cell with Bloch boundary conditions. The unit cell is modelled as an assembly of rigidly connected Timoshenko beams in the form a three-pointed star, where each limb is represented by a single beam element with attached point masses and surrounded by an elastic medium. Adopted slender ratio starts from $\beta = 1/15$ representing a thick beam model for which effects of shear forces and rotary inertia should be taken into account. Typical finite element models for Timoshenko beam theory are given in [55,56], where approximations of displacements $u(x,t)$ and $w(x,t)$ and rotation $\psi(x,t)$ are given in the following form

$$u(x,t) = \sum_{j=1}^{6}\Gamma_j(x)q_j(t), \quad w(x,t) = \sum_{j=1}^{6}\Lambda_j(x)q_j(t), \\ \psi(x,t) = \sum_{j=1}^{6}\Theta_j(x)q_j(t), \tag{11}$$

where $\Gamma_j(x), \Lambda_j(x)$ and $\Theta_j(x), (j = 1,2,\ldots,6)$ are the shape functions for six nodal degrees of freedom of Timoshenko beam element given as $\mathbf{q}(t) = [u_1, w_1, \psi_1, u_2, w_2, \psi_2]^T$. The mode shape functions are adopted from [56] and are given in Appendix A. By considering the equations of motion of Timoshenko beam Eqs. (8)–(10), energy variation Eqs. (10)–(7) and approximation of displacements and rotation Eq. (11), the FE model is defined as

$$\mathbf{M}^e\ddot{\mathbf{q}}^e + \mathbf{K}^e\mathbf{q}^e = \mathbf{f}^e, \tag{12}$$

where $\mathbf{M}^e$ and $\mathbf{K}^e$ are mass and stiffness matrices of the beam element while $\mathbf{q}^e$ and $\mathbf{f}^e$ are the corresponding element displacement and force vector, respectively.

By considering a typical unit cell of a hexagonal and re-entrant lattice, the model represents a frame structure where mass and stiffness matrices $(\mathbf{M}^e, \mathbf{K}^e)$ of the beam element are obtained in local coordinates but should be transformed into the global ones. The relations between the local and global mass $\mathbf{M}_g^e$ and stiffness $\mathbf{K}_g^e$ matrices are given by the transformation matrix in the following form

$$\mathbf{M}_g^e = \mathbf{T}^T\mathbf{M}^e\mathbf{T}, \quad \mathbf{K}_g^e = \mathbf{T}^T\mathbf{K}^e\mathbf{T}, \tag{13}$$

in which the transformation matrix is formed as

$$\mathbf{T} = \begin{pmatrix} \mathbf{T}_0 & \mathbf{0} \\ \mathbf{0} & \mathbf{T}_0 \end{pmatrix}, \tag{14}$$

and

$$\mathbf{T}_0 = \begin{pmatrix} \cos\varphi & \sin\varphi & 0 \\ -\sin\varphi & \cos\varphi & 0 \\ 0 & 0 & 1 \end{pmatrix}, \tag{15}$$

where $\mathbf{T}_0$ is the rotation matrix and $\varphi$is the angle between the local and global axial directions of the beam as shown in [55]. The three beam model of the chosen unit cell (n,m), connected under different angles according to the local coordinate system, can be assembled by considering matrices from Eq. (13) as follows

$$\mathbf{K} = \overset{n_{ele}}{\underset{e=1}{\mathscr{A}}}\mathbf{K}_g^e, \quad \mathbf{M} = \overset{n_{ele}}{\underset{e=1}{\mathscr{A}}}\mathbf{M}_g^e, \tag{16}$$

where $\mathbf{M}$ and $\mathbf{K}$ are the global mass and stiffness matrices of the unit cell and n_{ele} is the number of elements in the unit cell. Thus, the FE model of a unit cell is given as

$$\mathbf{M}\ddot{\mathbf{q}} + \mathbf{K}\mathbf{q} = \mathbf{f}. \tag{17}$$

The number of elements (n_{ele}) chosen in discretization of the unit cell is defined in the numerical section.

2.5. Dispersion relations – Periodic boundary conditions

By using the previously described concept, a corresponding eigenvalue problem can be established whose solution gives dispersion curves i.e. frequencies in terms of wavenumbers. Dispersion analysis enables one to detect band gaps at corresponding ranges of frequencies. Therefore, by considering the Bloch wave propagation in a unit cell described by the FE model given in Eq. (17), the dispersion curves can be generated as the solution of the following eigenvalue problem. Introducing harmonic solution $\mathbf{q}(x,t) = \mathbf{q}(x)e^{i\omega t}$ into Eq. (17), yields

$$(\mathbf{K} - \omega^2\mathbf{M})\mathbf{q} = \mathbf{0}, \tag{18}$$

where the force vector $\mathbf{f}$ of interaction between cells is neglected and ω is the frequency of free wave propagation. The vector $\mathbf{q}$ of nodal displacements is given in the following form

$$\mathbf{q} = \{\mathbf{q}_0 \quad \mathbf{q}_1 \quad \mathbf{q}_2 \quad \mathbf{q}_i\}^T, \tag{19}$$

where $\mathbf{q}_0, \mathbf{q}_1$, and $\mathbf{q}_2$ are the vectors of nodal displacements at end nodes of the unit cell. The nodal displacements in vector $\mathbf{q}_i$ are related to degrees of freedom of internal nodes of the unit cell. The absence of external forces in internal nodes simplifies the analysis by considering the free wave propagation, which yields a significant reduction in computation time. Based on the Bloch's theorem, the periodic boundary conditions related to the unit cell are applied on the end nodes displacements as follows

$$\mathbf{q}_1 = e^{k_1}\mathbf{q}_0, \quad \mathbf{q}_2 = e^{k_2}\mathbf{q}_0. \tag{20}$$

By using the Eq. (20), transformation matrix can be applied to the global vector of nodal displacements as

$$\mathbf{q} = \mathbf{T}_b\mathbf{q}_r, \tag{21}$$

where the global vector of nodal displacements is reduced to $\mathbf{q}_r = \{\mathbf{q}_0 \quad \mathbf{q}_i\}^T$, and matrix $\mathbf{T}_b$ is defined as

$$\mathbf{T}_b = \begin{bmatrix} \mathbf{I} & \mathbf{0} \\ \mathbf{I}e^{k_1} & \mathbf{0} \\ \mathbf{I}e^{k_2} & \mathbf{0} \\ \mathbf{0} & \mathbf{I} \end{bmatrix}. \tag{22}$$

Inserting Eq. (21) into Eq. (18) and pre-multiplying the resulting equation with the Hermitian (complex conjugate) transpose matrix $\mathbf{T}_b^H$, yields

$$(\mathbf{K}_r(k_1,k_2) - \omega^2\mathbf{M}_r(k_1,k_2))\mathbf{q}_r = \mathbf{0}, \tag{23}$$

where mass and stiffness matrices are now given as

$$\mathbf{M}_r(k_1,k_2) = \mathbf{T}_b^H\mathbf{M}\mathbf{T}_b, \\ \mathbf{K}_r(k_1,k_2) = \mathbf{T}_b^H\mathbf{K}\mathbf{T}_b. \tag{24}$$

The transformation matrix for the force vector can be found in a similar manner (see [4,10]).

By solving the eigenvalue problem given in Eq. (23) and varying the values of wave numbers k_i, $(i = 1,2)$ within the first Brillouin zone, obtained results can be displayed in the form of dispersion surfaces $\omega = \omega(k_1,k_2)$. However, computational effort can be substan-

tially reduced by exploiting the symmetry properties of the first Brillouin zone and a unit cell. From the physical viewpoint, the geometrical shape of the first Brillouin zone is directly dependent on the internal lattice angle θ and it can form a uniquely defined primitive cell in the reciprocal space determined by the vectors $(\mathbf{e}_1^*, \mathbf{e}_2^*)$. One can find more details about the symmetry and Brillouin zone structure in [57,58]. The reduced part of the first Brillouin zone is known as the irreducible Brillouin zone (IBZ), where for solution of the eigenvalue problem and determination of dispersion curves one should consider values of wavenumbers along the contours only. For hexagonal and re-entrant lattices, the IBZ and its contours are given as shaded regions denoted by $O-A-B-C-O$ (see Fig. 2(b)). However, for the regular hexagonal lattice there is one additional symmetry whose IBZ is given in the first part of (Fig. 2(b)) with its reduced contours $O-B-C-O$. In the following, the formation of a band structure is based on the restricted zone of the IBZ in the reciprocal lattice frame, where coordinates of boundary points are given in Table 1, [9].

To determine the band structure diagrams, values of the wave vector defined in the reciprocal space as $\mathbf{k} = k_1\mathbf{e}_1^* + k_2\mathbf{e}_2^*$, are varied along the contour $O-A-B-C-O$. The eigenvalue problem Eq. (23) is used to detect bandgap regions. The passbands are frequency ranges for which the lattice structure behaves as a wave-guide. On the other hand, the band gap regions are ranges of frequencies at which propagation of waves is stopped. The importance of determining the band structure of lattice structures lies in potential design of wave-filters.

The eigenvalue problem from Eq. (23) is solved by implementing the MATLAB function eig() to obtain corresponding dispersion curves. Also, the mass and stiffness matrices of the unit cells for the whole structure are implemented in MATLAB to analyse the free wave propagation and in-plane vibrations of the embedded lattice structure with attached masses. The complete set of the surface $\omega(k_1, k_2)$ is denoted as the phase constant surface or dispersion surface. The number of dispersion surfaces directly depends on the size of the eigenvalue problem.

3. Dynamic analysis of the lattice structure

In this section, our goal is to (i) reduce the model of periodic lattice structures, (ii) solve the eigenvalue problem and analyse the band structure, and (iii) investigate the resulting mode veering phenomena due to identical/close modes. The presented lattice structure is modelled as a system of periodically distributed unit cells in two directions forming a rectangular plate with corresponding boundary conditions. The results obtained in this section are presented in the form of eigenvalue curves for the in-plane vibration. In these diagrams one can also detect band gap regions. In the previous section, the main assumption was that the hexagonal structure should be considered long enough to apply the Bloch's theorem for detection of band gaps. As a consequence, such periodic structural systems may often consist of with thousands or even millions of degrees of freedom (DOFs) obtained by using the FE method. Analysing the global FE model may render the numerical computation process to be time-intensive, if not prohibitive. Therefore, the Hurty-Craig-Bampton method (also referred to as fixed-interface CMS) is employed here, which reduces the initial number of DOFs of the global FE model by dividing into sub-components. Thus, the intention is to capture the overall dynamic behaviour of the full FE model by an equivalent reduced model by entailing significantly less computational cost. Few recent contributions of CMS include [15,59–61].

3.1. Hurty-Craig-Bampton model reduction

The Hurty-Craig-Bampton model reduction technique is based on sub-structuring the initial (assembled) system into different sub-components and analysing the interior dynamics by considering truncated set of normal modes (eigenvectors), as shown in [62,63]. Moreover, the interface between (internal) sub-structural components is retained without any reduction. By using this fixed-interface model reduction framework, the presented hexagonal structure is divided into two parts as shown in Fig. 3, where the red coloured circles denote the interface between two sub-structures while the grey coloured circles represent the boundary conditions. The initial step of the Hurty-Craig-Bampton technique is FE discretization of the equation of motion for p^{th} sub-structure, which gives

$$\mathbf{M}_p\ddot{\mathbf{q}}_p + \mathbf{K}_p\mathbf{q}_p = \mathbf{f}_p, \tag{25}$$

where $\mathbf{M}_p$ and $\mathbf{K}_p$ are the mass and stiffness matrices of sub-structures, $\mathbf{q}_p$ is the nodal displacement vector and $\mathbf{f}_p$ is the forcing vector. Next step is to express the system Eq. (25) into interior and interface (or boundary) DOFs, which is given as

$$\begin{bmatrix} \mathbf{M}_{ii,p} & \mathbf{M}_{ib,p} \\ \mathbf{M}_{bi,p} & \mathbf{M}_{ii,p} \end{bmatrix} \begin{bmatrix} \ddot{\mathbf{q}}_{i,p} \\ \ddot{\mathbf{q}}_{b,p} \end{bmatrix} + \begin{bmatrix} \mathbf{K}_{ii,p} & \mathbf{K}_{ib,p} \\ \mathbf{K}_{bi,p} & \mathbf{K}_{ii,p} \end{bmatrix} \begin{bmatrix} \mathbf{q}_{i,p} \\ \mathbf{q}_{b,p} \end{bmatrix} = \begin{bmatrix} \mathbf{0} \\ \mathbf{f}_{b,p} \end{bmatrix}, \tag{26}$$

The subscripts b and i in the above equations are related to the boundary (or interface) and internal DOFs of the mass and stiffness matrices as well as displacement and force vectors. Following the methodology proposed in [62,59], the component modes are formed by determining the static responses corresponding to the internal DOFs, where one of the interface DOF is set as unit displacement while the other DOFs are fixed. From the unit static responses, the set of component modes is formed as

$$\begin{aligned} &\mathbf{q}_{i,p} = -\mathbf{K}_{ii,p}^{-1}\mathbf{K}_{ib,p}, \\ &\mathbf{q}_{b,p} = \mathbf{I}, \quad \rightarrow \quad \mathbf{\Psi}_p = \begin{bmatrix} -\mathbf{K}_{ii,p}^{-1}\mathbf{K}_{ib,p} \\ \mathbf{I} \end{bmatrix}. \end{aligned} \tag{27}$$

Consideration of this statically reduced model gives sufficiently accurate solutions for the system under static deformation. The obtained component modes ensure a basis for achieving static condensation that holds each interface DOFs and eliminates interior DOFs from the model. The main consequence is that the original physical interface DOFs of a sub-structure are retained, so the system can still be reassembled easily. If only statically obtained component modes are used, they cannot be applied for accurate analysis of the dynamic behaviour of internal DOFs. To extend the analysis and overcame this restriction, the set of component modes should be augmented for the set of dynamical modes that are obtained by fixing the interface DOFs. Taking into consideration the harmonic solution for the internal DOFs from Eq. (26) gives the following eigenvalue problem

Table 1
The boundary points of the irreducible Brillouin zone of hexagonal and re-entrant lattice structures.

Type of periodic structure	Hexagonal structure $0^\circ \leqslant \theta < 90^\circ$	Re-entrant structure $-30^\circ < \theta \leqslant 0^\circ$
O	$(0,0)$	$(0,0)$
A	$2\pi(1/(4\sin^2\phi), -1/(4\sin^2\phi))$	$2\pi(1/2, -1/2)$
B	$2\pi(1-1/(4\sin^2\phi), 1/(4\sin^2\phi))$	$2\pi(1-1/(4\cos^2\phi), -1/(4\cos^2\phi))$
C	$2\pi(1/2, 1/2)$	$2\pi(1/(4\cos^2\phi), 1/(4\cos^2\phi))$

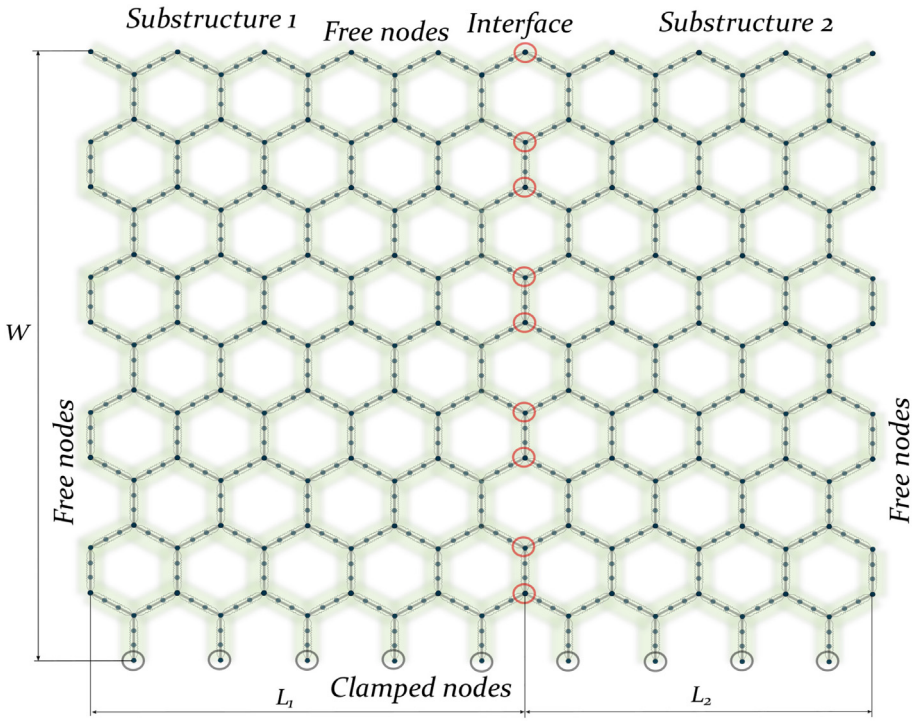

Fig. 3. Two sub-structures coupled through the interface in geometrical points.

$$(\mathbf{K}_{ii,p} - \omega_r^2 \mathbf{M}_{ii,p})\{\eta_{i,p}\}_r = \mathbf{0}. \tag{28}$$

The obtained eigenvectors as the solution of Eq. (28) are known as fixed-interface modes, whereby taking the truncated set of these mass – normalized eigenvectors, they are composed into the fixed-interface mode matrix

$$\mathbf{\Phi}_p = \begin{bmatrix} \{\eta_{i,p}\}_1, \ldots, \{\eta_{i,p}\}_n \\ \mathbf{0} \end{bmatrix} = \begin{bmatrix} \mathbf{\Phi}_{i,p} \\ \mathbf{0} \end{bmatrix}. \tag{29}$$

Now, by combining the set of component and fixed-interface modes one can form a unique matrix known as Hurty-Craig-Bampton (HCB) reduction matrix given as

$$\mathbf{T}_p^{HCB} = \begin{bmatrix} \mathbf{\Phi}_p & \mathbf{\Psi}_p \end{bmatrix}, \tag{30}$$

The above relation provides a transformation from the HCB generalized DOFs to the sub-structure physical DOFs,

$$\begin{Bmatrix} \mathbf{q}_{i,p} \\ \mathbf{q}_{b,p} \end{Bmatrix} \approx \mathbf{T}_p^{HCB} \begin{Bmatrix} \mathbf{u}_{i,p} \\ \mathbf{q}_{b,p} \end{Bmatrix}, \tag{31}$$

where $\mathbf{u}_{i,p}$ represents the modal coordinate vector associated with the fixed-interface modes.

Introducing the transformed DOFs from Eq. (31) into Eq. (25) and pre-multiplying such obtained results with HCB transformation matrix Eq. (30) yields

$$\begin{aligned} \mathbf{M}_p^{HCB} &= \left(\mathbf{T}_p^{HCB}\right)^T \mathbf{M}_p \mathbf{T}_p^{HCB}, \\ \mathbf{K}_p^{HCB} &= \left(\mathbf{T}_p^{HCB}\right)^T \mathbf{K}_p \mathbf{T}_p^{HCB}, \end{aligned} \tag{32}$$

where $\mathbf{M}_p^{HCB}$ and $\mathbf{K}_p^{HCB}$ represents the HCB reduced mass and stiffness matrices, respectively.

After reducing the sub-component matrices one needs to reassemble the whole system to analyse global dynamic behaviour. As mentioned above, the presented hexagonal structure is divided into two sub-structures, where in the case of two parts the following value $p = 2$ is set. Introduction of the coupling matrices that connect displacement vectors of a sub-structure with displacement vectors of the assembly yields mass and stiffness matrices in the following form

$$\begin{aligned} \mathbf{M}^{HCB} &= \sum_{p=1}^{2} \left(\mathbf{R}_p^{HCB}\right)^T \mathbf{M}_p^{HCB} \left(\mathbf{R}_p^{HCB}\right), \\ \mathbf{K}^{HCB} &= \sum_{p=1}^{2} \left(\mathbf{R}_p^{HCB}\right)^T \mathbf{K}_p^{HCB} \left(\mathbf{R}_p^{HCB}\right), \end{aligned} \tag{33}$$

where the reduced matrices ($\mathbf{M}^{HCB}$, $\mathbf{K}^{HCB}$) represents a sum of the reduced matrices of sub-components. The sub-structure coupling matrices $\mathbf{R}_p^{HCB}$ determined for the hexagonal structure are given in the following form

$$\begin{Bmatrix} \mathbf{u}_{i,1} \\ \mathbf{q}_{b,1} \end{Bmatrix} = \begin{Bmatrix} \mathbf{I} & \mathbf{0} & \mathbf{0} \\ \mathbf{0} & \mathbf{0} & \mathbf{I} \end{Bmatrix} \begin{Bmatrix} \mathbf{u}_{i,1} \\ \mathbf{u}_{i,2} \\ \mathbf{q}_{b,1} \end{Bmatrix} \rightarrow \mathbf{R}_1^{HCB} = \begin{Bmatrix} \mathbf{I} & \mathbf{0} & \mathbf{0} \\ \mathbf{0} & \mathbf{0} & \mathbf{I} \end{Bmatrix}, \tag{34}$$

$$\begin{Bmatrix} \mathbf{u}_{i,2} \\ \mathbf{q}_{b,2} \end{Bmatrix} = \begin{Bmatrix} \mathbf{0} & \mathbf{I} & \mathbf{0} \\ \mathbf{0} & \mathbf{0} & \mathbf{I} \end{Bmatrix} \begin{Bmatrix} \mathbf{u}_{i,1} \\ \mathbf{u}_{i,2} \\ \mathbf{q}_{b,1} \end{Bmatrix} \rightarrow \mathbf{R}_2^{HCB} = \begin{Bmatrix} \mathbf{0} & \mathbf{I} & \mathbf{0} \\ \mathbf{0} & \mathbf{0} & \mathbf{I} \end{Bmatrix}.$$

In further analysis, the reduced mass and stiffness matrices in Eq. (33) are used to determine natural frequencies of the presented hexagonal structure. However, it is well known that the interface DOFs can be also reduced and the methodology based on the system-level reduction is introduced next.

3.2. Interface reduction

The system-level reduction is based on the secondary eigenvalue problem of the assembled structure, where the number of interface DOFs is reduced. By dividing the assembled mass and stiffness matrices between the interface and interior parts, and considering only the interface portion, the following eigenvalue problem is formed

$$(\mathbf{K}_{bb}^{HCB} - \omega_r^2 \mathbf{M}_{bb}^{HCB})\{\eta_r^{S-CC}\} = \mathbf{0}, \tag{35}$$

where $\mathbf{M}_{bb}^{HCB}$ and $\mathbf{K}_{bb}^{HCB}$ are the mass and stiffness matrices of the interface part of the assembled structure. The vector $\{\eta_r^{S-CC}\}$ represents truncated set of eigenvectors or S-CC modes. Collecting the S-CC normalized modes into one mode shape matrix yields

$$\mathbf{\Phi}^{S-CC} = \left[\eta_1^{S-CC}, \ldots, \eta_n^{S-CC}\right]. \tag{36}$$

Transforming the interface DOF of HCB assembled system by using the Eq. (36), the reduced form of S-CC vector is obtained as

$$\mathbf{q}_b \approx \mathbf{\Phi}^{S-CC}\mathbf{u}_b. \tag{37}$$

To derive the S-CC transformed mass and stiffness matrices, pre- and post-multiplication with the extended S-CC modal matrix gives

$$\begin{aligned}\mathbf{M}^{S-CC} &= \left(\mathbf{R}^{S-CC}\right)^T \mathbf{M}^{HCB}\left(\mathbf{R}^{S-CC}\right),\\ \mathbf{K}^{S-CC} &= \left(\mathbf{R}^{S-CC}\right)^T \mathbf{K}^{HCB}\left(\mathbf{R}^{S-CC}\right),\end{aligned} \tag{38}$$

where the extended S-CC modal matrix has the following form

$$\mathbf{R}^{S-CC} = \begin{Bmatrix}\mathbf{I} & \mathbf{0}\\ \mathbf{0} & \mathbf{\Phi}^{S-CC}\end{Bmatrix}.$$

The main drawback of the interface reduction method is small number of interface DOFs since the interface consists of geometrical nodes that are connecting only two sub-structures. However, for efficient computation of large scale periodic structures in low-frequency regime this methodology can be cost-effective and gives results with satisfactory accuracy level.

4. Numerical study and discussion

The band structure of the proposed hexagonal lattice system is investigated for the chosen unit cell configurations based on three coupled elastically embedded Timoshenko beams with attached point masses. Moreover, it is assumed that the beams within the unit cells are pre-stressed and rigidly connected. Two lattice models with different unit cell configurations are adopted in this study known as hexagonal and re-entrant lattices. From the eigenvalue problem formed with mass and stiffness matrices given in Eq. (24) and values of the wave vector **k** given along the contour of IBZ, one can obtain corresponding dispersion curves and band structures of the proposed lattice systems. Moreover, the iso-frequency contours of the dispersion surface modes are plotted as functions of wave numbers $\omega(k_1, k_2)$ characterizing the directional wave properties. The effects of the elastic medium, attached point masses, and pre-stress on the frequency band structure and iso-frequency contours are examined in detail. The results from this study are similar to those obtained in [7] when the influences of the elastic medium, attached point masses, and pre-stress are neglected. It should be emphasized that the adopted pre-stress is introduced as a pre-load at each beam of the system. The HCB model reduction technique is introduced to analyse the free in-plane vibrations and corresponding eigenvalue curves of the lattice structure formed for two types of boundary conditions. The main reason for including such reduced model-based investigation was to save additional computational time compared to that of a full model and at the same time ensure that the wave propagation analysis based on a single unit cell can provide satisfactory results of the dynamic behaviour of a lattice system. According to [40], the dispersion phenomena can be divided into two groups such as weak coupling (veering and locking) and strong coupling effects. Which phenomenon, veering or locking, will occur depends on the product of the gradients of dispersion curves at the crossing frequency. Therefore, veering occurs if the group velocities of propagating waves have the same sign while locking appears if their signs differ [40]. In this study, a particular attention is devoted to the analysis of weak coupling effect phenomenon called veering, which occur in eigenvalue problems depending on a variable parameter e.g. stiffness or mass. In the literature, veering phenomenon is usually attributed to the case when two or more curves describing the eigenvalue loci as a function of some variable parameter veer away and diverge instead of crossing. Here, emergence of veering among dispersion curves and frequency curves in terms of stiffness foundation, point masses, pre-load and internal lattice angle is investigated.

4.1. The frequency band structure

The main characteristic of the proposed lattice periodic structure based on the embedded Timoshenko beam-mass system with additional pre-load is that the propagation of Bloch waves and dynamic responses can be controlled by changing only the external pre-load and attached masses without changing the main structural parameters of the lattice structure. Dispersion relations are obtained by varying the wave vector along the contour of the first Brillouin zone. The resulting representation shows the presence of interesting wave phenomena such as mode veering and band gaps. As given above, a common feature of dispersion curves for the hexagonal honeycomb and other types of lattices is the veering of frequencies i.e. convergence and divergence of the eigenvalues, where dispersion curves (dispersion branches) lay close to one another without crossing along the locus $O-A-B-C-O$ in k space. As shown in [7], the shape of the first Brillouin zone changes with the value of the internal angle and there is a significant difference in band structure between lattices with negative and positive internal angles. Therefore, we adopted two interesting cases of lattices with slenderness ratio $\beta = 1/15$ and negative $\theta = -10^\circ$ and positive $\theta = 30^\circ$ internal angles also called re-entrant and regular hexagonal lattices, respectively. In [7] it was demonstrated that a regular hexagonal lattice features both a veering and bandgap phenomena while in the case of re-entrant lattice the later is absent. This study reveals that a number and position of attached point masses can significantly affect the band structure of the system and introduce new band gaps even for re-entrant lattices. From the physical viewpoint, the effect of attached point masses in the proposed lattice system can be characterized as that of internal resonators in the locally resonant metamaterials [64,65], which leads to the emergence of new band gaps in the frequency band diagrams. Moreover, the emergence of zero-frequency band gap due to the presence of an elastic medium surrounding the beam elements is demonstrated, thus, causing the appearance of the phenomenon that is often called in the literature as zero-frequency Bragg gap [66]. It is well known that the Bragg band gaps mostly appear at higher frequency branches like in phononic type periodic structures [7,9,1].

Some authors [8] used a combination of conventional and auxetic core topology in honeycomb lattices to induce phononic band gaps. However, the lattice structure proposed in this study is a good example where band gaps can emerge at the lowest possible frequency range, starting from the zero-frequency, as a consequence of the elastic medium surrounding the beam elements within the unit cell of a lattice. Moreover, in [67] the authors demonstrated the absence of band gaps in regular hexagonal lattices and doubt about the Bragg scattering nature of band gaps in other types of lattices attributing their generation to localized resonances. In this context, they concluded that in highly connected lattices, the beams themselves act as mechanical resonators enabling the generation of locally resonant band gaps. On the other side, in [68] the authors have shown that resonance frequencies of pinned–pinned beams do not match consistently with directional bandgap frequencies in each direction, therefore suggesting directional band gaps in beam lattice systems are not necessarily linked to local resonance. Such difference of the results between previous studies is attributed to the fact that the latter includes group velocity maps and 3d model considering both the in-plane and out-of-plane modes. An increase in the number of bandgaps at low frequencies caused by the introduced concentrated masses connected to the primary structure of a lattice by soft links was examined in [5]. Some later studies observed locally resonant band gaps induced by microstructure cantilever beams connected to nodes of square [69] and hexagonal [70]

lattices. In both studies, besides resonant modes of attached cantilever beams, mass distribution was identified as an important mechanism for bandgap generation. Here, the main goal was to investigate the influences of attached concentrated masses, elastic medium and applied pre-load on the band structure of the proposed lattice systems while elaborating the nature of the resulting band gaps is out of the scope of this study.

Investigation of dispersion curves and their topology, leading to detection of pass and stop bands by using the Bloch wave analysis for a chosen unit cell configuration, is based on a solution of the corresponding eigenvalue problem. This insight into the band structure of the lattice system allows us to passively control elastic wave propagation. In the numerical simulations, the following material and geometrical parameters are adopted unless otherwise specified: the cross-sectional area $A = bh$, the second moment of inertia $I = \frac{bh^3}{12}$ and the wall's slenderness ratio $\beta = L/d = 1/15$. Length of all the beams is $L = 0.125$ m, $\rho = 25 \cdot 10^3$ kg/m^3 is the mass density, $E = 210 \cdot 10^9$ Pa denotes the elastic modulus, $\nu = 0.25$ is the Poisson's ratio and $M = 2$ is the number of attached masses per beam segment. The positions of attached point masses are identical for each beam in the unit cell and they are also placed at the end of each beam i.e. at beam's connection points. The stiffness of Winkler's elastic medium, in which a unit cell is embedded, is given as $k_u = k_w = 10^6$ N/m^2. The effect of the pre-stress is introduced through the pre-load on each beam within the unit cell as $N_0 = -10^4$ N. In the following, for clear demonstration of the results, the frequency $\omega(k_1, k_2)$ is normalized with respect to ω_0 as $\Omega = \omega/\omega_0$, where $\omega_0 = \frac{\pi^2}{L^2}\sqrt{\frac{EI}{\rho A}}$ is the first flexural frequency of the simply-supported Euler–Bernoulli beam of the length L. The number of finite elements per beam in the unit cell is adopted as $n_{ele} = 25$.

4.2. The effect of attached point masses

The effects of attached masses and internal angle θ on the Bloch wave propagation are investigated by analysing the obtained dispersion curves and corresponding frequency band structure. The dispersion diagrams demonstrate that introduction of additional masses at beams connection points of the lattice can cause a widening of existing or even appearance of new band gaps. Moreover, in some specific frequency range, mode veering phenomenon may appear at several positions on the band structure diagrams. According to [1], for all values of the wave vector k along $O - A - B - C - O$ contour, veering phenomenon occur when two branches are very close one to another without any overlap or crossing. Furthermore, the analysis presented herein is limited to two different lattice structures with the main difference in the internal angle θ. When the angle θ is positive $(\theta = 30^\circ)$, the periodic structure is a regular hexagonal honeycomb lattice while for the case when θ is negative $(\theta = -10^\circ)$ the periodic structure belongs to the class of re-entrant (auxetic) lattice structures.

Fig. 4 shows the frequency band structure diagrams of a regular honeycomb structure for different values of attached point masses and wall's slenderness ratio $\beta = 1/15$. One can count fifteen branches of dispersion curves that correspond to the first fifteen values obtained by solving the eigenvalue problem from Eq. (23). The four different cases are examined starting from the case without attached masses $M_p = 0$ and then introducing and increasing the values of attached masses until $M_p = \frac{1}{2}\rho AL$. A comparison of the results obtained for different values of masses shows quite interesting band structure. It can be noticed that an increase in the attached point masses values leads to the appearance of new band gaps as well as the widening of the existing ones at higher frequencies. Further, for an increase of the values of attached masses, one can observe stretching of dispersion curves that become more flatten, especially curves bounding the band gaps. In comparison to the case without attached masses Fig. 4(a) (see also [7]), where only a single complete band gap is detected for the regular hexagonal honeycomb structure, several band gaps can be detected when masses are attached to lattice nodes followed by widening of band gaps at higher frequencies. As stated in [69], the phononic band gaps are commonly attributed to the destructive interference during the multiple scattering and reflection of elastic waves propagating in periodic materials and structures. It is widely accepted that the location and width of the phononic band gaps are related to the geometrical and material properties of periodic lattice structures. Therefore, band gaps due to destructive interference are strongly affected by the distribution of elastic properties and mass in such materials. In [69], the authors have modified a two-dimensional square lattice by introducing the auxiliary cantilever beams at lattice nodes, which changes the mass distribution within the original lattice structure and induce certain band gaps. Here, similar modifications are taken over regular and re-entrant hexagonal lattice structures by adding only concentrated masses at nodes, which changes the mass distribution inside the lattice but does not introduce locally resonant modes like in the case when microstructure cantilever beams are considered. However, attaching concentrated masses and increasing their values introduces new band gaps (Fig. 4(b)–(d)). These new band gaps are placed between branches that are located at frequencies higher than the bandgap of the corresponding pristine lattice, which can confirm that they are not of local resonance origin. Moreover, one can notice several veering points of dispersion curves in the frequency band diagrams. For example, for all different mass cases in (Fig. 4(a) veering between the second and third as well as between the third and fourth branches of the dispersion curve can be observed along the locus O-A. The magnified picture of the veering zone reviles that eigenvalues are close one to another and do not cross but veer away from each other. However, changes in point masses do not affect significantly the number and position of veering points in regular honeycomb lattice structures.

When the wave vector is taken along the entire first Brillouin Zone one can explore the full dispersion surface. For such formed dispersion surfaces one can additionally plot the iso-frequency contour lines as multiple sections of 3*D* dispersion surface. The iso-frequency contours of the regular hexagonal lattice structure given in Figs. 5 and 6 are plotted for the first eight frequency branches in a succeeding manner from the lowest to the highest one, and two attached point masses values given as $(M_p = \frac{1}{12}\rho AL)$ and $(M_p = \frac{1}{2}\rho AL)$. In doing so, the following values of internal lattice angle $\theta = 30^\circ$ and the wall's slenderness ratio $\beta = \frac{1}{15}$ are adopted. If one considers only the iso-frequency contours of the first branch (the first of eight surfaces in Figs. 5 and 6), for both lower and higher values of attached masses, it can be noticed that the outward direction of a given iso-frequency line corresponds to the direction of wave propagation at the observed frequency. These contours display lobed features that indicate the anisotropic properties of the lattice structure, which is in line with the results presented in [7]. However, it is interesting to note how the shape of the contours change with an increase of mass. These changes can not be noticed at lower frequency branches while for the higher ones it is obvious that they are significantly modified, which implies differences in the wave propagation characteristics and mechanical properties between regular hexagonal lattices with different weights of attached masses. This also suggests that if only higher modes are affected then changes in band structure are not caused by the low frequency local resonances but rather ascribed to some other mechanism such as mass distribution within the lattice.

Further, Fig. 7 shows the effect of attached masses on the frequency band structure in the case when the internal lattice angle is given as $\theta = -10^\circ$ and the wall's slenderness ratio as $\beta = 1/15$. One can observe fifteen dispersion curves with a single bandgap detected at higher frequency branches. The well-known hypothesis that Bragg band gaps, which are sensitive to changes in lattice spacing, are located at higher frequencies while locally resonant band gaps depend-

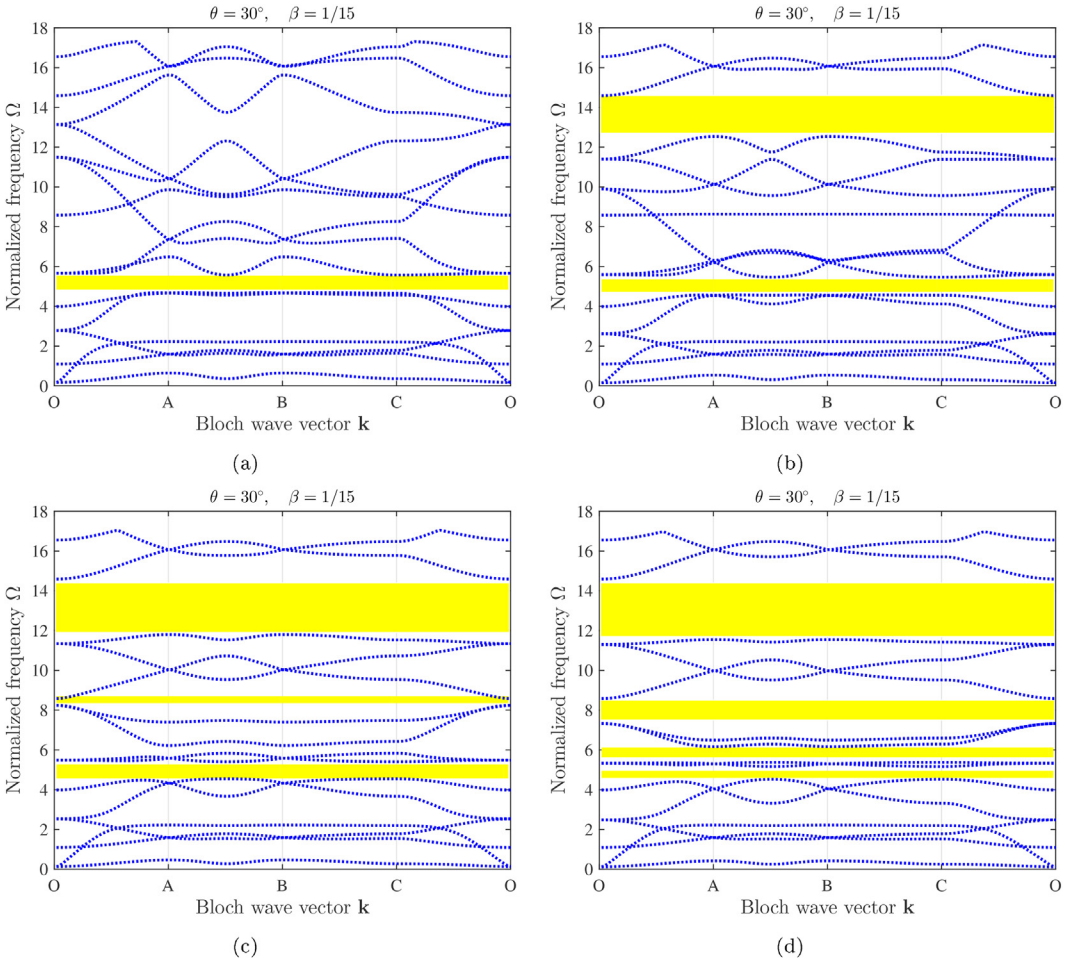

Fig. 4. The effect of the attached point masses on the frequency band structures determined for the regular hexagonal $\theta = 30^\circ$ lattice: (a)$M_p = 0$; (b) $M_p = \frac{1}{6}\rho AL$; (c) $M_p = \frac{1}{3}\rho AL$; (d) $M_p = \frac{1}{2}\rho AL$.

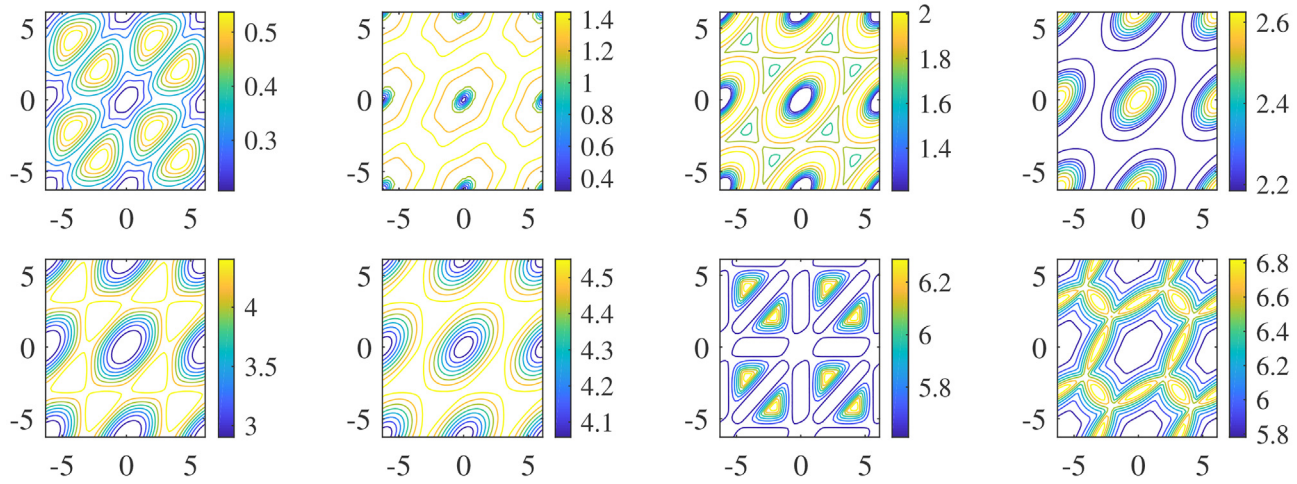

Fig. 5. The effect of the attached point masses on the iso-frequency contours of the regular hexagonal, $\theta = 30^\circ$ lattice with additional point masses $M_p = \frac{1}{12}\rho AL$.

ing on the presence of resonating elements are narrow and located at lower frequencies, will be corroborated based on the following analysis. It can be noticed that an increase in the value of the attached point masses $M_p = \frac{1}{2}\rho AL$ generates additional narrow and lower frequency band gap. Moreover, in comparison with the results from [7], the example of re-entrant lattice structure shows all the advantages of the proposed design since new band gaps can emerge only by increasing the values of attached masses. It can be noticed that mode veering phenomenon becomes more prominent for lower values of attached masses. However, for higher values of attached masses dispersion curves are more flattened and new band gaps are opened, therefore, reducing the number of veering points in the case of re-entrant lattice

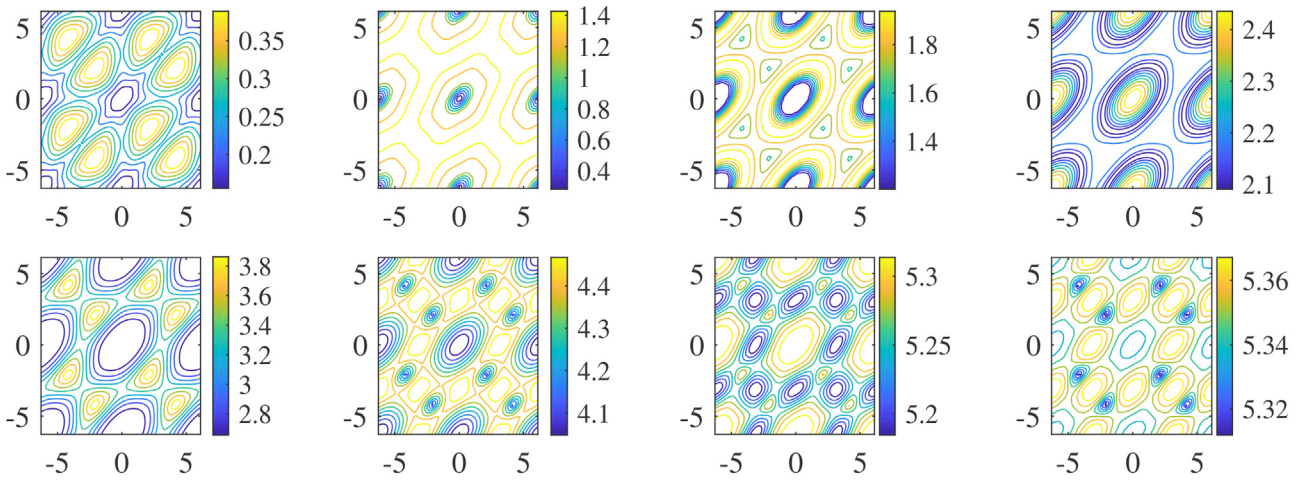

Fig. 6. The effect of attached point masses on the iso-frequency contours of the regular hexagonal $\theta = 30^\circ$ lattice with additional point masses $M_p = \frac{1}{2}\rho AL$.

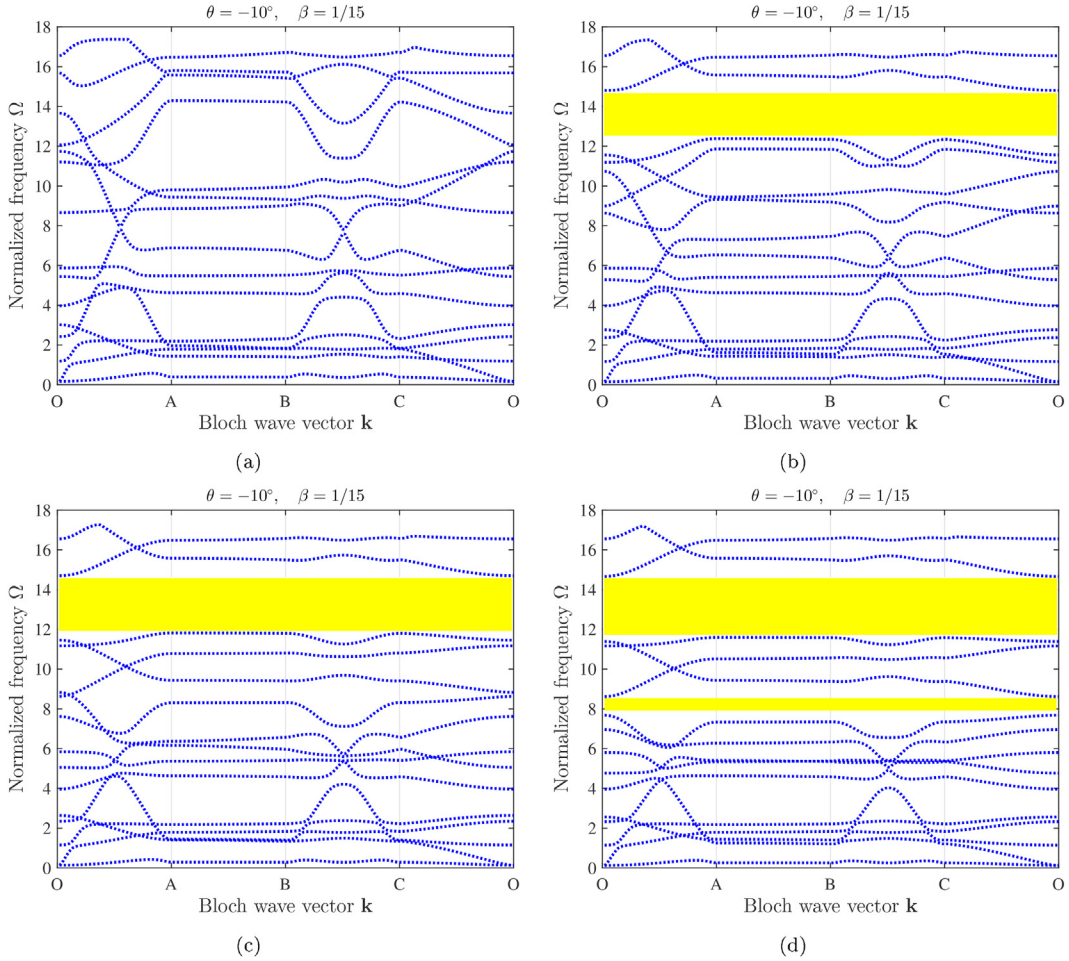

Fig. 7. The effect of the attached point masses on the frequency band structures determined for the re-entrant $\theta = -10^\circ$ lattice: (a) $M_p = 0$; (b) $M_p = \frac{1}{6}\rho AL$; (c) $M_p = \frac{1}{3}\rho AL$; (d) $M_p = \frac{1}{2}\rho AL$.

structures. This can be easily noticed at higher frequency branches within the locus $O - A - B - C - O$

The iso-frequency contour lines for eight frequency branches and the re-entrant lattice ($\theta = -10^\circ$) with two different values of attached masses are given in Figs. 8 and 9. It can be noticed that iso-frequency contours in the first four frequency branches are only slightly changed for the variations of the values of attached masses. However, the effect of an increase of mass is more pronounced at higher frequency branches, where the topology of contour lines is significantly changed concerning the case with lower values of attached masses. Similar to

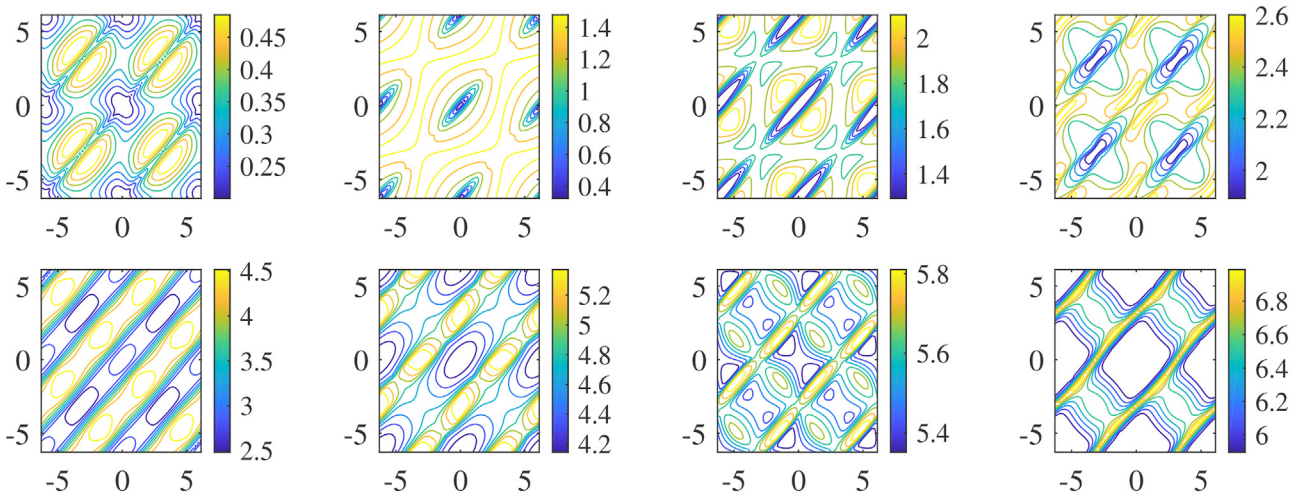

Fig. 8. The effect of attached point masses on the iso-frequency contours of re-entrant $\theta = -10^{\circ}$ lattice with additional point masses $M_p = \frac{1}{12}\rho AL$.

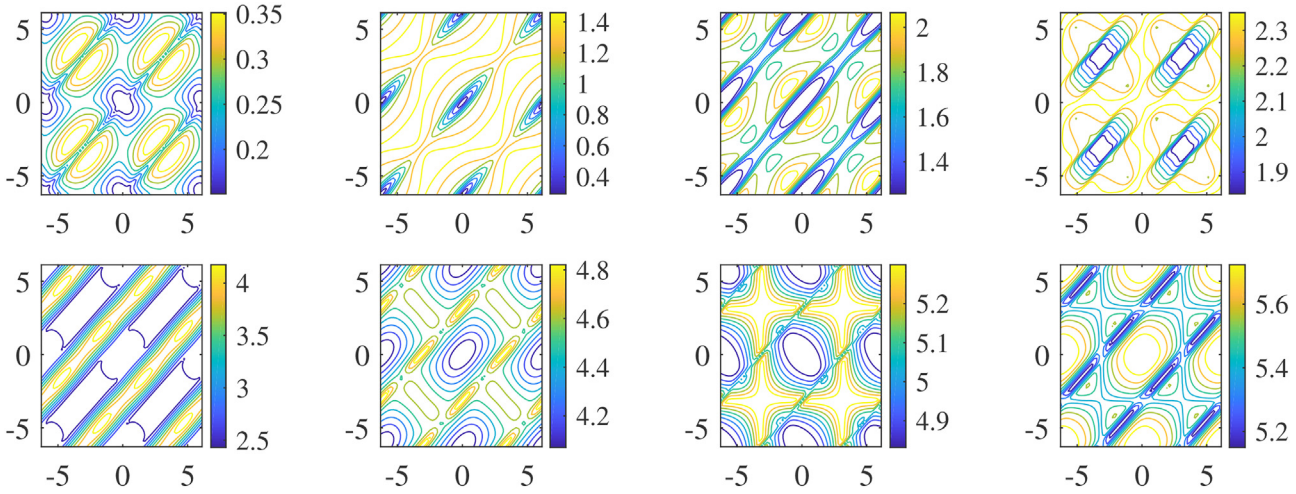

Fig. 9. The effect of attached point masses on the iso-frequency contours of re-entrant $\theta = -10^{\circ}$ lattice with additional point masses $M_p = \frac{1}{2}\rho AL$.

the case with regular hexagonal lattice, these changes implies significant difference in wave propagation properties between two lattice configurations at higher frequency branches.

From the viewpoint of practical applications, the presented iso-frequency contours can be used for analysing the self-collimation phenomenon also called wave-beaming [71]. The self-collimation phenomenon is an alternative way of waveguiding through the periodic medium, where incident wave propagates with almost no diffraction [71]. More details about the application of this phenomenon in the design of mechanical waveguides can be found in [72,73]. There is a promising potential of lattice structures with attached point masses to be used as waveguides using the self-collimation phenomenon, which can be an interesting subject for some future investigation challenge.

4.3. The effect of Winkler's elastic medium

Fig. 10 shows the influence of the stiffness of Winkler's elastic medium on dispersion curves and band structure of the regular hexagonal ($\theta = 30^{\circ}$) and re-entrant ($\theta = -10^{\circ}$) lattice structures for the wall's slenderness ratio given as $\beta = 1/15$. The following values of the stiffness of elastic medium are adopted: $k_u = k_w = 0\ \mathrm{N/m^2}$ and $k_u = k_w = 10^8\ \mathrm{N/m^2}$. The reason for introducing such high values of stiffness is to obtain the lowest possible band gap known as zero-frequency Bragg gap, as explained in [66]. According to [66], zero-frequency Bragg gaps can appear in periodic structures when structural elements are lying on the elastic foundation, which means that additional stiffness is introduced into the system. Fig. 10(a) and (b) shows the effect of the stiffness of Winkler's elastic medium on dispersion curves determined for the regular hexagonal unit cell. It can be noticed that the band gaps around $\Omega = 4.5$ and $\Omega = 14$ are slightly reduced. However, higher values of stiffness lead to the appearance of the additional band gap near the zero frequency Fig. 10(b). In the case of the re-entrant lattice structure, the effect of change of elastic medium stiffness becomes more prominent since the band gaps at higher frequency branches are even more reduced. In this case, the zero-frequency band gap is also detected. Besides, it is worth noting that dispersion curves are flattened for lower frequency branches and higher values of the stiffness of elastic medium in both cases of regular hexagonal and re-entrant lattice structures. Such behaviour can be physically interpreted as stiffening of the system, where as explained above, re-distribution of elastic properties can contribute to change of band structure properties, which is in this case emergence of the zero-frequency band gap. A number and position of veering

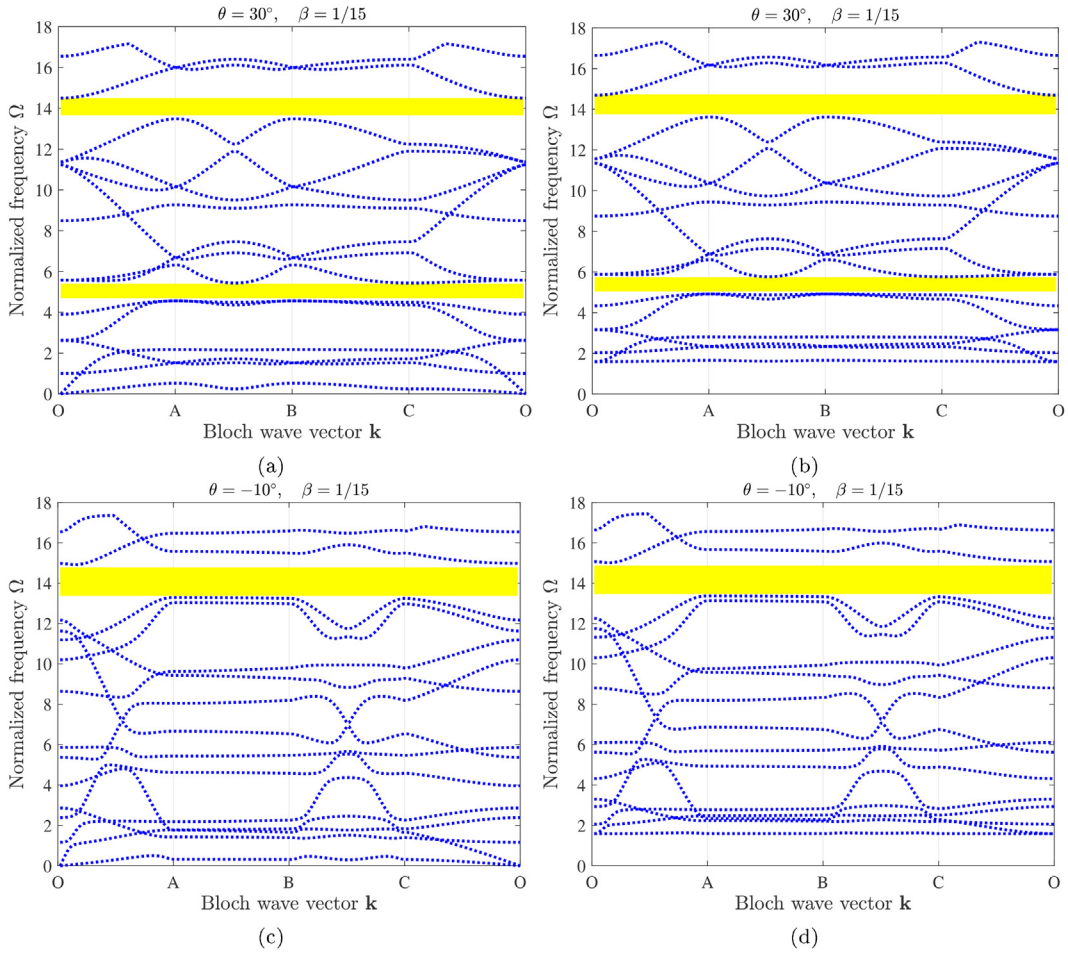

Fig. 10. The effect of the Winkler's elastic medium on the frequency band structures determined for $N_0 = -10^4(N)$, $M_p = \frac{1}{12}\rho AL$, the regular hexagonal lattice, (a) $K_u = K_w = 0$ N/m^2; (b) $K_u = K_w = 10^8$ N/m^2; the re-entrant lattice, (c) $K_u = K_w = 0$ N/m^2; (d) $K_u = K_w = 10^8$ N/m^2.

points does not change significantly for an increase of the foundation's stiffness parameter. However, there is a significant difference between two types of lattices where less veering points are located within a locus $A - B$ for regular hexagonal lattices, Fig. 10(a) and (b), while a higher number of veering points can be detected in re-entrant lattices but mostly located between $O - A$ and $B - C$ in Fig. 10(c) and (d).

4.4. The effect of pre-load

Fig. 11 shows the influence of pre-load on the frequency band structure of the regular hexagonal $(\theta = 30^\circ)$ and re-entrant $(\theta = -10^\circ)$ honeycomb structures for $N_0 = 0$ and $N_0 = 10^4$ N. The comparative study shows that the effect of pre-load on dispersion curves is small in both cases of honeycomb structures if compared to the effect of other parameters. The main reason for such behaviour might be attributed to the fact that the introduced additional stiffness of the Winkler's elastic medium increases the overall stiffness of the system and therefore, the pre-load does not affect dispersion branches significantly. In other words, the stiffness of the elastic medium reduces the effects of pre-load on the band structure of the proposed lattice systems. Moreover, by setting the optimal values of the pre-load and stiffness of the elastic medium, one can control the stop and passbands of honeycomb structures, which can result in optimal design procedures of waveguides and filters. Here, there are no differences in a number and position of veering points for changes in the pre-load parameter in both lower and higher modes.

4.5. Dynamic behaviour of the embedded lattice structure

When investigating the free in-plane vibration of the whole lattice structure, size of the full FE model becomes large, which requires the application of model reduction techniques such as HCB method to reduce the problem. As stated above, the adopted model of the lattice is similar to a plate-like structure with corresponding boundary conditions. Here, we consider two types of boundary conditions the Free-Free-Free-Free (FFFF) and the Clamped-Free-Free-Free (CFFF), which represent the conditions at four sides of the plate-like lattice structure i.e., boundary nodes. Dimensions of the plate-like lattice are given as $L = 1.95$ m and $W = 2.1875$ m. For the application of HCB technique, the initial structure is divided into two sub-structures of lengths $L_1 = 0.97428$ m, and $L_2 = 0.97572$ m, while the height is equal to that of the initial structure. It should be emphasized that the interface reduction technique is based on the S-CC reduction discussed in Section 3. However, it is shown that since the interface consists of only the geometrical nodes, then S-CC reduction technique does not achieve satisfying accuracy compared to the HCB reduction method. Also, a comparative study has shown that the results obtained for natural frequencies by the presented HCB method and COMSOL Multiphysics software are in good agreement. However, the presented analysis does not perform any convergence study of the reduced model, where maximum frequency and time errors are necessary for the eigenvalue analysis. For more details concerning these issues one is referred to [15,59,63].

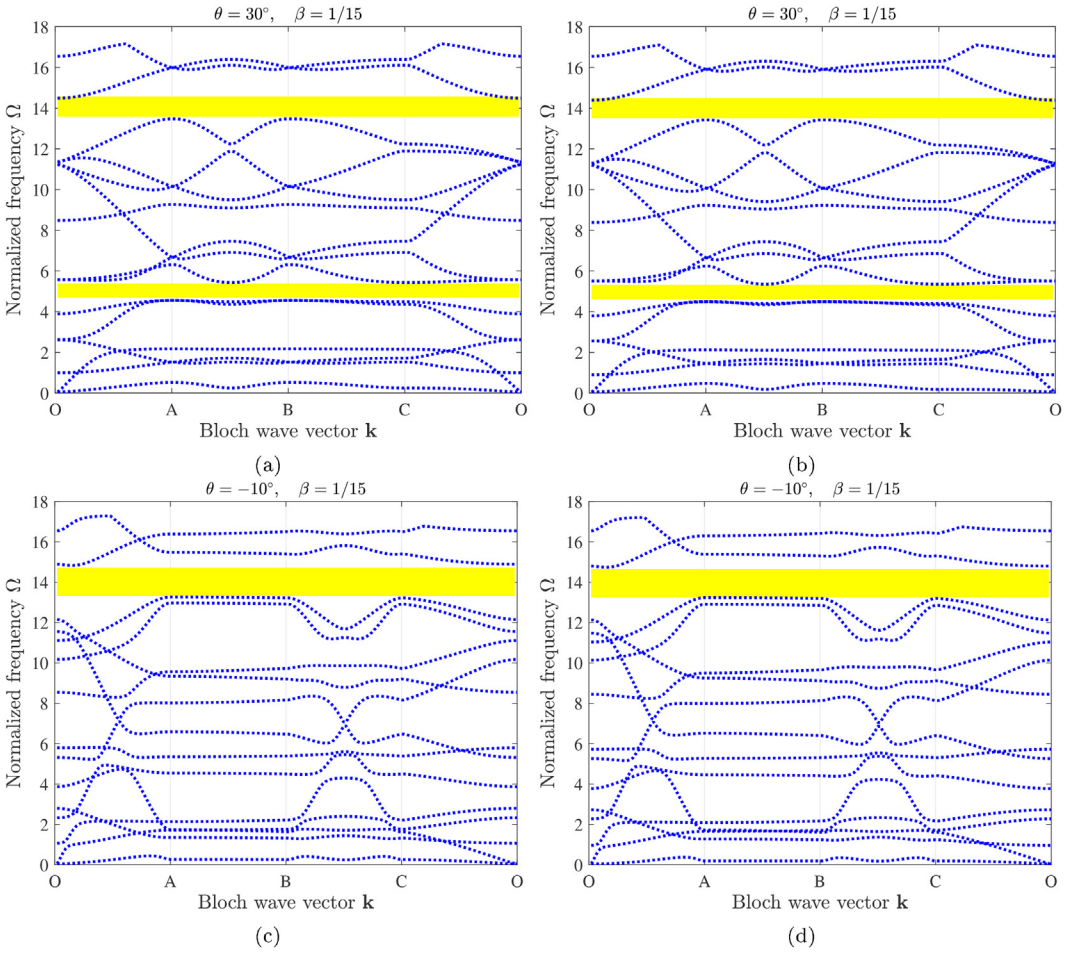

Fig. 11. The effect of the pre-load on the frequency band structures determined for $K_u = K_w = 10^5$ N/m^2, $M_p = \frac{3}{12}\rho AL$, and the regular hexagonal lattice, (a) $N_0 = 0$ N; (b) $N_0 = 10^4$ N; the re-entrant lattice, (c) $N_0 = 0$ N; (d) $N_0 = 10^4$ N.

4.6. Verification

To verify the results for the hexagonal plate-like structure obtained by the HCB model reduction and those from the interface reduction S-CC method, a comparative study is presented in Table 2 and Table 3 for two types of boundary conditions CFFF and FFFF. In this analysis, the effects of attached masses, pre-load, and stiffness of the Winkler's elastic medium are neglected. By solving the corresponding eigenvalue problem, the first ten natural frequencies are determined in Comsol Multiphysics software for the full model of a lattice structure and then compared with the results obtained by the HCB and S-CC model reduction techniques. Table 2 shows the results for natural frequencies given in (Hz) for the CFFF boundary conditions while Table 3 shows the results for the FFFF boundary conditions, where fine agreement between different approaches is achieved. It should be emphasized that the initial problem with 5655 and/or 4668 DOFs is reduced to the problem with only 133 DOFs by introducing the HCB model reduction technique. This significantly reduces the computational time in the dynamic analysis of large-scale problems such as honeycomb plate-like structures. Moreover, it is shown that the interface reduction technique achieves good results only for the first four natural frequencies, reducing the initial problem to only 115 DOFs. In the following

Table 2
The verification of natural frequencies Hz of the embedded hexagonal structure for CFFF boundary conditions ($K_w = K_u = M_p = N_0 = 0$). The number of finite elements per length L is $n_{ele} = 5$.

No.	COMSOL Multiphysics (full model 5655 DOFs)	Full model - CFFF 4638 DOFs	HCB reduction 133 DOFs	HCB + (S-CC) reduction 115 DOFs
1	17.197	17.201	17.202	17.335
2	44.822	44.832	44.837	46.838
3	46.593	46.603	46.604	48.781
4	71	71.014	71.016	73.348
5	73.941	73.958	73.986	92.792
6	86.489	86.501	86.519	104.42
7	92.385	92.406	92.429	107.59
8	100.7	100.71	100.81	121.2
9	116.66	116.69	116.8	125.52
10	118.71	118.73	119.03	132.73

Table 3
The verification of natural frequencies Hz of the embedded hexagonal structure for FFFF boundary conditions ($K_w = K_u = M_p = N_0 = 0$). The number of finite elements per length L is $n_{ele} = 5$.

No.	COMSOL Multiphysics (full model 5655 DOFs)	Full model - FFFF 4668 DOFs	HCB reduction 133 DOFs	HCB + (S-CC) reduction 115 DOFs
1	59.472	59.486	59.505	60.949
2	63.517	63.53	63.586	64.108
3	66.987	67.003	67.012	70.089
4	68.031	68.046	68.062	79.466
5	74.716	74.729	74.731	86.41
6	89.241	89.252	89.304	92.272
7	90.298	90.31	90.321	97.246
8	94.306	94.326	94.372	109.86
9	98.317	98.339	98.365	116.93
10	111.39	111.41	111.44	122.19

parametric study, the influence of mass and stiffness matrices on the vibration behaviour of the lattice structure is investigated by the HCB model reduction technique.

4.7. The effects of system parameters on eigenvalue curves

In this subsection, the natural frequencies are determined by using the reduced mass and stiffness matrices obtained by the HCB reduction method for both CFFF and FFFF boundary conditions, represented as the eigenvalue curves. Fig. 12 shows the effect of Winkler's elastic medium stiffness on the first ten natural frequencies. The magnitude of the stiffness is changed in the range 0–10^5 N and it is equal in both directions $k_u = k_w$. The obtained results reveal that an increase in the stiffness increases natural frequencies for both boundary conditions. However, it is evident that the influence of the medium's stiffness is more pronounced for CFFF boundary conditions than for the FFFF one, as given in Fig. 12(a). On the other hand, the impact of stiffness on the eigenvalue curves is almost linear for the FFFF boundary conditions as observed from Fig. 12(b). It is interesting to note that in general, the influence of elastic medium stiffness on higher natural frequencies is very low. Here, a frequency veering phenomenon can be observed from the modal analysis of the free in-plane vibration of the lattice structure, where the frequency is plotted in terms of system parameters. Here, no veering phenomenon can be detected on frequency curves for changes in stiffness of the Winkler's elastic medium.

The first ten natural frequencies in the form of eigenvalue curves with varying attached point masses for two different boundary conditions of the lattice structure are presented in Fig. 13. The values of attached point masses are changed in the range 0–0.495 kg. It can be observed that an increase in the values of attached point masses can reduce the natural frequencies. Moreover, it can be seen that the natural frequencies determined for the FFFF boundary condition are more affected for the varying attached masses (refer Fig. 13(b)), in comparison to the configuration with CFFF boundary conditions. However, in both cases one can notice a nonlinear relationship between the natural frequency and change of values of attached masses.

Further, Fig. 14 shows the influence of the pre-load parameter, given in the range $-1.5 \cdot 10^4$ N $< N_0 < 1 \cdot 10^4$ N, on the first ten natural frequencies in form of eigenvalue curves for the lattice plate-like structure and two types of boundary conditions. In the previous two examples, we have seen that the influences of elastic medium stiffness and attached point masses on natural frequencies are almost identical for both boundary conditions. However, the pre-load directly influences the modes and corresponding natural frequencies. One can notice a frequency veering phenomenon for changes of the pre-load parameter. Fig. 14(a) depicts the natural frequencies determined for the plate-like lattice structure with CFFF boundary conditions. One can observe that the fourth, sixth, and eighth eigenvalues curves are having different behaviour for varying the pre-load parameter. At some points in the graph one can detect mode veering. Fig. 14(b) also shows an interesting behaviour of natural frequencies obtained for the FFFF boundary conditions. In this case, one can also observe mode veering for varying values of the pre-load parameter. As mentioned before, plotted curves of natural frequencies in terms of varying pre-load parameter shows mode veering at certain points of the graph, which demonstrates the importance of this parameter for the appearance of this phenomenon.

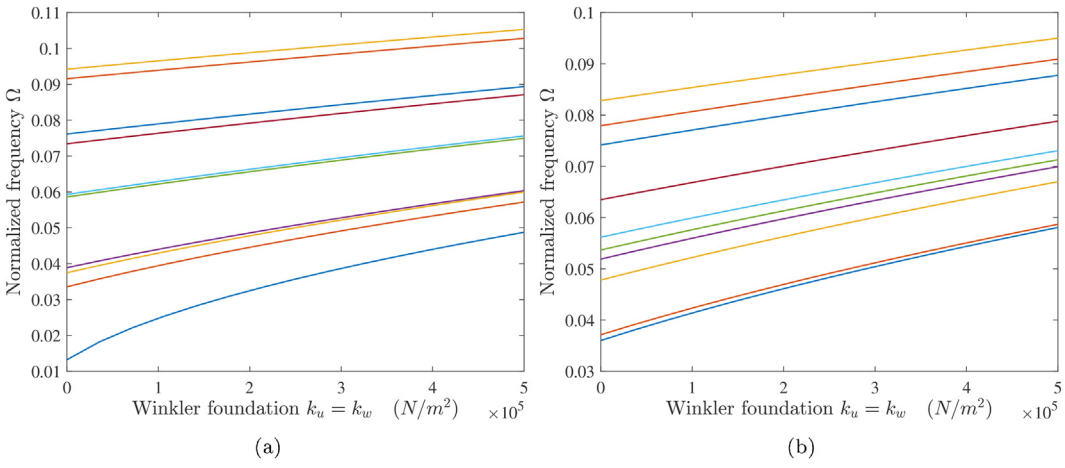

Fig. 12. The effect of the stiffness of Winkler's elastic medium on natural frequencies for the embedded regular hexagonal structure $\theta = 30^\circ$, with $N_0 = 10^4$ N, $M_p = \frac{3}{6}\rho AL$, $\beta = \frac{1}{10}$; (a) CFFF and (b) FFFF boundary conditions.

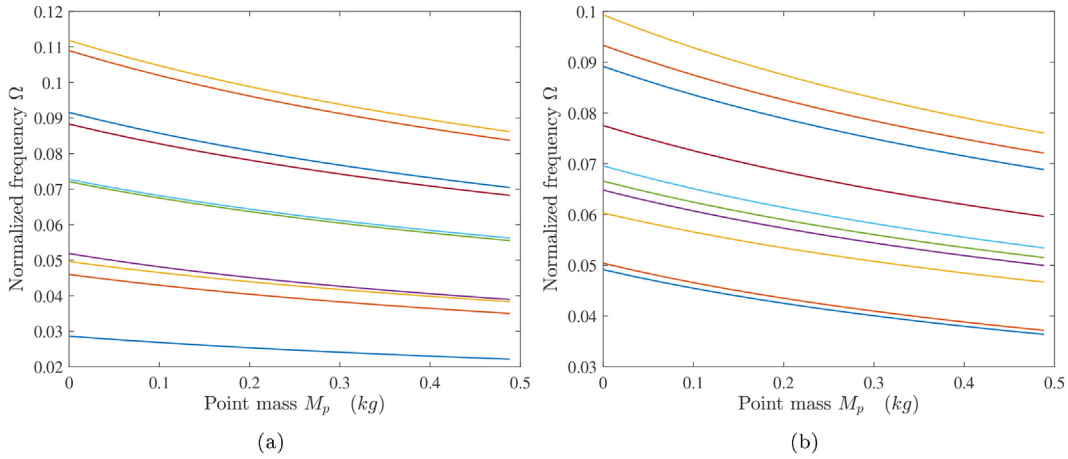

Fig. 13. The effects of attached point masses on natural frequencies determined for the embedded regular hexagonal structure $\theta = 30^\circ$, with $N_0 = 10^4$ N, $\beta = \frac{1}{10}$, $K_u = K_w = 10^5$ N/m^2; (a) CFFF and (b) FFFF boundary conditions.

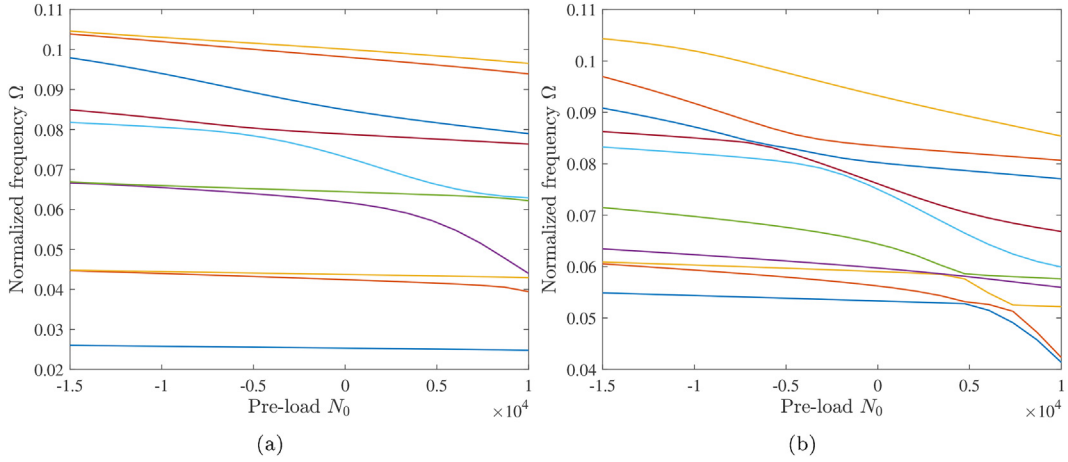

Fig. 14. The effects of the pre-load on natural frequencies determined for the embedded regular hexagonal structure $\theta = 30^\circ$, where $K_u = K_w = 10^5$ N/m^2, $M_p = \frac{3}{6}\rho AL$, $\beta = \frac{1}{10}$; (a) CFFF and (b) FFFF boundary conditions.

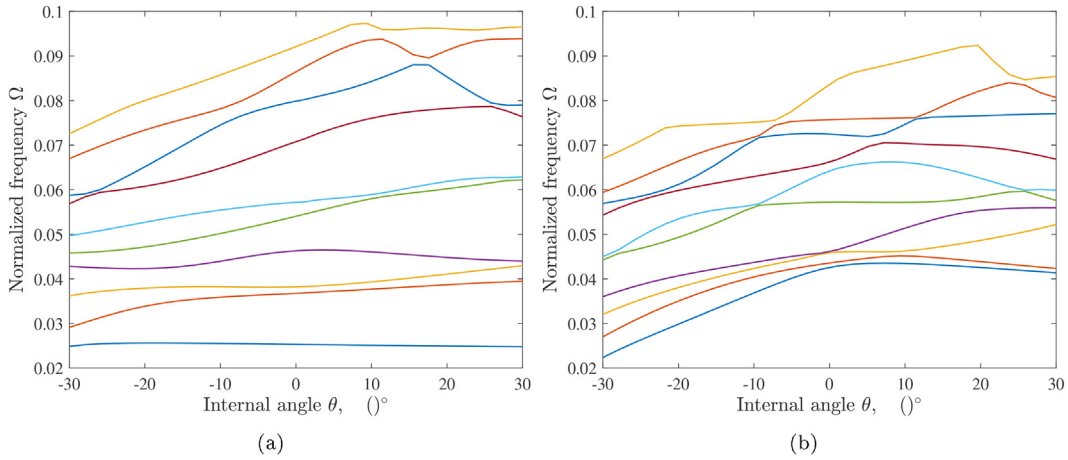

Fig. 15. The effects of the internal angle θ on natural frequencies of the lattice structure for $K_u = K_w = 10^5$ N/m^2, $M_p = \frac{3}{6}\rho AL$, $N_0 = 10^4$ N, $\beta = \frac{1}{10}$; (a) CFFF and (b) FFFF boundary conditions.

The last example shows the influence of the internal angle θ on the eigenvalue curves of the plate-like lattice system for two different boundary conditions, Fig. 15. The natural frequencies in both boundary conditions are almost independent on the angle θ, except in the case when θ approaches the value of 30°. In 15(a), for the case with CFFF boundary conditions, it can be noticed that the first natural

frequency is almost unchanged for varying internal angle θ. However, at higher values of natural frequencies, multiple mode veering occur. On the other hand, the natural frequencies given in 15(b) for the FFFF boundary conditions are manifesting slightly different behaviour since multiple veering occurs in a narrow frequency band. For this boundary condition case, natural frequencies demonstrate similar behaviour for changes of the internal angle θ. It can be concluded that lattice configuration has a strong impact on the appearance of veering phenomenon, which means it is sensitive to varying internal angle θ [74,75]. Due to identical/close modes in periodic lattice structures, mode veering can also lead to mode degeneration/localization and should be investigated in the pre-design stage based on adequate dynamic models. According to [76], veering is manifested in dramatic changes of vibration modes with a strong impact on the dynamic response, which makes performed analyses crucial for insight into the dynamic behaviour of the presented hexagonal lattice systems.

5. Summary and conclusions

The main contribution of this work lies in two aspects. First, it develops a generalized integrated equivalent cost-effective methodology which reduces the computational effort inherently associated with the analysis of wave propagation and dynamic behaviour of periodic lattice structures. In doing so, the proposed methodology efficiently blends in a two-tier physics-based model reduction strategy with the finite element method by coupling, (i) Bloch theorem for reducing the wave propagation analysis of lattice structures to that of a single unit cell, and (ii) Hurty-Craig-Bampton approach for reducing the internal and interface DOFs of the periodic lattice structures. Second, the emergence of frequency veering and zero-frequency band gap is detected in both wave propagation and vibration analysis of honeycomb lattice structures. This provides for the first time a framework to analyse this phenomenon from two different standpoints leading to results that shade into one another.

A model based on the finite element and Bloch wave analysis of the embedded and pre-stressed periodic lattice structure with attached point masses has been developed. Two types of lattice structures, namely, hexagonal and re-entrant honeycombs have been studied, with repetitive unit cells consisting of rigidly connected pre-stressed Timoshenko beams with attached point masses and embedded in the Winkler's type elastic medium. Dispersion curves have been generated by solving the corresponding eigenvalue problem and thereby, important information about band structures of the proposed lattice systems has been obtained. It is found that the combination of the attached point mass, pre-stress and Winkler's elastic medium significantly changes the band structure of lattice structures by introducing new band gaps at lower frequency branches including the zero-frequency band gap. Different veering points are noticed in regular and re-entrant lattice structures.

Dynamic behaviour of the finite length plate-like lattice structures has been investigated by comparing the full model and a reduced model using Hurty-Craig-Bampton approach with additional interface reductions. Comparison of the results for natural frequencies of the finite length lattice structure obtained in Comsol Multiphysics software for the full model and those obtained by using the model reduction techniques shows fine agreement. Parametric study based on the reduced model demonstrated an interesting dynamic behaviour, especially for changes of the internal angle θ. The plots of natural frequency versus internal angle have shown multiple mode veering phenomena i.e., instances of mode degeneration/localization which can significantly affect the dynamic behaviour of a system. Mode veering has been observed for changes in the pre-load parameter. This is possibly the first reported observation of mode veering in the proposed configuration of lattice materials.

In conclusion, the proposed periodic lattice structures revealed exciting band structure and dynamic properties that make them prospective candidates for waveguides and filters. Moreover, the introduction of attached point masses, pre-load and elastic medium is shown to be effective for tuning the band structure properties of lattice structures without changing the basic geometry of the system. These promising results can prove to be useful for adaptive/smart design of periodic lattice structures. The methods presented in this work can be used in future studies for application to more complex 3D lattice structures. Accounting for manufacturing variability in the proposed periodic structures is also another interesting topic of future research.

CRediT authorship contribution statement

Danilo Karličićć: Conceptualization, Methodology, Software. **Milan Cajić:** Data curation, Writing - original draft. **Tanmoy Chatterjee:** Visualization, Investigation, Software. **Sondipon Adhikari:** Supervision, Writing - review & editing.

Declaration of Competing Interest

The authors declare that they have no known competing financial interests or personal relationships that could have appeared to influence the work reported in this paper.

Acknowledgements

D. Karličić and S. Adhikari were supported by the Marie Skłodowska-Curie Actions – European Commission: 799201-METACTIVE. M. Cajić was sponsored by the Serbian Ministry of Education, Science and Technological Development and Mathematical institute of the Serbian Academy of Sciences and Art.

Appendix A. The shape function and matrix coefficients

The adopted shape functions of the Timoshenko beam element:

$$\Gamma_1(x) = 1-\xi, \quad \Gamma_2(x) = 0, \quad \Gamma_3(x) = 0, \tag{39}$$

$$\Gamma_4(x) = \xi, \quad \Gamma_5(x) = 0, \quad \Gamma_6(x) = 0,$$

$$\begin{aligned} &\Lambda_1(x) = 0, \quad \Lambda_2(x) = \frac{1-3\xi^2+2\xi^3+(1-\xi)\Phi}{1+\Phi}, \\ &\Lambda_3(x) = \frac{h_e(\xi-2\xi^2+\xi^3+\frac{1}{2}(\xi-\xi^2)\Phi)}{1+\Phi}, \end{aligned} \tag{40}$$

$$\begin{aligned} &\Lambda_4(x) = 0, \quad \Lambda_5(x) = \frac{3\xi^2-2\xi^3+\xi\Phi}{1+\Phi}, \\ &\Lambda_6(x) = \frac{h_e(-\xi^2+\xi^3-\frac{1}{2}(\xi-\xi^2)\Phi)}{1+\Phi}, \end{aligned}$$

$$\begin{aligned} &\Theta_1(x) = 0, \quad \Theta_2(x) = \frac{6(-\xi+\xi^2)}{h_e(1+\Phi)}, \\ &\Theta_3(x) = \frac{1-4\xi+3\xi^2+(1-\xi)\Phi}{1+\Phi}, \end{aligned} \tag{41}$$

$$\Theta_4(x) = 0, \quad \Theta_5(x) = \frac{6(\xi-\xi^2)}{h_e(1+\Phi)}, \quad \Theta_6(x) = \frac{-2\xi+3\xi^2+\xi\Phi}{1+\Phi},$$

where $\xi = x/h_e$ is the dimensionless axial coordinate and $\Phi = \frac{12EI}{GAk_s h_e^2}$ is the shear deformation parameter.

The elements of the mass and stiffness matrices for finite element beam model:

$$K_{ij}^{e}=\int_{0}^{h_e}\left[EA\frac{\partial\Gamma_i}{\partial x}\frac{\partial\Gamma_j}{\partial x}+EI\frac{\partial\Theta_i}{\partial x}\frac{\partial\Theta_j}{\partial x}+GAk_s\left(\Theta_i-\frac{\partial\Lambda_i}{\partial x}\right)\left(\Theta_j-\frac{\partial\Lambda_j}{\partial x}\right)+k_w\Lambda_i\Lambda_j+k_u\Gamma_i\Gamma_j-N_0\frac{\partial\Lambda_i}{\partial x}\frac{\partial\Lambda_j}{\partial x}\right]dx, \tag{42}$$

$$M_{ij}^{e}=\int_{0}^{h_e}\left(\rho A\Gamma_i\Gamma_j+\rho I\Theta_i\Theta_j+\rho A\Lambda_i\Lambda_j\right)dx, \tag{43}$$

$$R_{ij}^{e}=\int_{0}^{h_e}\left(\sum_{p=1}^{M}M_p\delta(x-a_p)\Gamma_i\Gamma_j+\sum_{p=1}^{M}M_p\delta(x-a_p)\Lambda_i\Lambda_j\right)dx, \tag{44}$$

where matrix $\mathbf{R}^e$ represents the additional mass matrix due to attached point masses on the beam.

References

[1] Phani AS, Hussein MI. Dynamics of lattice materials. Wiley Online Library; 2017..
[2] Zalipaev V, Movchan A, Poulton C, McPhedran R. Elastic waves and homogenization in oblique periodic structures. Proc R Soc Lond Ser A Math Phys Eng Sci 2002;458(2024):1887–912..
[3] Mukhopadhyay T, Adhikari S, Batou A. Frequency domain homogenization for the viscoelastic properties of spatially correlated quasi-periodic lattices. Int J Mech Sci 2019;150:784–806.
[4] Phani AS, Woodhouse J, Fleck N. Wave propagation in two-dimensional periodic lattices. J Acoust Soc Am 2006;119(4):1995–2005.
[5] Martinsson P, Movchan A. Vibrations of lattice structures and phononic band gaps. Q J Mech Appl Math 2003;56(1):45–64.
[6] Poulton C, Movchan A, McPhedran R, Nicorovici N, Antipov Y. Eigenvalue problems for doubly periodic elastic structures and phononic band gaps. Proc R Soc Lond Ser A Math Phys Eng Sci 2000;456(2002):2543–59..
[7] Gonella S, Ruzzene M. Analysis of in-plane wave propagation in hexagonal and re-entrant lattices. J Sound Vib 2008;312(1–2):125–39.
[8] Mukherjee S, Scarpa F, Gopalakrishnan S. Phononic band gap design in honeycomb lattice with combinations of auxetic and conventional core. Smart Mater Struct 2016;25(5):054011.
[9] Meng J, Deng Z, Zhang K, Xu X. Wave propagation in hexagonal and re-entrant lattice structures with cell walls of non-uniform thickness. Waves Random Complex Media 2015;25(2):223–42.
[10] Leamy MJ. Exact wave-based bloch analysis procedure for investigating wave propagation in two-dimensional periodic lattices. J Sound Vib 2012;331(7):1580–96.
[11] Farzbod F, Leamy MJ. Analysis of bloch's method and the propagation technique in periodic structures. J Vib Acoust 133(3)..
[12] Mazloomi MS, Ranjbar M, Boldrin L, Scarpa F, Patsias S, Ozada N. Vibroacoustics of 2d gradient auxetic hexagonal honeycomb sandwich panels. Compos Struct 2018;187:593–603.
[13] Glacet A, Tanguy A, Réthoré J. Vibrational properties of quasi-periodic beam structures. J Sound Vib 2019;442:624–44.
[14] An X, Fan H, Zhang C. Elastic wave and vibration bandgaps in planar square metamaterial-based lattice structures. J Sound Vib 2020;115292.
[15] Krattiger D, Wu L, Zacharczuk M, Buck M, Kuether RJ, Allen MS, Tiso P, Brake MR. Interface reduction for hurty/craig-bampton substructured models: Review and improvements. Mech Syst Signal Process 2019;114:579–603.
[16] De Klerk D, Rixen D, Voormeeren S. General framework for dynamic substructuring: history, review, and classification of techniques. AIAA J 2008;46:1169–81.
[17] Boldrin L, Hummel S, Scarpa F, Di Maio D, Lira C, Ruzzene M, Remillat C, Lim T, Rajasekaran R, Patsias S. Dynamic behaviour of auxetic gradient composite hexagonal honeycombs. Compos Struct 2016;149:114–24.
[18] Silva PB, Mencik J, Arruda JRDF. Wave finite element-based superelements for forced response analysis of coupled systems via dynamic substructuring. Int J Numer Methods Eng 2016;107(6):453–76.
[19] Mencik J. A wave finite element approach for the analysis of periodic structures with cyclic symmetry in dynamic substructuring. J Sound Vib 2016;431(6):441–57.
[20] Fu J, Xia L, Gao L, Xiao M, Li H. Topology optimization of periodic structures with substructuring. J Mech Des 2019;141(7):071403.
[21] Shiyin X, Xiuchang H, Hongxing H. A study on the isolation performance of trichiral lattices with gradient geometry. J Vib Control 2015;21(16):3465–75.
[22] Shen C, Lu G, Yu T. Dynamic behavior of graded honeycombs–a finite element study. Compos Struct 2013;98:282–93.
[23] Khakalo S, Balobanov V, Niiranen J. Modelling size-dependent bending, buckling and vibrations of 2d triangular lattices by strain gradient elasticity models: applications to sandwich beams and auxetics. Int J Eng Sci 2018;127:33–52.
[24] Baravelli E, Ruzzene M. Internally resonating lattices for bandgap generation and low-frequency vibration control. J Sound Vib 2013;332(25):6562–79.
[25] Gonella S, Ruzzene M. Homogenization and equivalent in-plane properties of two-dimensional periodic lattices. Int J Solids Struct 2008;45(10):2897–915.
[26] Joseph L, Craster RV. Asymptotics for rayleigh–bloch waves along lattice line defects. Multiscale Model Simul 2013;11(3):871–89.
[27] Makwana M, Craster R. Homogenisation for hexagonal lattices and honeycomb structures. Q J Mech Appl Math 2014;67(4):599–630.
[28] Narisetti RK, Ruzzene M, Leamy MJ. Study of wave propagation in strongly nonlinear periodic lattices using a harmonic balance approach. Wave Motion 2012;49(2):394–410.
[29] Wang P, Shim J, Bertoldi K. Effects of geometric and material nonlinearities on tunable band gaps and low-frequency directionality of phononic crystals. Phys Rev B 2013;88(1):014304.
[30] Mousanezhad D, Babaee S, Ghosh R, Mahdi E, Bertoldi K, Vaziri A. Honeycomb phononic crystals with self-similar hierarchy. Phys Rev B 2015;92(10):104304.
[31] Trainiti G, Rimoli JJ, Ruzzene M. Wave propagation in undulated structural lattices. Int J Solids Struct 2016;97:431–44.
[32] Zhang K, Su Y-C, Hou X-H, Meng J-M, Deng Z-C. Effect of pre-load on wave propagation characteristics of hexagonal lattices. Compos Struct 2018;203:361–72.
[33] Gei M. Wave propagation in quasiperiodic structures: stop/pass band distribution and prestress effects. Int J Solids Struct 2010;47(22–23):3067–75.
[34] Gei M, Movchan A, Bigoni D. Band-gap shift and defect-induced annihilation in prestressed elastic structures. J Appl Phys 2009;105(6):063507.
[35] Gei M, Bigoni D, Movchan A, Bacca M. Band-gap properties of prestressed structures. In: Acoustic metamaterials. Springer; 2013. p. 61–82.
[36] Miniaci M, Mazzotti M, Bartoli I. Modeling bloch waves in prestressed phononic crystal plates. Front Mater 2019;6:74.
[37] Zhang K, Zhao P, Zhao C, Hong F, Deng Z. Study on the mechanism of band gap and directional wave propagation of the auxetic chiral lattices. Compos Struct 2020;238:111952.
[38] Anderson MS. Vibration of prestressed periodic lattice structures. AIAA J 1982;20(4):551–5.
[39] Koellner A, Todt M, Ganzosch G, Völlmecke C. Experimental and numerical investigation on pre-stressed lattice structures. Thin-Wall Struct 2019;145:106396.
[40] Mace BR, Manconi E. Wave motion and dispersion phenomena: Veering, locking and strong coupling effects. J Acoust Soc Am 2012;131(2):1015–28.
[41] Tee K, Spadoni A, Scarpa F, Ruzzene M. Wave propagation in auxetic tetrachiral honeycombs. J Vib Acoust 132(3)..
[42] Bergamini, AE, Zündel M, Flores Parra EA, Delpero T, Ruzzene M, Ermanni P. Hybrid dispersive media with controllable wave propagation: a new take on smart materials. J Appl Phys 2015;118(15):154310..
[43] Zhu Z, Deng Z, Tong S, Ding B, Du J. Elastic wave propagation in hierarchical lattices with convex and concave hexagons stacked vertexes. J Acoust Soc Am 2019;146(3):1519–27.
[44] du Bois JL, Adhikari S, Lieven NAJ. On the quantification of eigenvalue curve veering: a veering index. Trans ASME J Appl Mech 2011;78(4):041007:1–8..
[45] Hodges C, Woodhouse J. Vibration isolation from irregularity in a nearly periodic structure: theory and measurements. J Acoust Soc Am 1983;74(3):894–905.
[46] Chan HC, Liu JK. Mode localization and frequency loci veering in disordered engineering structures. Chaos Solitions Fract 2000;11:1493–504.
[47] Happawana G, Bajaj A, Nwokah O. A singular perturbation analysis of eigenvalue veering and modal sensitivity in perturbed linear periodic systems. J Sound Vib 1993;160(2):225–42.
[48] Natsiavas S. Mode localization and frequency veering in a non-conservative mechanical system with dissimilar components. J Sound Vib 1993;165(1):137–47.
[49] Adhikari S. Calculation of derivative of complex modes using classical normal modes. Comput Struct 2000;77(6):625–33.
[50] Jafari H, Yazdi MH, Fakhrabadi MMS. Damping effects on wave-propagation characteristics of microtubule-based bio-nano-metamaterials. Int J Mech Sci 2020;105844.
[51] Chatterjee T, Karlicic D, Adhikari S, Friswell M. Gaussian process assisted stochastic dynamic analysis with applications to near-periodic structures. Mech Syst Signal Process 2021;149:107218..
[52] du Bois JL, Adhikari S, Lieven NAJ. Mode veering in stressed framed structures. J Sound Vib [Published online]..
[53] Liu X, Hu G, Sun C, Huang G. Wave propagation characterization and design of two-dimensional elastic chiral metacomposite. J Sound Vib 2011;330(11):2536–53.
[54] Brillouin L Wave propagation in periodic structures: electric filters and crystal lattices..
[55] Reddy JN.An introduction to the finite element method, New York 27..
[56] Yokoyama T. Vibration analysis of Timoshenko beam-columns on two-parameter elastic foundations. Comput Struct 1996;61(6):995–1007.
[57] Kittel C, McEuen P, McEuen P. Introduction to solid state physics, vol. 8. New York: Wiley; 1996.
[58] Kaxiras E, Joannopoulos JD. Quantum theory of materials..
[59] Chatterjee T, Adhikari S, Friswell M. Uncertainty propagation in dynamic sub-structuring by model reduction integrated domain decomposition. Comput Methods Appl Mech Eng 2020;366:113060.
[60] Boo SH, Kim JH, Lee PS. Towards improving the enhanced Craig-Bampton method. Comput Struct 2018;196:63–75.
[61] Jensen HA, Araya VA, Muñoz AD, Valdebenito MA. A physical domain-based substructuring as a framework for dynamic modeling and reanalysis of systems. Comput Methods Appl Mech Eng 2017;326:656–78.
[62] Craig RR, Kurdila AJ. Fundamentals of structural dynamics. John Wiley & Sons; 2006.
[63] Allen MS, Rixen D, van der Seijs M, Tiso P, Abrahamsson T, Mayes RL. Substructuring in engineering dynamics. Springer; 2020.
[64] An X, Sun F, Yu P, Fan H, He S, Fang D. Negative effective mass density of one-dimensional hierarchical metacomposite. J Appl Mech 82(3)..

[65] Tian Y, Wu JH, Li H, Gu C, Yang Z, Zhao Z, Lu K. Elastic wave propagation in the elastic metamaterials containing parallel multi-resonators. J Phys D Appl Phys 2019;52(39):395301.
[66] Pal RK, Rosa MI, Ruzzene M. Topological bands and localized vibration modes in quasiperiodic beams. New J Phys 2019;21(9):093017.
[67] Wang P, Casadei F, Kang SH, Bertoldi K. Locally resonant band gaps in periodic beam lattices by tuning connectivity. Phys Rev B 2015;91(2):020103.
[68] Zelhofer AJ, Kochmann DM. On acoustic wave beaming in two-dimensional structural lattices. Int J Solids Struct 2017;115:248–69.
[69] Liu W, Chen J-W, Su X-Y. Local resonance phononic band gaps in modified two-dimensional lattice materials. Acta Mech Sin 2012;28(3):659–69.
[70] Gonella S, To AC, Liu WK. Interplay between phononic bandgaps and piezoelectric microstructures for energy harvesting. J Mech Phys Solids 2009;57(3):621–33.
[71] Chang S-Y, Chen C-D, Yeh J-Y, Chen L-W. Elastic wave propagation of two-dimensional metamaterials composed of auxetic star-shaped honeycomb structures. Crystals 2019;9(3):121.
[72] Ruzzene M, Scarpa F, Soranna F. Wave beaming effects in two-dimensional cellular structures. Smart Mater Struct 2003;12(3):363.
[73] Zhang T, Cheng Y, Guo J-Z, Xu J-Y, Liu X-J. Acoustic logic gates and boolean operation based on self-collimating acoustic beams. Appl Phys Lett 2015;106 (11):113503.
[74] Liu X. Behavior of derivatives of eigenvalues and eigenvectors in curve veering and mode localization and their relation to close eigenvalues. J Sound Vib 2002;256 (3):551–64.
[75] Gallina A, Pichler L, Uhl T. Enhanced meta-modelling technique for analysis of mode crossing, mode veering and mode coalescence in structural dynamics. Mech Syst Signal Process 2011;25(7):2297–312.
[76] Lin J, Parker RG. Natural frequency veering in planetary gears. Mech Struct Mach 2001;29(4):411–29.

Mechanical Systems and Signal Processing 155 (2021) 107591

Contents lists available at ScienceDirect

Mechanical Systems and Signal Processing

journal homepage: www.elsevier.com/locate/ymssp

Bloch waves in an array of elastically connected periodic slender structures

Danilo Karličić [a,b], Milan Cajić [a,b,*], Stepa Paunović [b], Sondipon Adhikari [a]

[a] College of Engineering, Swansea University, United Kingdom
[b] Mathematical Institute of the Serbian Academy of Sciences and Arts, Belgrade, Serbia

ARTICLE INFO

Article history:
Received 5 July 2020
Received in revised form 29 November 2020
Accepted 26 December 2020
Available online 21 January 2021

Keywords:
Bloch waves
Galerkin approximation
Band structure
Elastically connected beams
Concentrated masses

ABSTRACT

This paper proposes the methodology to carry out the analysis of Bloch wave propagation in an array of vertically aligned and elastically connected structural elements such as beams, strings, plates, or other slender structures. The suggested approach is based on the Galerkin approximation and Floquet-Bloch theorem used in defining the eigenvalue problem and obtaining the band structure of the periodic systems. Special attention is devoted to the case of elastically connected Rayleigh beams with attached concentrated masses and wave propagation in the direction normal to the beam's length. A validation study is performed by using the finite element model and the frequency response function to confirm the accuracy of the solution obtained via the Galerkin approximation. Two configurations of unit cells, having two and three elastically connected beams with different geometrical and material properties, are considered in the numerical study. The effects of various parameters are investigated to reveal their influence on the frequency band structure and emergence of the zero-frequency bandgap. The results of this study demonstrates the tunability properties of the proposed periodic systems due to changes in values of concentrated masses, stiffness of the coupling medium or boundary conditions on structural elements within the unit cell.

1. Introduction

Some early notable contributions by Mead and co-workers [1] in the field of harmonic wave propagation analysis in periodic structures motivated many researchers. The main attention in those works was given to one-dimensional [2–4] and two-dimensional periodic structures [5]. It is a well-known fact that waves propagating in a homogeneous continuum are non-dispersive. Contrarily, in a heterogeneous structured medium such as beams and plates, dispersion occurs due to the presence of physical boundaries. Another characteristic of heterogeneous medium, which might be the consequence of microstructural properties or structural interfaces, is the existence of bandgaps as frequency intervals at which waves decay exponentially. This implies difference between homogeneous and heterogeneous medium that was demonstrated in [6], where flexural harmonic waves propagating within the bi-coupled periodic system composed of Euler-Bernoulli beams have been analyzed in great detail. The authors have demonstrated that periodicity, which introduces the internal length, causes the dispersion curve to be reflected at the boundary of the first Brillouin zone. This makes it possible to apply the Floquet-Bloch theory and obtain the dispersion relation that allows one to distinguish pass-bands, the frequencies of the waves that

* Corresponding author at: College of Engineering, Swansea University, United Kingdom.
E-mail addresses: milan.cajic@swansea.ac.uk, mcajic@mi.sanu.ac.rs (M. Cajić).

https://doi.org/10.1016/j.ymssp.2020.107591
0888-3270/

propagate without attenuation, and stop-bands (bandgaps) where the waves decay exponentially. However, in that study only the bi-coupled continuous and discrete systems rigidly connected in series and parallel were considered. Here, the main focus is put on specific type of heterogeneous systems composed of an array of parallel and elastically connected periodic slender structures of the same length/width and boundary condition by studying the wave propagation along the array.

A good example of harmonic axial wave propagation in one-dimensional quasiperiodic-generated structured rods was investigated in [7], which is given as an infinite bar with repeated elementary cells designed by using the Fibonacci substitution rules. Propagation of a transition wave in a more complex system composed of a finite heterogeneous discrete beam strip with periodically placed masses and subjected to the harmonic load was investigated in [8]. Some authors devoted special attention to problems of flexural waves propagation in structures resting on elastic foundation due to the relevance of this subject in various engineering applications.These application examples include models of infinite beams on elastic support carrying a dynamic load that represent slabs, rails or road pavements. The effects of compressive load and support's damping on the dispersion characteristic and transient response of a beam lying on elastic foundation of Winkler type is investigated in [9]. A more complex case was studied in [10] by analyzing the wave propagation and attenuation properties in ordered and disordered periodic composite beams on elastic foundations due to moving loads. It has been shown that one-dimensional discrete flexural systems composed of massless beams connecting periodically placed masses can be used to approximate the Rayleigh's beam on elastic foundation in the long-wavelength limit [11]. In [12], the authors investigated the existence of localized modes in a set of quasi-periodic continuous elastic beams with attached array of ground springs. It is shown that vibration modes are first localized at a boundary and then migrate into a bulk for a varied projection parameter. The structured Rayleigh beams on the elastic foundation that can exhibit dispersion wave characteristics and localized wave-forms were analysed in [13]. Moreover, the influence of pre-stress on the bandgap formation of the elastic beam on elastic foundation was studied in [14]. The authors introduced repeated elementary cells generated by adopting the Fibonacci sequence and then solved the eigenvalue problem by using the transmission matrix of the unit cell and the Bloch solution. By considering the Rayleigh beam theory, the free and forced wave propagation in an elastic grid structure was analysed in [15], where several forms of vibration localization and wave channeling were observed. It was demonstrated that the localization is triggered by several parameters such as rotation inertia and external excitation. By considering the complex beam model suggested in [16], an energy harvesting device was developed based on the metamaterials design, showing great applicability in surface wave control.

Most of the wave dispersion analyses of two-dimensional multi-structural systems in the literature are devoted to the frame-like structures representing multi-story buildings [17], hexagonal chiral lattices [18] or shell structures [19]. Available wave propagation studies of multi structural systems are mostly limited to the analysis of beams rigidly connected through periodically distributed ribs [20] or sandwich structures with a soft [21] or auxetic core [22]. In [21], the authors employed the asymptotic method to analyze a long-wave dynamic model of two layers adhesively connected by a thin and soft core. Particularly, they analyzed the propagation of waves along the thin interface layer and reviled some interesting effects such as coupling between the longitudinal and transverse displacements associated with a slow motion, and longitudinal displacement jumps related to fast motion. Similar problems has been addressed by other authors [23], where also asymptotic method was applied to study wave propagation in a three layer beam with a thin and soft core in the middle. In [24] the authors demonstrated that dynamics of two beams bonded by adhesive joint can be approximately represented by the Winkler and Pasternak type elastic layers for different boundary conditions. This paved the way for dynamic studies of sandwich beams [25], multi-beam [26] and multi-plate [27] systems coupled through discrete elastic or viscoelastic layers. If beam, plate or membrane structures are coupled, they are observed as layered systems having unique band structure properties [28,29] with a great potential for applications in wave absorption [30] and topological waveguiding [31].

According to [32], one can distinguish two main approaches to form the eigenvalue problem for wave propagation analysis in periodic structures.The first and the oldest is the inverse approach, where the propagation constant of a periodic structure is fixed while the unknown frequencies need to be computed. The second is the direct approach, which was later developed to avoid certain deficiencies of the inverse approach, but ill conditioning of the eigenvalue problem and possible low machine precision set limitations to this approach. Therefore, in [32] the authors proposed a combination of these two approaches when defining the eigenvalue problem. Different methods are used in the literature such as plane wave expansion [33], transfer matrix [34], finite element [35] or finite difference method [36], which all belong to the inverse approaches. In [37], the authors named the therein presented approach as the inverse method, where the band structure is determined without explicitly including the terms related to the material and geometrical properties except for the lattice constant, i.e. from the response of the system instead of using a model, as it is done in the majority of the methods available in the literature. Moreover, an interesting study [38] of elastic wave propagation in two-component laminates revealed the universal structure of its frequency spectrum independent of the geometry of the periodic-cell and the specific physical properties. In this study, an inverse Floquet-Bloch approach is applied to define the eigenvalue problem, where the corresponding inverse state-vector is formed after performing the discretization procedure.

The concept of locally resonant metamaterials is often used to form the periodic systems with low frequency bandgaps, in which the lattice dispersion characteristics depend on the modal behaviour of the host structure with its resonators [39]. Modal analysis was shown to be very useful in the nonlinear periodic structure analysis, were the Galerkin approximation method is applied to study the multi-mode vibration absorption capability of a nonlinear metamaterial Euler-Bernoulli beam coupled to a distributed array of nonlinear spring-mass subsystems behaving as local vibration absorbers [40]. Similar methodology was applied in [41], where frequencies of the attached resonators are tuned exactly to targeted modes of a non-

linear metamaterial beam. In [42], a general approach for estimation of the band structure of metamaterials with locally resonant properties is proposed. However, in [43] the authors demonstrated that the Bragg-type and resonance-type gaps can co-exist, which was explained through coupled bandgaps generated in the periodic system such as rod with multiple internal resonators. Since the first introduction of periodic materials with internal resonators [44], the mechanism responsible for the opening of locally resonant bandgaps has been investigated in a number of studies [45–47]. In [48] the authors identified the conditions for the transition between Bragg scattering and local resonance and showed the effects of this transition on the lowest bandgap. This was demonstrated on the examples of different types of materials, geometric and boundary periodicity in Timoshenko beams with and without elastically suspended masses. Moreover, another promissing application of metamaterials and periodic structures lies in seismic shielding over the entire range of frequencies. According to [49], three approaches are used to obtain shielding effects: Bragg scattering, locally resonant sub-wavelength inclusions and application of zero-frequency stop-band media. However, all three mechanisms for bandgap formation occur in a small number of periodic structures, thus providing the motivation for further investigations. Moreover, design of periodic structures is a powerful concept to achieve mechanical wave filtering. Different concepts for filtering of elastic waves are suggested in the literature. The concept based on structural interfaces, initially introduced in [50], involves a non-local mechanical behavior and allows the achievement of special mechanical properties. It was revealed in [51] that thick interfaces separating different regions of elastic materials introduce unique filtering characteristics that cannot be achieved with multilayered interfaces. In this paper, a unique band structure proprieties of the herein proposed systems reveal the presence of all three requirements needed for seismic shielding and wave filtering applications, such as the existence of zero-frequency and low-frequency bandgaps, as well as the bandgaps at higher dispersion branches.

The present paper shows the methodology for studying the wave propagation along the array of vertically aligned and elastically connected periodic structures (e.g. beams, plates, membranes or shallow shells) with the same boundary conditions and coupling medium stiffness. The main steps in defining the problem are the derivation of the system's governing equations, application of multi-mode Galerkin discretization and the assumption of wave propagation in the thickness direction of structural elements using the Floquet-Bloch theory. This methodology is generalized for one-dimensional case. Frequency band structure of the system is investigated by using the inverse approach to solve the eigenvalue problem and generate dispersion curves when the propagation constant is confined to the first Brillouin zone. The paper is organized as follows: the general mechanical model of periodic and coupled slender structures, Galerkin approximation procedure, Floquet-Bloch theorem and definition of the eigenvalue problem are presented in Section 2. The particular problem of wave propagation in an array of vertically aligned and elastically connected Rayleigh beams given in the so-called "diatomic" and "triatomic" unit cell configurations is detailed in Section 3. Section 4 shows the validation study of the methodology based on Galerkin approximation by using the finite element model, and the parametric study of the influence of coupling medium stiffness, concentrated masses and beam's boundary conditions on the frequency band structure of the proposed coupled beam-mass system.

2. Mathematical preliminaries

In order to analyze the free wave propagation in elastically connected structures such as beams, plates, strings or membranes, different approaches to discretize partial differential equations are used in the literature. The exact solutions of wave propagation problems in structural mechanics are difficult to find due to model complexities, such as specific boundary conditions, shape of structural elements, concentrated masses, attached vibration absorbers, etc. Therefore, application of approximate methods such as Rayleigh's, Rayleigh-Ritz or Galerkin approximation method can play an important role in solving the corresponding eigenvalue problems by approximating solutions using a finite number of mode shapes as admissible functions [52].

Here, we focus our attention to application of the Galerkin approximation in combination with Floquet-Bloch theorem to solve the corresponding eigenvalue problem. Typical unit cells of the proposed periodic system can be modelled as the diatomic and triatomic chains, composed of, respectively, two and three elastically connected structural elements such as beams or plates, Fig. 1.

2.1. The Galerkin approximation and inverse Floquet-Bloch formalism

The Galerkin approximation method belongs to a special group of weighted residual methods. The general solution of the problem is given as a linear combination of trial functions, which are chosen such that they exactly satisfy the corresponding boundary conditions.

Let us consider the m-th unit cell of an array of elastically connected slender structures, which is composed of several structural elements with each one having different material (density) or geometrical properties (thickness) than others. It is assumed that waves propagate only along the array of structural elements i.e. in the direction normal to the structures' length/surface, which is denoted by wavy line in Fig. 1. The general unit cell model of such systems is governed by the following equations of motion

$$\epsilon_i(x)\frac{\partial^2 w_i(x,t)}{\partial t^2} + \Pi_i[w_i(x,t)] + \Pi_{i+1}[w_{i+1}(x,t)] + \Pi_{i-1}[w_{i-1}(x,t)] = f_i(x,t), \quad i = 1,\ldots,p, \tag{1}$$

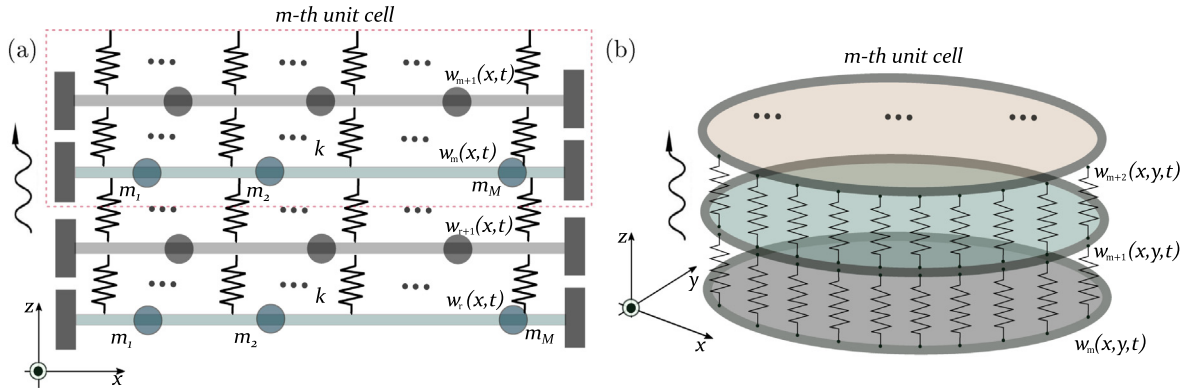

Fig. 1. The structural elastic models of unit cells proposed for: (a) a multi-beam-mass system formed as a diatomic unit cell and (b) a multi-plate system modelled as a triatomic unit cell. The wavy line shows the direction of the wave propagation through the periodic slender structures.

where p denotes the number of structures in a chosen unit cell, $\epsilon_i(x)$ is the inertia term of the considered element and $f_i(x,t)$ is the external excitation. When $p=2$ the system is named diatomic chain and for $p=3$ it is called triatomic chain [53]. The masses of the beams within a cell differ due to different geometrical and material properties or a different number of attached concentrated masses. Assuming the solution of $w_i(x,t)$ in the form of a series of N comparison functions and time generalized coordinates yields

$$w_i(x,t)=\sum_{k=1}^{N} q_{(i)k}(t)\phi_k(x)=\mathbf{C}\mathbf{q}_i, \quad i=1,\ldots,p, \tag{2}$$

in which $\mathbf{q}_i=[q_{(i)1}(t),q_{(i)2}(t),\ldots,q_{(i)N}(t)]^T$ represents the vector of time functions of the i-th structural element and $\mathbf{C}=[\phi_1(x),\phi_2(x),\ldots,\phi_N(x)]$ is the vector of the assumed mode shapes that satisfy the geometric and natural boundary conditions, and which are differentiable at least up to the highest order of spacial derivative in the differential equation of motion Eq. (1). The same boundary conditions are applied to all structural elements in the system. In general, the approximated solution Eq. (2) satisfies all boundary conditions of the unit cell except for the equations of motion Eq. (1). By introducing Eq. (2) into the differential equation of motion Eq. (1), the resulting equation will define the i-th residue as

$$\ell_i(x,t) := \epsilon_i(x)\mathbf{C}\ddot{\mathbf{q}}_i+\Pi_i[\mathbf{C}]\mathbf{q}_i+\Pi_{i+1}[\mathbf{C}]\mathbf{q}_{i+1}+\Pi_{i-1}[\mathbf{C}]\mathbf{q}_{i-1}-f_i(x,t)=0, \quad i=1,\ldots,p, \tag{3}$$

where $\Pi_i[\mathbf{C}]=(\Pi_i[\phi_1(x)],\Pi_i[\phi_2(x)],\ldots,\Pi_i[\phi_N(x)])$. It should be noted that all the residuals will be equal to zero because trial solution is composed of comparison functions that satisfy all the boundary conditions. According to the criteria of the Galerkin method, all residuals should be small. In other words, residue should have zero projection on the chosen basis functions $\phi_j(x)$, $j=1,\ldots,N$ since approximated solution is placed in finite N-dimensional space. For the case of m unit cells, which depends on the number of structural components, the solution will be extended to a number p. Therefore, multiplying the i-th residual by comparison functions and then integrating their product over the domain of a specific structural components gives

$$<\ell_i(x,t),\phi_j(x)> := \int_0^l \ell_i(x,t)\phi_j(x)dx=0, \quad j=1,\ldots,N, \quad i=1,\ldots,p. \tag{4}$$

Introducing the expression Eq. (3) into Eq. (4) and after integration, the set of ordinary differential equation appears with the corresponding mass and stiffness matrices in the following form

$$\mathbf{M}_i\ddot{\mathbf{q}}_i+\mathbf{K}_i\mathbf{q}_i+\mathbf{K}_{i+1}\mathbf{q}_{i+1}+\mathbf{K}_{i-1}\mathbf{q}_{i-1}=\mathbf{f}_i, \quad i=1,\ldots,p, \tag{5}$$

where the elements of the mass and stiffness matrices and the force vector are determined as

$$\begin{aligned}&\mathbf{M}_i=\int_0^l \epsilon_i(x)\mathbf{C}^T\mathbf{C}dx, \quad \mathbf{K}_i=\int_0^l \mathbf{C}^T\Pi_i[\mathbf{C}]dx, \quad i=1,\ldots,p,\\ &\mathbf{K}_{i+1}=\int_0^l \mathbf{C}^T\Pi_{i+1}[\mathbf{C}]dx, \quad \mathbf{K}_{i-1}=\int_0^l \mathbf{C}^T\Pi_{i-1}[\mathbf{C}]dx, \quad \mathbf{f}_i=\int_0^l \mathbf{C}^T f_i dx.\end{aligned} \tag{6}$$

In general, for the m-th unit cell composed of p structural elements it holds

$$\mathbf{M}_m\ddot{\mathbf{q}}_m(t)+\mathbf{K}_m\mathbf{q}_m(t)+\mathbf{K}_{m+1}\mathbf{q}_{m+1}(t)+\mathbf{K}_{m-1}\mathbf{q}_{m-1}(t)=\mathbf{F}_m, \tag{7}$$

where the mass and stiffness matrices of the unit cell are given in Appendix A. The generalized time coordinates are given as $\mathbf{q}_m=[q_{(1)1}(t),\ldots,q_{(1)N}(t),\ldots,q_{(p)1}(t)\ldots,q_{(p)N}(t)]^T$. To analyze the wave propagation, the harmonic solution is assumed by neglecting the vector of external forces. Assuming that $\mathbf{q}_m(t)=\bar{\mathbf{q}}_m e^{j\omega t}$ and introducing it in Eq. (7), yields

$$(\mathbf{K}_m - \omega^2\mathbf{M}_m)\bar{\mathbf{q}}_m + \mathbf{K}_{m+1}\bar{\mathbf{q}}_{m+1} + \mathbf{K}_{m-1}\bar{\mathbf{q}}_{m-1} = \mathbf{0}. \tag{8}$$

It is also assumed that unit cells are repeating periodically in the thickness direction i.e. normal to the length/surface of the structural elements. Note that a unit cell and its neighbors in Eq. (8) may be identified by $\mathbf{K}_m = \mathbf{K}_u$, where $\mathbf{K}_u$ with $u = -1, 0, 1$ denotes the previous, present and subsequent unit cell, respectively as given in [29].

For determination of dispersion characteristics of the system, the inverse method is introduced as given in [29,37]. The dispersion curves are given by the wave frequency ω as a function of propagation constant μ. By considering the undamped Bloch wave propagation, the corresponding eigenvalue problem can be formulated by using the expression given in Eq. (8). However, only the real part of the dispersion curve without attenuation is observed.

To obtain the frequency band structure, i.e. dispersion diagrams, the solution procedure based on the Floquet-Bloch theorem [29] is applied to Eq. (8). The assumed plane wave solution is defined as

$$\bar{\mathbf{q}}_m(\omega) = \tilde{\mathbf{q}}(\mu)e^{jm\mu}, \tag{9}$$

in which the value of the propagation constant μ is pre-set. Inserting the assumed plane wave solution Eq. (9) into Eq. (8) yields the following linear eigenvalue problem

$$(\mathbf{K} - \omega^2\mathbf{M})\tilde{\mathbf{q}}(\mu)e^{jm\mu} = \mathbf{0}, \tag{10}$$

where the overall stiffness matrix is derived as

$$\mathbf{K} = \mathbf{K}_{-1}e^{-j\mu} + \mathbf{K}_0 + \mathbf{K}_{+1}e^{+j\mu} = \sum_{u=-1,0,1}\left(\mathbf{K}_u e^{ju\mu}\right). \tag{11}$$

The solution of the eigenvalue problem for the m-th unit cell obtained in Eq. (10) gives corresponding dispersion diagrams. Solution of this problem requires the propagation constant μ to be known, which is taken within the First Brillouin Zone (FBZ) fundamental period of the dispersion relation, determined for one-dimensional periodic structures in the range $-\pi \leqslant \mu \leqslant \pi$, [53]. As stated in [29], for the wave propagation in periodic structures without attenuation, the wave propagation constant μ corresponds to a real value. On the other hand, the imaginary values of the propagation constant μ are related to the spatial decay of the wave amplitude as the wave propagates through a periodic structure. The number of dispersion curves resulting from the solution of the eigenvalue problem directly depends on the number of connected structural elements (p) in the unit cell and the number of considered terms in the Galerkin approximation (N). The band structure defines the position and width of pass and stop bands (bandgaps). It is well known that the pass-bands are related to the frequency ranges where an elastic wave propagates through the periodic structure, while bandgaps are frequency ranges where waves are attenuated.

3. Problem formulation

3.1. Motion equations of an array of elastically connected beams

In this section, an example of a periodic structure based on elastically coupled beams with concentrated masses is presented to demonstrate the efficiency of the approach based on the Galerkin approximation and Floquet-Bloch theorem. It is well known that classical Euler-Bernoulli beam theory is often used for accurate modelling of long and slender beams, whereas to accurately predict frequencies at higher modes of thick and short beams one should use higher order theories such as Timoshenko's beam theory. Lord Rayleigh developed simpler theory that includes the rotary inertia effect but without the complexity of the Timoshenko's beam theory. Nevertheless, Rayleigh's beam theory can predict response of slender beam structures with a satisfying accuracy.

Introducing the heterogeneity in the system is a major requirement to obtain the wave dispersion properties, which is achieved by taking into account diatomic and triatomic unit cell configurations with two and three elastically connected beams, respectively, having different material or geometrical properties such as density or beam's height. It is assumed that unit cells are periodically distributed in z- direction to infinity, as shown in Fig. 2. Moreover, identical boundary conditions are assumed for all beams within the system (unit cells), which are mutually connected through the continuously distributed springs i.e. Winkler's type of elastic medium. In this analysis, two types of beam's boundary conditions were considered: clamped-free (Fig. 2(a)) and simply supported (Fig. 2(b)).

By introducing the assumptions from the Rayleigh's beam theory [13,52], the governing equation of motion for the infinite periodic system, with p structural elements in the unit cell, can be derived by using the Hamilton's principle as

$$\begin{aligned} &E_{si}I_{si}\tfrac{\partial^4 w_{si}}{\partial x^4} + k(w_{si} - w_{(s-1)(i-1)}) + k(w_{si} - w_{(s+1)(i+1)}) - \rho_{si}I_{si}\tfrac{\partial^4 w_{si}}{\partial t^2 \partial x^2} \\ &\quad + \left[\rho_{si}A_{si} + \sum_{b=1}^{M_{si}} M_{b(si)}\delta(x - a_{b(si)})\right]\tfrac{\partial^2 w_{si}}{\partial t^2} = f_{si}(x,t), \end{aligned} \tag{12}$$

where $w_{si} = w_{si}(x,t)$ and $f_{si} = f_{si}(x,t)$ are the transverse displacement and external load, respectively of the s-th beam in the multiple beam system, and i-th beam in the unit cell, while k is the stiffness of Winkler's elastic medium. The indices i and s

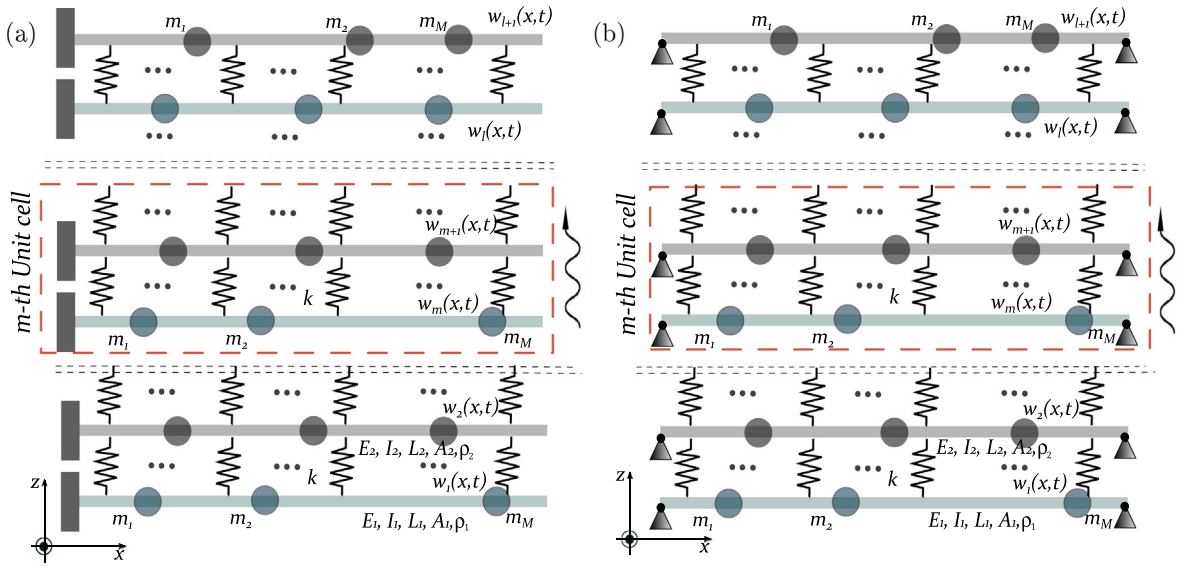

Fig. 2. Periodic system of elastically connected Rayleigh beams with concentrated masses (a) the clamped-free and (b) the simply-supported boundary conditions. The unit cell composed of two elastically connected Rayleigh beams is named diatomic cell.

can take the following values, $s = 1, 2, 3 \ldots$and $i = 1, 2, \ldots, p$, where p is the number of beams in the unit cell. The material and geometrical characteristics of the si-th beam are given by Young's modulus E_{si} , mass density ρ_{si}, cross-sectional area A_{si} and moment of inertia I_{si}. The term $M_{b(si)}$ denotes the b-th attached point mass on the position $a_{b(si)}$ in the axial direction of each beam in the system.

The adopted boundary conditions for clamped-free (CF) and simply-supported (SS) beams are given as

$$w_{si}(0,t) = \frac{\partial w_{si}(0,t)}{\partial x} = \frac{\partial^2 w_{si}(L,t)}{\partial x^2} = \frac{\partial^3 w_{si}(L,t)}{\partial x^3} = 0, \tag{13}$$

and

$$w_{si}(0,t) = \frac{\partial^2 w_{si}(0,t)}{\partial x^2} = w_{si}(L,t) = \frac{\partial^2 w_{si}(L,t)}{\partial x^2} = 0. \tag{14}$$

The initial conditions are taken to be zero.

Taking into consideration the m-th unit cell of the periodic structure modeled as diatomic $p = 2$ and triatomic $p = 3$ system, the governing equations can be reduced to

diatomic unit cell:

$$E_1 I_1 \frac{\partial^4 w_m}{\partial x^4} + k(w_m - w_{m-1}) + k(w_m - w_{m+1}) + \left[\rho_1 A_1 + \sum_{b=1}^{M_1} M_{b(1)}\delta(x - a_{b(1)})\right]\frac{\partial^2 w_m}{\partial t^2} - \rho_1 I_1 \frac{\partial^4 w_m}{\partial t^2 \partial x^2} = f_m(x,t), \tag{15}$$

$$E_2 I_2 \frac{\partial^4 w_{m+1}}{\partial x^4} + k(w_{m+1} - w_m) + k(w_{m+1} - w_{m+2}) + \left[\rho_2 A_2 + \sum_{b=1}^{M_2} M_{b(2)}\delta(x - a_{b(2)})\right]\frac{\partial^2 w_{m+1}}{\partial t^2} - \rho_2 I_2 \frac{\partial^4 w_{m+1}}{\partial t^2 \partial x^2} = f_{m+1}(x,t), \tag{16}$$

triatomic unit cell:

$$E_1 I_1 \frac{\partial^4 w_m}{\partial x^4} + k(w_m - w_{m-1}) + k(w_m - w_{m+1}) + \left[\rho_1 A_1 + \sum_{b=1}^{M_1} M_{b(1)}\delta(x - a_{b(1)})\right]\frac{\partial^2 w_m}{\partial t^2} - \rho_1 I_1 \frac{\partial^4 w_m}{\partial t^2 \partial x^2} = f_m(x,t), \tag{17}$$

$$E_2I_2\frac{\partial^4 w_{m+1}}{\partial x^4}+k(w_{m+1}-w_m)+k(w_{m+1}-w_{m+2})+ \tag{18}$$
$$\left[\rho_2A_2+\sum_{p=1}^{M_2}M_{b(2)}\delta(x-a_{b(2)})\right]\frac{\partial^2 w_{m+1}}{\partial t^2}-\rho_2I_2\frac{\partial^4 w_{m+1}}{\partial t^2\partial x^2}=f_{m+1}(x,t),$$

$$E_3I_3\frac{\partial^4 w_{m+2}}{\partial x^4}+k(w_{m+2}-w_{m+1})+k(w_{m+2}-w_{m+3})+ \tag{19}$$
$$\left[\rho_3A_3+\sum_{p=1}^{M_3}M_{b(3)}\delta(x-a_{b(3)})\right]\frac{\partial^2 w_{m+2}}{\partial t^2}-\rho_3I_3\frac{\partial^4 w_{m+2}}{\partial t^2\partial x^2}=f_{m+2}(x,t).$$

3.2. Defining the eigenvalue problem

In order to analyse the free wave propagation through the periodic structure, the approach based on the Galerkin discretization and Floquet-Bloch theorem is applied for the chosen unit cell defined in the previous section. The main objective is to determine the band structures by detecting stop and pass bands in order to demonstrate the applicability of the presented methodology. In the following, derivations are given for the diatomic chain system, which can be easily extended to the triatomic case.

The first step is to discretize the motion equations of the unit cell by using the Galerkin approximation, which for the $i-th$ beam in the $m-th$ unit cell is defined as

$$w_i(x,t)=\sum_{k=1}^{N}q_{(i)k}(t)\phi_k(x),\quad i=1,\dots,p, \tag{20}$$

where $q_{(i)k}(t)$ and $\phi_k(x)$ are the $k-th$ generalized time function and assumed trial (mode shape) function of the $i-th$ beam. N is the number of terms in the Galerkin approximation series. Inserting Eq. (20) into the equations for unit cell Eq. (15)–(19) yields

$$\begin{aligned}&\sum_{k=1}^{N}E_iI_iq_{(i)k}\phi_k''''+\sum_{k=1}^{N}2kq_{(i)k}\phi_k+\sum_{k=1}^{N}\left[\rho_iA_i+\sum_{b=1}^{M_i}M_{b(i)}\delta(x-a_{b(i)})\right]\ddot{q}_{(i)k}\phi_k-\\&-\sum_{k=1}^{N}\rho_iI_i\ddot{q}_{(i)k}\phi_k''-\sum_{k=1}^{N}kq_{(i-1)k}\phi_k-\sum_{k=1}^{N}kq_{(i+1)k}\phi_k-f_i(x,t)=\ell_i(x,t),\quad i=1,\dots,p,\end{aligned} \tag{21}$$

where ℓ_i is the $i-th$ non-zero residue obtained from the introduced approximated solution. By multiplying the above expression with the $j-th$ trial function ϕ_j for $j=1,2,\dots,N$ and integrating over the beam's length, the following system of equations is obtained

$$\begin{aligned}&\sum_{k=1}^{N}E_iI_i\left(\int_0^L\phi_k''''\phi_j dx\right)q_{(i)k}+\sum_{k=1}^{N}2k\left(\int_0^L\phi_k\phi_j dx\right)q_{(i)k}+\\&+\sum_{k=1}^{N}\left(\int_0^L\left[\rho_iA_i+\sum_{b=1}^{M_i}M_{b(i)}\delta(x-a_{b(i)})\right]\phi_k\phi_j dx\right)\ddot{q}_{(i)k}-\\&-\sum_{k=1}^{N}\rho_iI_i\left(\int_0^L\phi_k''\phi_j dx\right)\ddot{q}_{(i)k}-\sum_{k=1}^{N}k\left(\int_0^L\phi_k\phi_j dx\right)q_{(i-1)k}-\\&-\sum_{k=1}^{N}k\left(\int_0^L\phi_k\phi_j dx\right)q_{(i+1)k}=\left(\int_0^Lf_i(x,t)\phi_j dx\right),\quad i=1,\dots,p.\end{aligned} \tag{22}$$

or in a more compact form as

$$\sum_{k=1}^{N}M_{jk}^{(i)}\ddot{q}_{(i)k}+\sum_{k=1}^{N}K_{jk}^{(i)}q_{(i)k}+\sum_{k=1}^{N}B_{jk}^{(i)}q_{(i+1)k}+\sum_{k=1}^{N}B_{jk}^{(i)}q_{(i-1)k}=F_j^{(i)},\quad i=1,\dots,p., \tag{23}$$

where

$$\begin{aligned}M_{jk}^{(i)}&=\left(\int_0^L\left[\rho_iA_i+\sum_{b=1}^{M_i}M_{b(i)}\delta(x-a_{b(i)})\right]\phi_k\phi_j dx\right)-\rho_iI_i\left(\int_0^L\phi_k''\phi_j dx\right),\\K_{jk}^{(i)}&=E_iI_i\left(\int_0^L\phi_k''''\phi_j dx\right)+2k\left(\int_0^L\phi_k\phi_j dx\right),\\B_{jk}^{(i)}&=-k\left(\int_0^L\phi_k\phi_j dx\right),\quad F_j^{(i)}=\int_0^Lf_i(x,t)\phi_j dx,\quad i=1,\dots,p.\end{aligned} \tag{24}$$

To apply the solution based on the Floquet-Bloch's theorem, the expression given in Eq. (23) should be rewritten in the matrix form that is more convenient for the following analysis. By assuming a harmonic solution for the generalized time functions and neglecting the external load, the system of Eqs. Eq. (23) for $m-th$ unit cell takes a new form

$$\mathbf{D}_m(\omega)\tilde{\mathbf{q}}_m + \mathbf{K}_{m+1}\tilde{\mathbf{q}}_{m+1} + \mathbf{K}_{m-1}\tilde{\mathbf{q}}_{m-1} = \mathbf{0}, \tag{25}$$

where $\mathbf{D}_m(\omega)$ is related to the dynamic stiffness matrix of the unit cell, and matrices $\mathbf{K}_{m+1}$ and $\mathbf{K}_{m-1}$ denote additional stiffness defined for the triatomic chain model as

$$\mathbf{D}_m(\omega) = \left(\begin{bmatrix} \mathbf{K}_1 & \mathbf{0} & \mathbf{0} \\ \mathbf{0} & \mathbf{K}_2 & \mathbf{0} \\ \mathbf{0} & \mathbf{0} & \mathbf{K}_3 \end{bmatrix} - \omega^2 \begin{bmatrix} \mathbf{M}_1 & \mathbf{0} & \mathbf{0} \\ \mathbf{0} & \mathbf{M}_2 & \mathbf{0} \\ \mathbf{0} & \mathbf{0} & \mathbf{M}_3 \end{bmatrix} \right), \tag{26}$$

$$\mathbf{K}_{m+1} = \mathbf{K}_{m-1} = \begin{bmatrix} \mathbf{B}_1 & \mathbf{0} & \mathbf{0} \\ \mathbf{0} & \mathbf{B}_2 & \mathbf{0} \\ \mathbf{0} & \mathbf{0} & \mathbf{B}_3 \end{bmatrix},$$

and the vectors of generalized coordinates are

$$\tilde{\mathbf{q}}_m = \begin{bmatrix} \mathbf{q}_m \\ \mathbf{q}_{m+1} \\ \mathbf{q}_{m+2} \end{bmatrix}, \tilde{\mathbf{q}}_{m-1} = \begin{bmatrix} \mathbf{q}_{m-1} \\ \mathbf{q}_m \\ \mathbf{q}_{m+1} \end{bmatrix}, \tilde{\mathbf{q}}_{m+1} = \begin{bmatrix} \mathbf{q}_{m+1} \\ \mathbf{q}_{m+2} \\ \mathbf{q}_{m+3} \end{bmatrix}. \tag{27}$$

By inserting the solution Eq. (9) into the Eq. (25), the following eigenvalue problem is obtained

$$\tilde{\mathbf{D}}(\omega)\tilde{\mathbf{q}}(\mu)e^{jm\mu} = \mathbf{0}, \tag{28}$$

where the dynamic stiffness matrix is derived as

$$\tilde{\mathbf{D}}(\omega) = \tilde{\mathbf{K}}_{-1}e^{-j\mu} + \tilde{\mathbf{K}}_0 + \tilde{\mathbf{K}}_{+1}e^{+j\mu} - \omega^2\tilde{\mathbf{M}}. \tag{29}$$

Solving the eigenvalue problem Eq. (28) for given values of propagation constant μ, one can obtain the corresponding dispersion curves of the system. It can be noticed that the obtained eigenvalue problems are similar to the ones derived for equivalent discrete models of diatomic and triatomic phononic crystals, having two and three different masses within the unit cell, respectively. Similar conclusions are brought in [31], where topological pumping was studied in a similar system of elastically coupled beams. In this study the main focus is put on the investigation of wave propagation in a heterogeneous systems of elastically connected beams with unit cell configurations having two and three beams of different geometrical or material properties.

4. Numerical study

In this section, the frequency band structures of a periodic system based on multiple elastically connected Raleigh beams with concentrated masses is investigated by using the methodology elaborated in Section 3. Two different unit cell configurations, such as diatomic and triatomic chain systems, are adopted in the numerical study. The results obtained by the Galerkin approximation and Floquet-Bloch theory are validated against the results from the finite element model and those obtained by the frequency response function (FRF). The effects of coupling medium stiffness k and concentrated masses M_p on the band structure of the system are examined in detail. Additionally, the influence of boundary conditions, number of adopted terms in the Galerkin approximation and different unit cell configurations are studied and discussed. To achieve the desired wave dispersion properties, the heterogeneity of the system is introduced by assuming beams in the unit cell with different material or geometrical properties. Numerical simulations are performed for $N = 5$ terms in the Galerkin approximation. Moreover, in validation study, the finite element (FE) method is used to determine the frequency band structure and to compare the results obtained by the Galerkin approximation, where fine agreement is achieved. More details on FE models of multiple beam systems can be found in [54,26]. In the presented study every beam in the unit cell is approximated by considering $n_{ele} = 50$ Rayleigh beam elements.

4.1. Validation

The presented FRF solution is obtained by taking the same number of terms in the Galerkin approximation as in the Floquet-Bloch analysis, and a finite number of unit cells. The following material and geometrical parameters are used in simulations if not specified differently: the cross-sectional area $A = bh$ and the second moment of inertia $I = \frac{bh^3}{12}$for the first beam in the unit cell with height $h = 0.003(\mathrm{m})$ and width $b = 0.02(\mathrm{m})$. Length of all beams in the system is adopted as $L = 0.8(\mathrm{m})$, while mass density of the first beam is given as $\rho = 1190.0(\mathrm{kg/m^3})$, elastic modulus as $E = 3.2 \cdot 10^9(\mathrm{Pa})$ and the number of concentrated masses per beam as $M = 3$, each weighting one third of beam's weight. The positions of attached point masses

are identical for each beam in the system, where $a_b = (\frac{1}{3}, \frac{1}{2}, \frac{2}{3})L$. In order to analyse the harmonic response using FRF, the system with ten connected unit cells is observed. The harmonic force is applied at the middle of the first beam for the simply supported boundary conditions and at the free end of the beam for the clamped-free case. The response is measured at the last beam in the periodic system, where the first beam is those where the coordinate system is placed. The stiffness of the coupling Winkler's type elastic medium is adopted as $k = 100(\mathrm{N/m^2})$. Moreover, Table 1 shows properties of beam elements within the unit cell of a periodic structure in four different configurations with simply supported (SS) and clamped-free (CF) boundary conditions for diatomic and triatomic unit cell configurations. Here, all calculations are given for the normalized frequency given as $\Omega = \omega/\omega_0$, where $\omega_0 = \frac{\pi^2}{L^2}\sqrt{\frac{E_1 I_1}{\rho_1 A_1}}$ is the first natural frequency of the simply-supported beam. Fig. 3 shows comparison of the band structures of systems with elastically connected beams and attached concentrated masses, given in the diatomic and triatomic unit cell configurations, against FRF results of the equivalent system with a finite number of unit cells. Simulations are performed for the five considered terms in the Galerkin approximation and mode shapes of simply supported beams adopted as admissible functions. One can notice similar stop-bands (colored in yellow) and transmission-bands in both the dispersion and FRF diagrams. One can be observe five bandgaps starting from narrower and lower frequency bandgaps and than going to wider and higher frequency bandgaps. In the case of the triatomic configuration given in Fig. 3 b), a higher number of bandgaps can be identified. Here, eight bandgaps can be noticed in the given frequency range in both the dispersion and FRF diagrams. Similar to the previous case, the narrowest bandgap is located at lower frequency dispersion curves while the others are slightly wider. Moreover, in both configurations one can notice a very narrow bandgap at the lowest possible frequency usually named zero-frequency bandgap, whose appearance can be attributed to the presence of the coupling Winkler type of elastic medium [12] or boundary conditions [49]. Additional validation is performed by comparing the dispersion curves obtained via Galerkin approximation and those obtained via the FE model and Floquet-Bloch solution that are marked as red circles in the figures. Comparison of the obtained dispersion characteristics using these two approaches shows excellent agreement of the results.

In Fig. 4, dispersion curves are given for the diatomic and triatomic unit cell configurations of the periodic system of elastically connected beams with five terms in the Galerkin approximation and mode shapes of clamped-free beams adopted as trial functions. One can observe several stop and transmission bands in both diatomic and triatomic configurations and good correspondence between the dispersion curves and FRF responses. It is obvious that lower frequency bandgaps are narrower than those at higher frequency ranges. In the clamped-free case the lower bandgap is shifted to higher frequency than in the simply supported case. The comparison of the Galerkin approximation results with the results from the FE model shows good agreement. The validation demonstrated the applicability, accuracy and simplicity of the proposed approach in analysing the band structure of the complex periodic system of elastically connected Rayleigh beams with concentrated masses that will be used in the following parametric study. Moreover, one can also notice that the introduction of the clamped-free boundary conditions on beams reduces the width of the initial zero-frequency bandgap.

4.2. Parametric study and discussion

The effects of beams' material/geometrical properties and boundary conditions

The effects of different geometrical properties as well as boundary conditions of beams in the unit cell of the proposed periodic system are investigated to reveal their influence on the frequency band structure. To see these effects, first periodic

Table 1
The values of parameters used in simulations of diatomic and triatomic unit cell configurations, whit results plotted in Figs. 3 and 4.

SS boundary conditions				
diatomic UC		triatomic UC		
Beam 1	Beam 2	Beam 1	Beam 2	Beam 3
$E_1 = E$	$E_2 = E$	$E_1 = E$	$E_2 = 2E$	$E_3 = 3E$
$\rho_1 = \rho$	$\rho_2 = \rho$	$\rho_1 = \rho$	$\rho_2 = \rho$	$\rho_3 = \rho$
$I_1 = \frac{bh^3}{12}$	$I_2 = \frac{b(2h)^3}{12}$	$I_1 = \frac{bh^3}{12}$	$I_2 = \frac{b(2h)^3}{12}$	$I_3 = \frac{bh^3}{12}$
$A_1 = bh$	$A_2 = 2bh$	$A_1 = bh$	$A_2 = 2bh$	$A_3 = bh$
$M_b = \frac{1}{3}\rho AL$	$M_b = \frac{1}{3}\rho AL$	$M_b = \frac{1}{2}\rho AL$	$M_b = \frac{1}{2}\rho AL$	$M_b = \frac{1}{2}\rho AL$
CF boundary conditions				
diatomic UC		triatomic UC		
Beam 1	Beam 2	Beam 1	Beam 2	Beam 3
$E_1 = E$	$E_2 = 3E$	$E_1 = E$	$E_2 = 2E$	$E_3 = 3E$
$\rho_1 = \rho$	$\rho_2 = \rho$	$\rho_1 = \rho$	$\rho_2 = \rho$	$\rho_3 = 1.5\rho$
$I_1 = \frac{bh^3}{12}$	$I_2 = \frac{b(2h)^3}{12}$	$I_1 = \frac{bh^3}{12}$	$I_2 = \frac{b(2h)^3}{12}$	$I_3 = \frac{bh^3}{12}$
$A_1 = bh$	$A_2 = 2bh$	$A_1 = bh$	$A_2 = 2bh$	$A_3 = bh$
$M_b = \frac{1}{3}\rho AL$	$M_b = \frac{1}{3}\rho AL$	$M_b = \frac{1}{2}\rho AL$	$M_b = \frac{1}{2}\rho AL$	$M_b = \frac{1}{2}\rho AL$

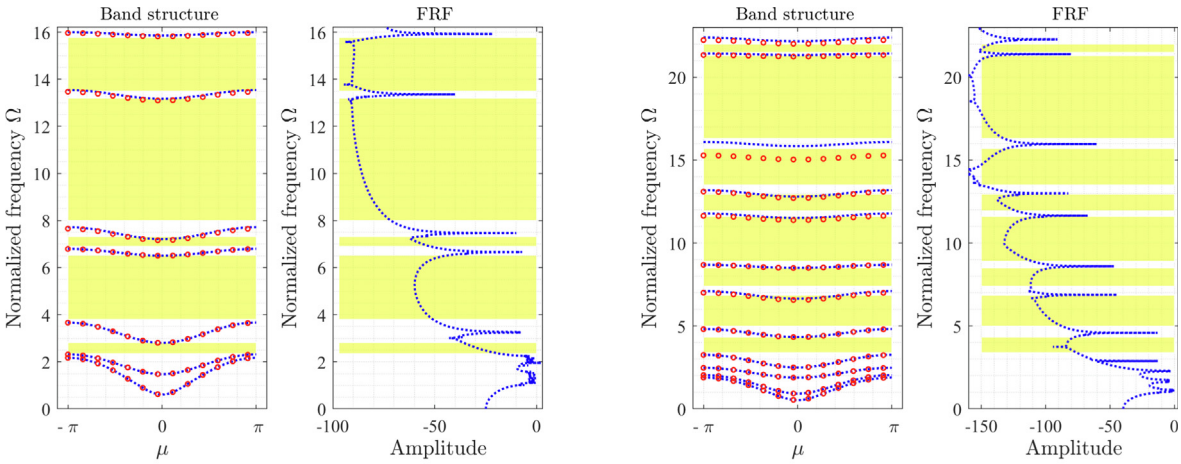

(a) The diatomic unit cell model. (b) The triatomic unit cell model.

Fig. 3. The frequency band structure of the diatomic and triatomic unit cell configurations of the periodic system of elastically connected Rayleigh beams with simply supported boundary conditions and FRF diagrams of the equivalent periodic system with ten unit cells. Blue doted lines are dispersion curves for the five terms in Galerkin approximation and red circles are results from the finite element model. (For interpretation of the references to color in this figure legend, the reader is referred to the web version of this article.)

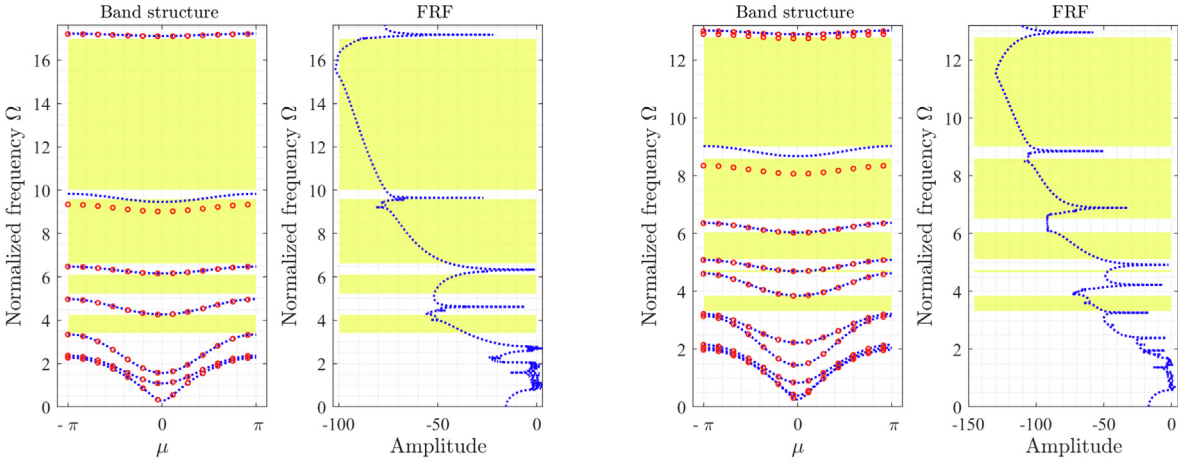

(a) The diatomic unit cell model. (b) The triatomic unit cell model.

Fig. 4. The frequency band structure of the diatomic and triatomic unit cell configurations of the periodic system of elastically connected Rayleigh beams with clamped-free boundary conditions and FRF diagrams of the equivalent periodic system with ten unit cells. Blue doted lines are dispersion curves for the five terms in Galerkin approximation and red circles are results from the finite element model. (For interpretation of the references to color in this figure legend, the reader is referred to the web version of this article.)

systems with diatomic and triatomic unit cell configurations are considered having two and three elastically connected identical beams, respectively for simply-supported and clamped-free boundary conditions, Fig. 5. Here, the same values of parameters as in the validation study are adopted except all the beams have the same cross sectional area, thus, having the same material and geometrical characteristics. The number of adopted terms in the Galerkin approximation is $N = 5$. It can be observed that there are four bandgaps plus the zero-frequency bandgap for the simply-supported boundary conditions case and only three bandgaps in the clamped-free boundary condition case. The reason for the lower number of visible dispersion curves is related to their overlapping due to identical beams in the unit cell having the same eigenfrequency properties. This means that the proposed system with identical unit cells can be represented by a monoatomic unit cell configuration with a single beam, which will generate the same band structure similar to discrete monoatomic chains. Lower bandgaps are narrower compared to the one at higher frequency, whereas the lowest bandgap in the clamped-free case is shifted to higher frequency compared to the simply supported case. In general, the case with identical beams exhibits a great wave attenuation potential since wide bandgaps are achieved with a minimal number of transmission-bands in between.

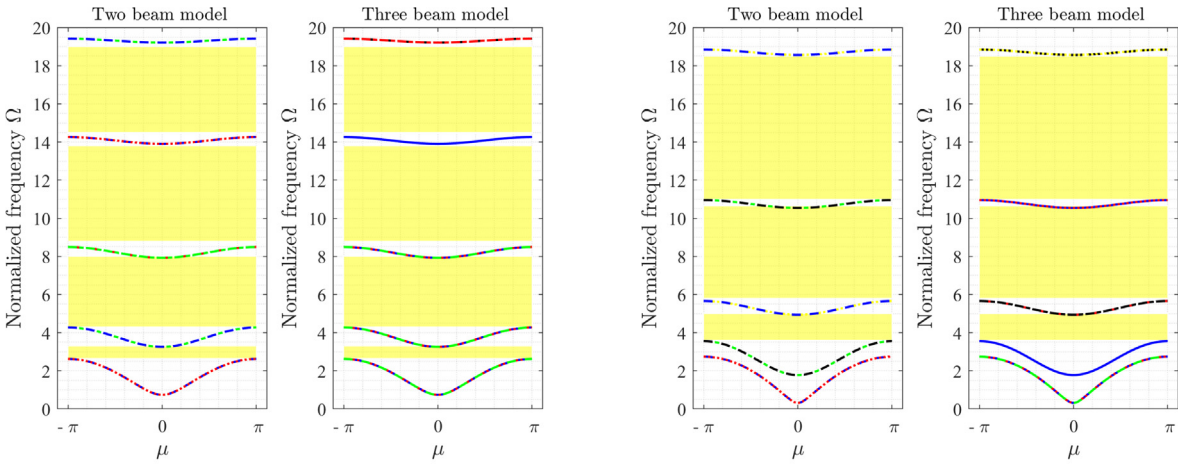

(a) The simply-supported boundary conditions. (b) The clamped-free boundary conditions.

Fig. 5. The frequency band structure of a periodic system with elastically connected beams and concentrated masses determined for five terms considered in Galerkin approximation. The unit cell configurations are based on coupled two and three identical beams, for two types of boundary conditions (a) simply-supported and (b) clamped-free.

The next figure shows the effects of different geometrical (cross sectional area) properties and boundary conditions of beams within the diatomic and tri atomic unit cell configurations on the frequency band structure diagrams. Fig. 6(a) shows eight regular bandgaps and one very narrow zero-frequency bandgap in the diatomic unit cell configuration and nine regular and one narrow zero-frequency bandgap in the triatomic case. The main difference between these two cases is in the number of dispersion curves witch is greater for the triatomic case due to the additional beam introduced in the unit cell. Fig. 6(b) shows the same unit cell models but for the clamped-free boundary conditions. It can be noticed that five bandgaps are obtained in the diatomic configuration and six for the triatomic case. However, additional zero-frequency band gaps in both cases are very narrow, almost invisible. Except for the additional bandgap at highest frequency there is no significant difference in width between other bandgaps. The first bandgap at the lowest frequency is the narrowest, which could be attributed to the local resonance nature of certain bandgaps. Generally, the effect of clamped-free boundary conditions is reflected in the vanishing of one bandgap at lower frequencies and the narrowing of other bandgaps. Different cross sectional areas of beams in Fig. 6 results in their different eifenfrequency properties and consequently in different dispersion characteristics. In this case, there is no overlapping of curves and higher number of dispersion branches can be detected compared to the case with identical beams for the same frequency range.

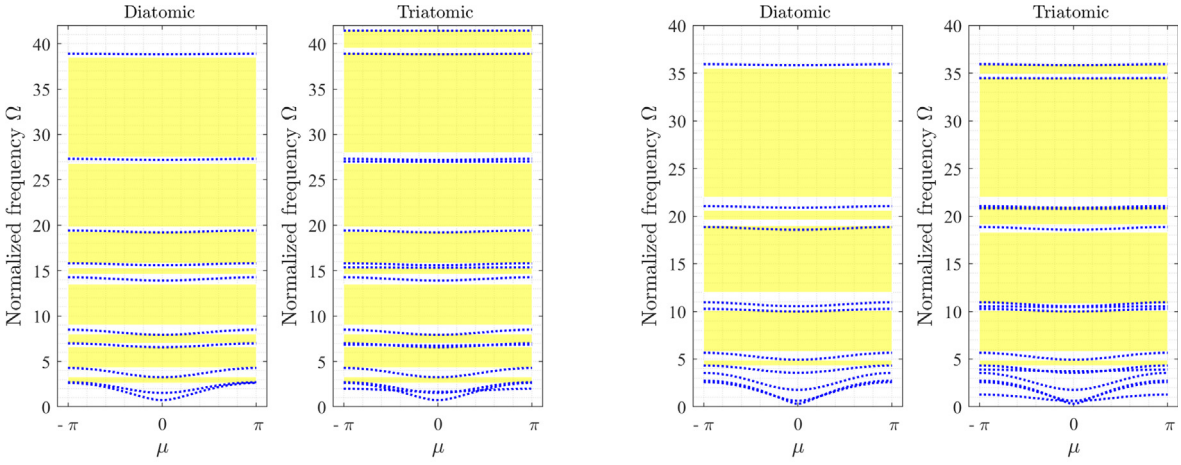

(a) The simply-supported boundary conditions. (b) The clamped-free boundary conditions.

Fig. 6. The frequency band structure of a periodic system with elastically connected beams and concentrated masses determined for five terms considered in the Galerkin approximation. The diatomic and triatomic unit cell configurations are based on coupled two and three beams with different geometrical properties, and for two types of boundary conditions (a) simply-supported and (b) clamped-free.

4.3. The effect of the stiffness of Winkler's coupling medium

Here, the influence of the stiffness of elastic medium on the band structure of the periodic system is investigated for the diatomic and triatomic unit cell configurations and five terms considered in the Galerkin approximation. The values of adopted parameters are the same as those in the validation study, except for the stiffness of the elastic medium. Fig. 7 shows a cross section of the band structure 3D plot for simultaneous change of the propagation constant μ and stiffness of the elastic medium k given in the horizontal axis. One can observe nine bandgaps for lower values of the stiffness parameter (white backgrounds). The first bandgap at the lowest frequency range is the narrowest while the widest one is located at the highest frequency range. The number and width of bandgaps reduces for further increase of the stiffness parameter. From the physical point of view, increasing the stiffness of the Winkler elastic medium increases the overall stiffness of the system. Different band structure can be observed in the case of triatomic unit cell configurations, where one can observe a larger number of bandgaps but with similar behavior when increasing the stiffness parameter. Moreover, Fig. 8 shows equivalent periodic systems but for the clamped-free boundary conditions on beams. This system is even more sensitive to variation of the stiffness parameter whose increase can significantly reduce the number and width of bandgaps. In the triatomic configuration case, there are initially more bangaps but their number is also reduced when increasing the stiffness parameter. Narrow and lower frequency bandgaps can be easily eliminated by increasing the stiffness parameter. The overall characteristic of all presented examples is that transmission bands are very narrow at higher frequencies.

4.4. The effect of concentrated masses

The effect of concentrated masses on dispersion curves of the periodic system of elastically connected beams in diatomic and triatomic unit cell configurations is investigated in this sub-section for five terms in Galerkin approximation. Beams in the unit cell have different cross sectional areas like in the previous examples. The values of parameters are adopted the same as in the validation study except for the values of concentrated masses. The main reason for introducing the concentrated masses is possibility to change the mass distribution and therefore the band structure of the periodic system without changing its geometrical properties. In this analysis, figures are also obtained as a cross section i.e. dispersion surface of a 3D plot obtained by changing the propagation constant μ and values of the attached point masses M_p (horizontal axis).Therefore, Fig. 9 shows the effect of change of concentrated masses on the band structure of the proposed periodic system for simply supported beams. One can observe nine bandgaps (white surfaces) for lower values of masses, including the zero-frequency bandgap. Similar to the previous examples, lower frequency bandgaps are narrower, while those at higher frequencies are wider. An increase of mass decreases the bandgaps' width while the zero-frequency bandgap vanishes. In addition, all the remaining bandgaps are shifted towards lower frequencies due to the well known feature of beam-mass systems that an increase of values of concentrated masses reduces the values of natural frequencies. Similar behaviour can be noticed in both periodic systems with diatomic and the triatomic unit cell configurations, except the latter has greater number of bandgaps. Furthermore, similar tendencies in the band structure behaviour can be observed in Fig. 10 for the same system but with the cantilever beams. In the case of small values of concentrated masses there are six bandgaps including the zero-frequency bandgap. The narrowest bandgap is at the lowest, while the widest is at the highest frequency. However, an

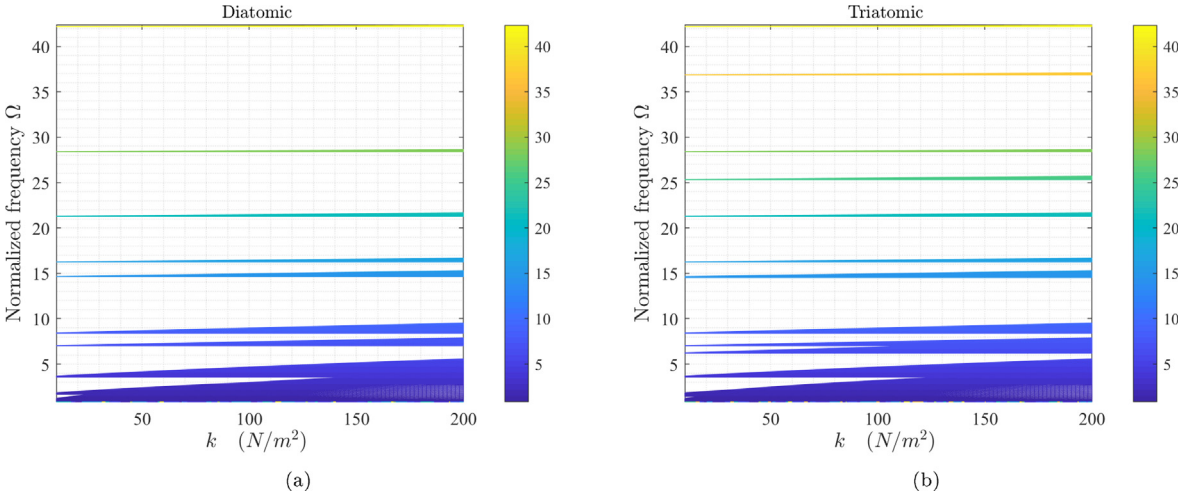

Fig. 7. The cross section of 3D frequency band structure diagrams for five terms in the Galerkin approximation and diatomic and triatomic unit cell configurations with simply supported beams. The surfaces are obtained by solving the eigenvalue problem from Eq. (29) and by changing the propagation constant μ and the stiffness of elastic coupling medium k.

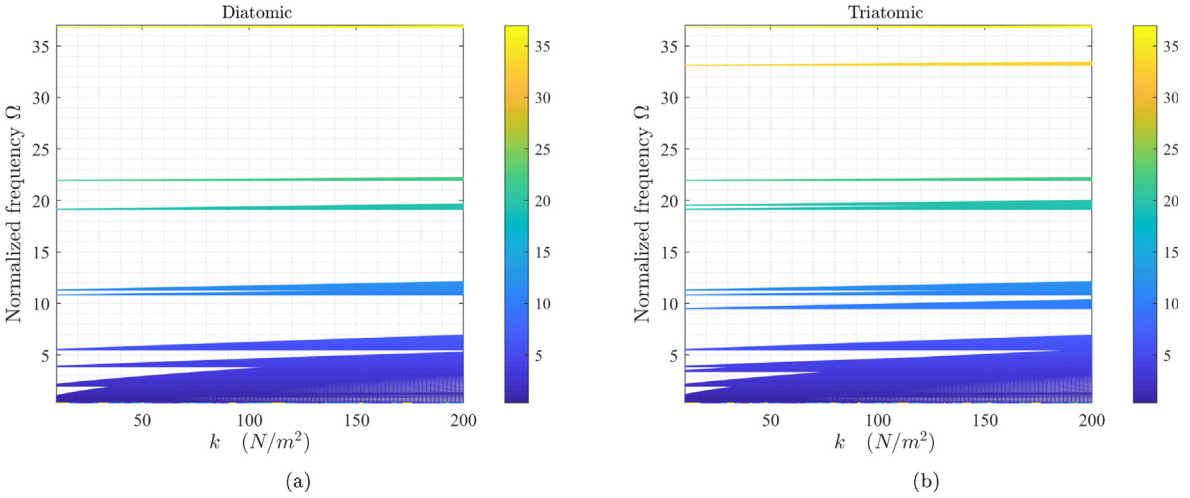

Fig. 8. The cross section of 3D frequency band structure diagrams for five terms in the Galerkin approximation and diatomic and triatomic unit cell configurations with clamped-free beams. The surfaces are obtained by solving the eigenvalue problem from Eq. (29) and by changing the propagation constant μ and the stiffness of elastic coupling medium k.

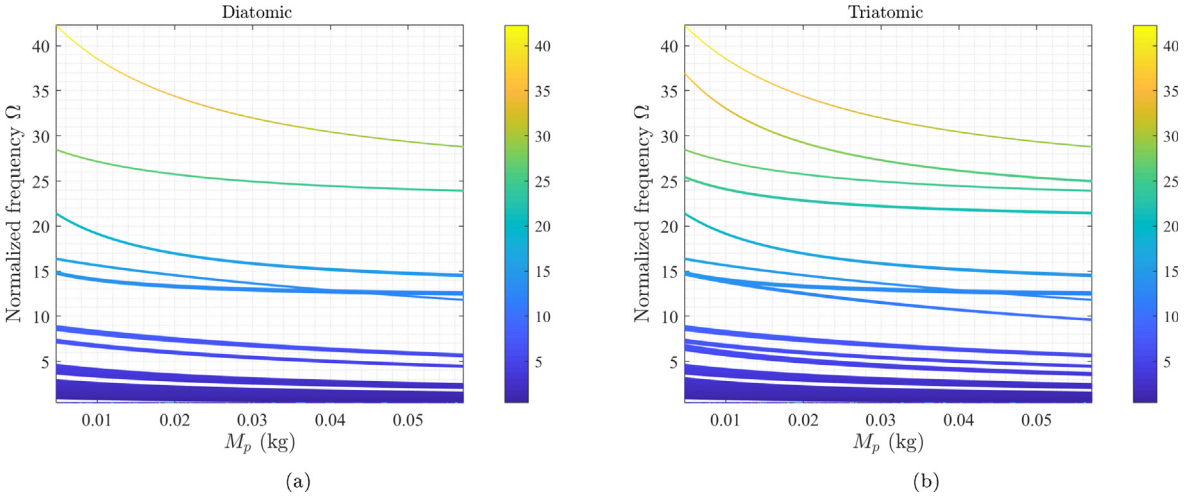

Fig. 9. The cross section of 3D frequency band structure diagrams for five terms in Galerkin approximation and diatomic and triatomic unit cell configurations with simply supported beams. The surfaces are obtained by solving the eigenvalue problem from Eq. (29) and by changing the propagation constant μ and the stiffness of elastic coupling medium M_p.

increase of the mass quickly eliminates the lowest frequency bandgaps, including the zero-frequency bandgap, and it also narrows the others. One can also notice shifting of the bandgaps towards lower values of frequency. However, in the case of triatomic configuration, the frequency ranges and the number of bandgaps for the same values of concentrated masses are different. Moreover, a veering phenomenon can be noticed in frequency dispersion plots, which is known from the literature as a point where dispersion or frequency response curves are approaching each other without crossing and then suddenly diverge one from another. Appearance of this phenomenon strongly depends on the value of concentrated masses attached to beams.

It can be outlined that the main characteristic of the proposed periodic system of elastically connected beams is that the band structure properties can be easily changed by changing the stiffness of coupling medium and values of concentrated masses attached to beams without changing the geometrical features of the system it self. The proposed model also shows the existence of the zero-frequency bandgap, which is more pronounced for the simply supported boundary conditions and certain values of concentrated masses than for the clamped-free case.

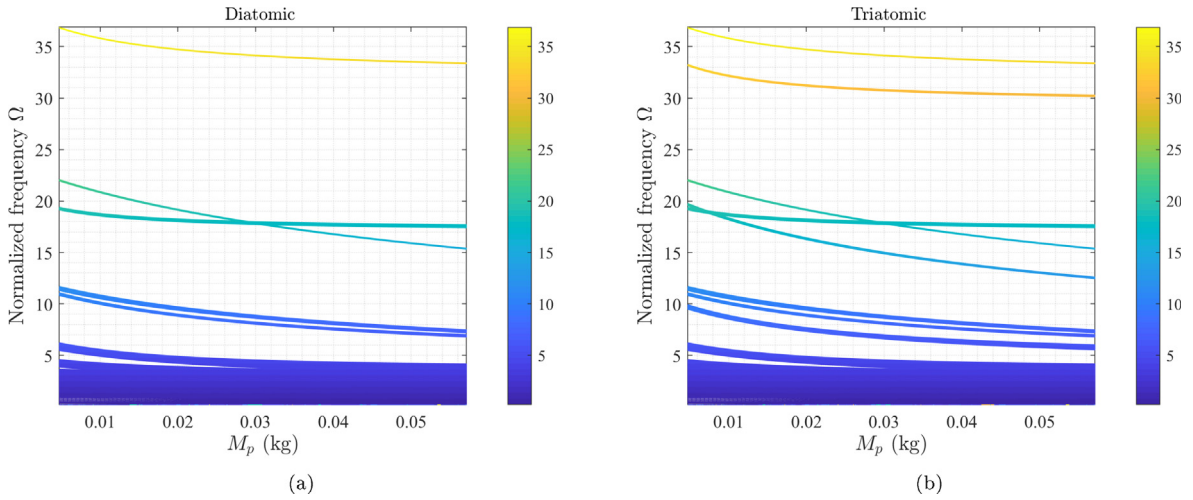

Fig. 10. The cross section of 3D frequency band structure diagrams for five terms in Galerkin approximation and diatomic and triatomic unit cell configurations with clamped-free beams. The surfaces are obtained by solving the eigenvalue problem from Eq. (29) and by changing the propagation constant μ and the stiffness of elastic coupling medium M_p.

5. Conclusions

In this work, Floquet-Bloch theorem and Galerkin approximation are suggested to study wave propagation in periodic systems based on vertically aligned and elastically connected parallel slender structures. A particular attention is devoted to the periodic system given as an array of elastically connected beams with concentrated masses and same boundary conditions. Adjacent beams are coupled through the Winkler's type of elastic medium given as uniformly distributed springs along beam's length. The eigenvalue problem is solved to determine the dispersion curves with the main assumption that the elastic wave propagates along the array of periodically repeating structures i.e. in the direction normal to the length/-surface of structural elements. The frequency band structure diagrams are validated by comparing them with the results from the finite element model and the frequency response function determined for the full model of the periodic system. Parametric study is performed to analyze the effects of different structural parameters on the frequency band structure. The following conclusions can be drawn as a result of the presented study:

- Obtained frequency band structure of the presented periodic system of elastically connected beams reveals great potential for wave attenuation applications.
- Beams boundary conditions and different unit cell configurations have shown a significant influence on the band structure diagrams of the proposed system.
- Variation of elastic medium stiffness parameter and value of concentrated masses revealed that band structure properties can be easily tuned without changing the geometrical properties of the system.

The proposed framework allows the study of more complex systems with elastically coupled structural elements such as plates or membranes. This study shows potential of the proposed periodic systems to be utilized in vibration mitigation and wave attenuation applications. Moreover, the presented model can be useful in future design of topological mechanical metamaterials based on coupled structures systems, which presents an intriguing direction for further research.

CRediT authorship contribution statement

Danilo Karličić: Conceptualization, Methodology, Software. **Milan Cajić:** Writing - original draft, Investigation, Data curation. **Stepa Paunović:** Software, Validation. **Sondipon Adhikari:** Supervision.

Declaration of Competing Interest

The authors declare that they have no known competing financial interests or personal relationships that could have appeared to influence the work reported in this paper.

Acknowledgements

D. Karličić and S. Adhikari were supported by the Marie Sklodowska-Curie Actions — - European Commission: 799201-METACTIVE. M. Cajić and S. Paunović were supported by the Serbian Ministry of Education, Science and Technological Development through the Mathematical Institute of the Serbian Academy of Sciences and Arts.

Appendix A. The mass and stiffness matrices

The mass and stiffness matrices determined in a general case are

$$\mathbf{M}_m = \begin{bmatrix} \mathbf{M}_1 & \mathbf{0} & \mathbf{0} & \mathbf{0} & \dots & \mathbf{0} \\ \mathbf{0} & \mathbf{M}_2 & \mathbf{0} & \mathbf{0} & \dots & \mathbf{0} \\ \mathbf{0} & \mathbf{0} & \mathbf{M}_3 & \mathbf{0} & \dots & \mathbf{0} \\ \dots & \dots & \dots & \mathbf{M}_i & \dots & \mathbf{0} \\ \mathbf{0} & \mathbf{0} & \mathbf{0} & \mathbf{0} & \dots & \mathbf{M}_p \end{bmatrix}_{pN\times pN},$$

$$\mathbf{K}_m = \begin{bmatrix} \mathbf{K}_1 & \mathbf{0} & \mathbf{0} & \mathbf{0} & \dots & \mathbf{0} \\ \mathbf{0} & \mathbf{K}_2 & \mathbf{0} & \mathbf{0} & \dots & \mathbf{0} \\ \mathbf{0} & \mathbf{0} & \mathbf{K}_3 & \mathbf{0} & \dots & \mathbf{0} \\ \dots & \dots & \dots & \mathbf{K}_i & \dots & \mathbf{0} \\ \mathbf{0} & \mathbf{0} & \mathbf{0} & \mathbf{0} & \dots & \mathbf{K}_p \end{bmatrix}_{pN\times pN}, \tag{30}$$

$$\mathbf{K}_{m-1} = \mathbf{K}_{m+1} = \begin{bmatrix} \mathbf{B}_1 & \mathbf{0} & \mathbf{0} & \mathbf{0} & \dots & \mathbf{0} \\ \mathbf{0} & \mathbf{B}_2 & \mathbf{0} & \mathbf{0} & \dots & \mathbf{0} \\ \mathbf{0} & \mathbf{0} & \mathbf{B}_3 & \mathbf{0} & \dots & \mathbf{0} \\ \dots & \dots & \dots & \mathbf{B}_i & \dots & \mathbf{0} \\ \mathbf{0} & \mathbf{0} & \mathbf{0} & \mathbf{0} & \dots & \mathbf{B}_p \end{bmatrix}_{pN\times pN},$$

where p is the number of the structural elements in the unit cell. The size of the matrices $(\mathbf{M}_i, \mathbf{K}_i, \mathbf{B}_i)$ inside of the global mass and stiffness matrices are related to the number of adopted terms in the Galerkin approximation N, and defined in Eq. (6).

References

[1] D. Mead, Wave propagation in continuous periodic structures: research contributions from Southampton, 1964–1995, J. Sound Vib. 190 (3) (1996) 495–524.
[2] D. Mead, A general theory of harmonic wave propagation in linear periodic systems with multiple coupling, J. Sound Vib. 27 (2) (1973) 235–260.
[3] D.J. Mead, A new method of analyzing wave propagation in periodic structures; applications to periodic Timoshenko beams and stiffened plates, J. Sound Vib. 104 (1) (1986) 9–27.
[4] D.J. Mead, The forced vibration of one-dimensional multi-coupled periodic structures: An application to finite element analysis, J. Sound Vib. 319 (1–2) (2009) 282–304.
[5] D. Mead, S. Parthan, Free wave propagation in two-dimensional periodic plates, J. Sound Vib. 64 (3) (1979) 325–348.
[6] G. Carta, M. Brun, Bloch–Floquet waves in flexural systems with continuous and discrete elements, Mech. Mater. 87 (2015) 11–26.
[7] L. Morini, M. Gei, Waves in one-dimensional quasicrystalline structures: dynamical trace mapping, scaling and self-similarity of the spectrum, J. Mech. Phys. Solids 119 (2018) 83–103.
[8] M. Nieves, G. Mishuris, L. Slepyan, Transient wave in a transformable periodic flexural structure, Int. J. Solids Struct. 112 (2017) 185–208.
[9] G. Carta, Effects of compressive load and support damping on the propagation of flexural waves in beams resting on elastic foundation, Arch. Appl. Mech. 82 (9) (2012) 1219–1232.
[10] L. Ding, H.-P. Zhu, L. Wu, Effects of axial load and structural damping on wave propagation in periodic Timoshenko beams on elastic foundations under moving loads, Phys. Lett. A 380 (31–32) (2016) 2335–2341.
[11] M. Nieves, M. Brun, Dynamic characterization of a periodic microstructured flexural system with rotational inertia, Philos. Trans. Roy. Soc. A 377 (2156) (2019) 20190113.
[12] R.K. Pal, M.I. Rosa, M. Ruzzene, Topological bands and localized vibration modes in quasiperiodic beams, New J. Phys. 21 (9) (2019) 093017.
[13] A. Piccolroaz, A. Movchan, Dispersion and localisation in structured rayleigh beams, Int. J. Solids Struct. 51 (25–26) (2014) 4452–4461.
[14] M. Gei, A. Movchan, D. Bigoni, Band-gap shift and defect-induced annihilation in prestressed elastic structures, J. Appl. Phys. 105 (6) (2009) 063507.
[15] G. Bordiga, L. Cabras, D. Bigoni, A. Piccolroaz, Free and forced wave propagation in a rayleigh-beam grid: flat bands, dirac cones, and vibration localization vs isotropization, Int. J. Solids Struct. 161 (2019) 64–81.
[16] J.M. De Ponti, A. Colombi, R. Ardito, F. Braghin, A. Corigliano, R.V. Craster, Graded elastic metasurface for enhanced energy harvesting, New J. Phys. 22 (1) (2020) 013013.
[17] Z. Cheng, W. Lin, Z. Shi, Wave dispersion analysis of multi-story frame building structures using the periodic structure theory, Soil Dyn. Earthquake Eng. 106 (2018) 215–230.
[18] S. Gonella, M. Ruzzene, Homogenization and equivalent in-plane properties of two-dimensional periodic lattices, Int. J. Solids Struct. 45 (10) (2008) 2897–2915.
[19] D. Torrent, J. Sánchez-Dehesa, Acoustic resonances in two-dimensional radial sonic crystal shells, New J. Phys. 12 (7) (2010) 073034.
[20] S. Hajarolasvadi, A.E. Elbanna, Dynamics of metamaterial beams consisting of periodically-coupled parallel flexural elements: a theoretical study, J. Phys. D: Appl. Phys. 52 (31) (2019) 315101.

[21] O. Avila-Pozos, A. Movchan, S. Sorokin, Propagation of elastic waves along interfaces in layered beams, in: IUTAM Symposium on Asymptotics, Singularities and Homogenisation in Problems of Mechanics, Springer, 2003, pp. 53–61.
[22] M. Ruzzene, F. Scarpa, Control of wave propagation in sandwich beams with auxetic core, J. Intell. Mater. Syst. Struct. 14 (7) (2003) 443–453.
[23] M. Serpilli, S. Lenci, Asymptotic modelling of the linear dynamics of laminated beams, Int. J. Solids Struct. 49 (9) (2012) 1147–1157.
[24] H. Saito, H. Tani, Vibrations of bonded beams with a single lap adhesive joint, J. Sound Vib. 92 (2) (1984) 299–309.
[25] W. Brito, C. Maia, A. Mendonca, Bending analysis of elastically connected euler–bernoulli double-beam system using the direct boundary element method, Appl. Math. Model. 74 (2019) 387–408.
[26] S. Paunović, M. Cajić, D. Karličić, M. Mijalković, Dynamics of fractional-order multi-beam mass system excited by base motion, Appl. Math. Model. 80 (2020) 702–723.
[27] D. Karličić, M. Cajić, S. Adhikari, P. Kozić, T. Murmu, Vibrating nonlocal multi-nanoplate system under inplane magnetic field, Eur. J. Mech. A/Solids 64 (2017) 29–45.
[28] P. Martinsson, A. Movchan, Vibrations of lattice structures and phononic band gaps, Q. J. Mech. Appl. Mech. 56 (1) (2003) 45–64.
[29] M.I. Hussein, M.J. Leamy, M. Ruzzene, Dynamics of phononic materials and structures: Historical origins, recent progress, and future outlook, Appl. Mech. Rev. 66 (4) (2014) 040802.
[30] H. Peng, P.F. Pai, Acoustic metamaterial plates for elastic wave absorption and structural vibration suppression, Int. J. Mech. Sci. 89 (2014) 350–361.
[31] M.I. Rosa, R.K. Pal, J.R. Arruda, M. Ruzzene, Edge states and topological pumping in spatially modulated elastic lattices, Phys. Rev. Lett. 123 (3) (2019) 034301.
[32] R.F. Boukadia, C. Droz, M.N. Ichchou, W. Desmet, A bloch wave reduction scheme for ultrafast band diagram and dynamic response computation in periodic structures, Finite Elem. Anal. Des. 148 (2018) 1–12.
[33] M. Sigalas, E. Economou, Elastic waves in plates with periodically placed inclusions, J. Appl. Phys. 75 (6) (1994) 2845–2850.
[34] L. Han, Y. Zhang, Z.-Q. Ni, Z.-M. Zhang, L.-H. Jiang, A modified transfer matrix method for the study of the bending vibration band structure in phononic crystal euler beams, Physica B 407 (23) (2012) 4579–4583.
[35] V. Laude, R.P. Moiseyenko, S. Benchabane, N.F. Declercq, Bloch wave deafness and modal conversion at a phononic crystal boundary, AIP Adv. 1 (4) (2011) 041402.
[36] M.I. Hussein, G.M. Hulbert, R.A. Scott, Dispersive elastodynamics of 1d banded materials and structures: analysis, J. Sound Vib. 289 (4–5) (2006) 779–806.
[37] L. Junyi, D. Balint, An inverse method to determine the dispersion curves of periodic structures based on wave superposition, J. Sound Vib. 350 (2015) 41–72.
[38] G. Shmuel, R. Band, Universality of the frequency spectrum of laminates, J. Mech. Phys. Solids 92 (2016) 127–136.
[39] C. Sugino, S. Leadenham, M. Ruzzene, A. Erturk, On the mechanism of bandgap formation in locally resonant finite elastic metamaterials, J. Appl. Phys. 120 (13) (2016) 134501.
[40] A. Casalotti, S. El-Borgi, W. Lacarbonara, Metamaterial beam with embedded nonlinear vibration absorbers, Int. J. Non-Linear Mech. 98 (2018) 32–42.
[41] E.E. Basta, M. Ghommem, S.A. Emam, Vibration suppression and optimization of conserved-mass metamaterial beam, Int. J. Non-Linear Mech. 120 (2020) 103360.
[42] C. Sugino, Y. Xia, S. Leadenham, M. Ruzzene, A. Erturk, A general theory for bandgap estimation in locally resonant metastructures, J. Sound Vib. 406 (2017) 104–123.
[43] Y. Xiao, J. Wen, X. Wen, Longitudinal wave band gaps in metamaterial-based elastic rods containing multi-degree-of-freedom resonators, New J. Phys. 14 (3) (2012) 033042.
[44] Z. Liu, X. Zhang, Y. Mao, Y. Zhu, Z. Yang, C.T. Chan, P. Sheng, Locally resonant sonic materials, Science 289 (5485) (2000) 1734–1736.
[45] R. Zhu, G. Huang, G. Hu, Effective dynamic properties and multi-resonant design of acoustic metamaterials, J. Vib. Acoust. 134 (3) (2012) 031006.
[46] L. Raghavan, A.S. Phani, Local resonance bandgaps in periodic media: Theory and experiment, J. Acoust. Soc. Am. 134 (3) (2013) 1950–1959.
[47] Y. Xiao, J. Wen, G. Wang, X. Wen, Theoretical and experimental study of locally resonant and bragg band gaps in flexural beams carrying periodic arrays of beam-like resonators, J. Vib. Acoust. 135 (4) (2013) 041006.
[48] L. Liu, M.I. Hussein, Wave motion in periodic flexural beams and characterization of the transition between bragg scattering and local resonance, J. Appl. Mech. 79 (1) (2012) 011003.
[49] Y. Achaoui, T. Antonakakis, S. Brûlé, R. Craster, S. Enoch, S. Guenneau, Clamped seismic metamaterials: ultra-low frequency stop bands, New J. Phys. 19 (6) (2017) 063022.
[50] D. Bigoni, A. Movchan, Statics and dynamics of structural interfaces in elasticity, Int. J. Solids Struct. 39 (19) (2002) 4843–4865.
[51] M. Brun, S. Guenneau, A.B. Movchan, D. Bigoni, Dynamics of structural interfaces: filtering and focussing effects for elastic waves, J. Mech. Phys. Solids 58 (9) (2010) 1212–1224.
[52] P. Hagedorn, A. DasGupta, Vibrations and waves in continuous mechanical systems, Wiley Online Library, 2007.
[53] C. Kittel, P. McEuen, P. McEuen, Introduction to solid state physics, vol. 8, Wiley, New York, 1996.
[54] T. Chatterjee, D. Karličić, S. Adhikari, M.I. Friswell, Gaussian process assisted stochastic dynamic analysis with applications to near-periodic structures, Mech. Syst. Signal Process. 149 (2021) 107218.

Extreme Mechanics Letters 40 (2020) 100934

Contents lists available at ScienceDirect

Extreme Mechanics Letters

journal homepage: www.elsevier.com/locate/eml

Anisotropy tailoring in geometrically isotropic multi-material lattices

T. Mukhopadhyay [a,*], S. Naskar [b], S. Adhikari [c]

[a] Department of Aerospace Engineering, Indian Institute of Technology Kanpur, Kanpur, India
[b] Department of Aerospace Engineering, Indian Institute of Technology Bombay, Mumbai, India
[c] College of Engineering, Swansea University, Swansea, UK

ARTICLE INFO

Article history:
Received 31 May 2020
Received in revised form 10 August 2020
Accepted 11 August 2020
Available online 9 September 2020

Keywords:
Anisotropy tailoring
Multi-material lattices
Elastic properties
Lattice materials
Honeycomb microstructures
Periodic structures

ABSTRACT

This article proposes the concept of anisotropy tailoring in multi-material lattices based on a mechanics-based bottom-up framework. It is widely known that isotropy in a mono-material lattice can be obtained when the microstructure has an isotropic geometry. For example, regular hexagonal lattices with a unit cell comprised of six equal members and equal internal angle of 120° each, show isotropy in the elastic properties. Such limited microstructural configuration space for having isotropy severely restricts the scope of many multi-functional applications such as space filling in 3D printing. We first demonstrate that there are multiple structural geometries in mono-material lattices that could lead to isotropy. It is shown that the configuration space for isotropy can be expanded by multiple folds when more than one intrinsic material is introduced in the unit cell of a lattice. We explicitly demonstrate different degrees of anisotropy in regular geometrically isotropic lattices by introducing the multi-material architecture. The contours of achieving minimum anisotropy, maximum anisotropy and a fixed value of anisotropy are presented in the design space consisting of geometric and multi-material parameters. Proposition of such multi-material microstructures could essentially expand the multi-functional design scope significantly, offering a higher degree of flexibility to the designer in terms of choosing (or identifying) the most suitable microstructural geometry. An explicit theoretical characterization of the contours of anisotropy along with physical insights underpinning the configuration space of multi-material and geometric parameters will accelerate the process of its potential exploitation in various engineered multi-functional materials and structural systems across different length-scales with the demand of any specific degree of anisotropy but limitation in the micro-structural geometry.

1. Introduction

Lattice based periodic material microstructures provide an unprecedented opportunity to artificially engineer the global mechanical properties of materials based on multi-functional demands of modern structural systems by identifying (or designing) the intrinsic material distribution and structural geometry at micro-scale. In such microstructured materials the tailorable effective macro-scale mechanical properties (such as equivalent elastic moduli, deformation, buckling, energy absorption, vibration and wave propagation characteristics with modulation features) are defined by the structural configuration along with intrinsic material properties of the constituent members. Even though a limited number of natural systems can show few unusual properties (for example, lightweight bone structures, and auxeticity in various crystalline materials), the scope of having multiple desired mechanical properties to the optimum level in a single natural material is rare. Most of the naturally occurring materials cannot exhibit one or more of the fascinating multi-functional properties like negative Poisson's ratio, extremely lightweight characteristics, negative stiffness, pentamode material characteristics (meta-fluid), programmable constitutive laws etc., which can be achieved by an intelligent and intuitive microstructural design [1–9]. For example, the conventional positive effective Poisson's ratio in a hexagonal lattice can be converted to negative by considering the cell angle θ in Fig. 1 as negative (as indicated in figure 1(C–D) of the supplementary material), or to a 'zero' value by intuitively designing the hexagonal unit cell [10,11]. Recently buckling-induced instability has been utilized to obtain and modulate unusual mechanical properties like enhanced energy absorption capacity and strain rate dependent constitutive behaviour [12–14]. Besides static properties, various unusual and useful properties can be realized in metamaterials under dynamic condition, such as negative bulk modulus [15], negative mass density [16], negative Young's modulus [17], negative shear modulus [18] and elastic cloaks [19]. These novel class of artificially engineered materials with tailorable bespoke

* Corresponding author.
E-mail address: tanmoy@iitk.ac.in (T. Mukhopadhyay).

https://doi.org/10.1016/j.eml.2020.100934
2352-4316/

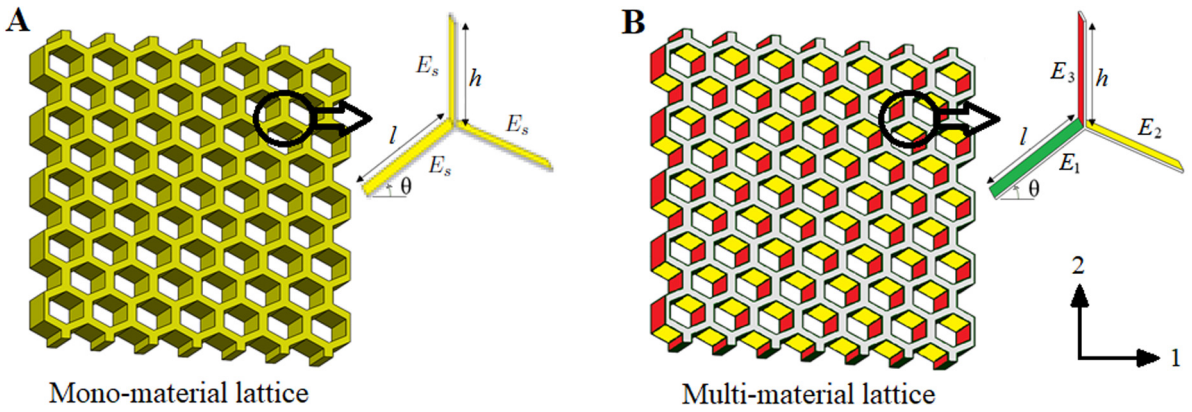

Fig. 1. Multi-material microstructure. (A) Mono-material hexagonal lattice where all the members in a unit cell are made of same material **(B)** Multi-material hexagonal lattice where the three constituting members in a unit cell are made of three different materials (as indicated by separate colours). The respective unit cells with dimensions are shown using insets. Unit cell of a multi-material lattice has three different intrinsic material properties corresponding to the three constituting beam elements (E_1, E_2 and E_3). In case of unit cell of the mono-material lattice $E_1 = E_2 = E_3 = E_s$. In the mono-material and multi-material lattice configurations shown here, if θ becomes negative, the lattice will become re-entrant that can show auxeticity i.e. negative Poisson's ratio (refer to figure 1(C–D) of the supplementary material). The fundamental mechanics of such lattices are normally scale-independent across micro to macro scales. From a multi-scale point of view, even though there exists a lattice structure at microscale, the mechanical properties at macroscale could be idealized to have equivalent values of a bulk continuum-like solid for further analysis. Therefore, for a structural analysis at macroscale, one only needs to consider the effective macroscale mechanical properties without bothering about the microstructural geometry. (For interpretation of the references to colour in this figure legend, the reader is referred to the web version of this article.)

properties have tremendous potential for applications in futuristic multi-functional aerospace, mechanical, civil, electronics and biomedical systems.

In lattice metamaterials two material properties are involved at two different length-scales. One is the intrinsic material(s) which is actually the material of the constituting elements (such as the connecting beam members shown in Fig. 1) at micro-scale. These materials are either naturally occurring monolithic materials or their alloys and compounds. The intrinsic mechanical properties depend on the chemical composition, atomic and molecular structure of that material. The second set of material properties correspond to the effective macro-scale behaviour of the entire lattice. Such macro-scale properties depend on the intrinsic material properties as well as the microstructural geometry of the lattice, the compound effect of which presents us with a tremendous opportunity to achieve unprecedented properties that are not available in conventional monolithic materials. A unit cell based approach is often adopted to model periodic microstructures leading to a set of effective elastic moduli at macro-scale, equivalent to an idealized continuous solid material [20–25]. The fundamental mechanics for lattices being scale-independent in most cases, the research findings in this context are normally applicable for a wide range of materials and structural forms. Two dimensional lattices of hexagonal form can be found across nano to macro scale covering various natural and artificial systems in abundance (such as nanostructures of graphene, hBN etc., core of sandwich panels, microstructure of multiple woods and bones, microstructure of metamaterials, space filling pattern for 3D printing etc.) [26–32,32–35]. In fact hexagonal tessellations can be proved to be the most efficient 2D space-filling pattern. Moreover, from a geometric view-point, it can be noted that a hexagonal lattice can effectively be converted to rectangular, rhombic and re-entrant configurations as special cases. Such widespread relevance of hexagonal lattices has led to our current focus on this form of microstructure in the present article while selecting a lattice configuration to demonstrate the concepts of anisotropy tailoring.

Most of the investigations for creating mechanical metamaterials focus on the microstructural geometry for modulation of physical properties, rather than the constituent intrinsic materials. Thus, one single material, suitable for manufacturing and having adequate mechanical properties, are normally adopted as the constituent material [36]. However, recent advances in the area of multi-material additive manufacturing [37–39] have propelled the rationale for creation of a new class of metamaterial microstructures, where two or more intrinsic materials could be used to form the unit cell. Such multi-material microstructures could essentially expand the multi-functional design scope significantly, offering a higher degree of flexibility to the designer in terms of choosing (or identifying) the most suitable microstructural geometry. The Majority of investigations related to multi-functional metamaterials try an inverse identification approach to identify the intrinsic materials and their corresponding volume fractions based on numerical algorithms [40–42]. Multi-material microstructures have shown to be a pathway for achieving different unprecedented multi-physical properties like zero and negative thermal expansion along with other necessary mechanical attributes [43,44]. However, physically insightful analytical formulations of such systems leading to tailorable elastic properties are limited in the current literature. Anisotropy tailoring is an important design parameter for various mechanical systems under static and dynamic conditions, where different stiffness components are necessary along different directions. Thus it is necessary to develop the capability of achieving different degrees of anisotropy in microstructured materials with sufficient options of microstructural configurations, from which a designer can choose the most suitable one based on various other functional demands and manufacturing constraints. Here we aim to present a physics-based analytical framework for deriving the theoretical contours of microstructures to achieve different degrees of anisotropy in multi-material lattices.

It is widely known that isotropy in a mono-material hexagonal lattice can be obtained when the microstructure has an isotropic geometry. For example, regular hexagonal lattices with a unit cell comprised of six equal members and equal internal angle of 120° each, show isotropy in the elastic properties. Such limited microstructural configuration space for having isotropy restricts the scope of many multi-functional applications such as space filling in 3D printing. In this article we first aim to demonstrate that there could be multiple structural geometries in mono-material lattices that could lead to isotropy. It will be shown that the design space for isotropy can be expanded by multiple folds

when more than one intrinsic material is introduced in the unit cell of a lattice. Further we will explore the possibility of having different degrees of anisotropy in regular geometrically isotropic lattices by introducing multi-material configurations. The theoretical contours of achieving minimum anisotropy, maximum anisotropy and any fixed value of anisotropy will be systematically presented in the design space consisting of geometric and multi-material parameters. In essence, we aim to decouple the long-standing conventional understanding between relationship of effective (an)isotropy and (an)isotropic structural geometry by showing that both isotropy and anisotropy (of certain specific degree) can be achieved in a set of microstructural configurations in multi-material lattices. Though we would concentrate on hexagonal lattices in this article, the basic concepts are general and it would be applicable to other two and three dimensional lattice geometries.

2. Effective elastic moduli of multi-material lattices

In principle, multi-material lattices could have two different forms. In the first form, the unit cell could have multiple intrinsic materials and it may be tessellated to construct a lattice. In the second form the lattice may be constructed of different unit cells where two or more unit cells have different intrinsic material properties. The second form of lattice cannot be modelled using the conventional unit cell based approach as it does not lead to a periodic structure in the true sense. In the present article, our focus is on the first form of multi-material lattice where the desirable periodicity can be achieved.

Effective elastic moduli of multi-material lattices would be different from the mono-material lattice with the same structural geometry. To present adequate insights concerning the anisotropy tailoring in multi-material lattices, computational models for Young's moduli of such lattices are required. On the basis of a unit cell (consisting of three beam-like members connected at a single point, refer to Fig. 1) based approach, closed-form analytical expressions for the effective Young's moduli in two orthogonal directions are derived as a function of the intrinsic material properties and structural geometry. In the analytical derivation, only bending deformation is considered, which is most predominant for thin-walled lattices with axially rigid members. In most of the advanced mechanical systems including space filling in 3D printing, thin-walled lattices are preferred due to the fact that it leads to a lightweight design.

In this section we will focus on the two effective Young's moduli $\bar{E}_1$ and $\bar{E}_2$ since they are functions of the multi-material configuration (i.e. E_1 and E_2). It may be noted that the two in-plane Poisson's ratios are not dependent on the material properties even in case of multi-material lattices (note that the Poisson's ratio's are reported to be not dependent on the intrinsic material properties in case of mono-material lattices [20]). Expressions of the two effective Young's moduli for a multi-material lattice (refer to the supplementary material for detailed derivation) can be written as

$$\bar{E}_1 = 2E_s\,(t/l)^3\,\frac{\cos\theta}{(h/l+\sin\theta)\sin^2\theta(1+\alpha)} \tag{1}$$

$$\bar{E}_2 = E_s\,(t/l)^3\,\frac{(h/l+\sin\theta)(1+\alpha)}{2\alpha\cos^3\theta} \tag{2}$$

where, $\frac{E_1}{E_2} = \alpha$ and $E_1 = \alpha E_2 = E_s$ (E_1 and E_2 are the intrinsic Young's moduli of the two slant members, refer to Fig. 1). Here we define degree of anisotropy as $q = \frac{\bar{E}_1}{\bar{E}_2}$. Note that $\bar{E}_1$ and $\bar{E}_2$ are macro-scale properties of the lattice, while E_1 and E_2 are micro-scale properties of the intrinsic materials. It can be noticed from the above expressions that the effective in-plane elastic properties of a multi-material hexagonal lattice depend only on the intrinsic Young's modulus of the two slant members, whereas material properties of the vertical member has no contribution. This observation is similar to the case of mono-material hexagonal lattices [20]. Here t denotes thickness of the cell walls. The other geometric parameters involved in the expressions of $\bar{E}_1$ and $\bar{E}_2$ (such as h, l and θ) are indicated in Fig. 1.

For $\alpha = 1$, the expressions of elastic moduli for multi-material lattice (refer to Eqs. (1) and (2)) reduce to the traditional expressions of mono-material lattice [20] as a special case. This observation provides an exact analytical validation of the derived formulae. To validate the proposed expressions of $\bar{E}_1$ and $\bar{E}_2$ for different other values of α, we adopt a finite element based approach as discussed in section 2.3 of the supplementary material. The finite element analysis results are presented in figure 3 of the supplementary material along with the corresponding analytical results (obtained based on Eqs. (1) and (2)) for different values of α. A good agreement between the results of two forms of analysis can be noticed. It is also interesting to note the increasing level of deviation between $\bar{E}_1$ and $\bar{E}_2$ for higher values of α, essentially corroborating the preliminary evidence of the possibility of anisotropy tailoring based on multi-material parameters. The exact analytical validation for $\alpha = 1$ and finite element based numerical validation for different values of α generate necessary confidence to utilize the proposed analytical formulae of $\bar{E}_1$ and $\bar{E}_2$ for demonstrating the aspect of anisotropy tailoring further. Three different cases will be discussed systematically in the following sections leading to: I. isotropy (i.e. minimum anisotropy), II. maximum anisotropy and III. a fixed value of anisotropy. The theoretical contours in the design space of multimaterial and geometrical parameters of a unit cell will be presented considering all these three cases including insightful numerical results for demonstration. It can be noted that we have used the term 'contour' in the context of the current article to describe the microstructural configuration and their variations to achieve different degrees of (an)isotropy.

2.1. Isotropy or minimum anisotropy

In the case of $\alpha \neq 1$, an interplay among h/l, θ and α may lead to isotropy of the lattice. In literature, it is widely mentioned that $\bar{E}_1 = \bar{E}_2$ when $h/l = 1$, $\theta = 30°$, $\alpha = 1$ [20]. The value of Young's modulus would be the same, not only in any two orthogonal directions, but in all directions for an isotropic lattice. Here we show the possibility of unexplored isotropy contours of lattice materials with multi-material as well as mono-material (i.e. $\alpha = 1$) configurations. Using the condition of $\bar{E}_1 = \bar{E}_2$ based on the Eqs. (1) and (2), we get

$$\left[\frac{4\alpha}{(1+\alpha)^2}\right]\frac{\cos^4\theta}{\sin^2\theta} = (h/l+\sin\theta)^2 \tag{3}$$

From on the above equation, we investigate two possible cases depending on the value of α.

First we consider the case of α = 1, that is, the lattice is made of a single material. In such case Eq. (3) reduces to

$$\frac{\cos^4\theta}{\sin^2\theta} = (h/l+\sin\theta)^2 \tag{4}$$

One of the solutions of Eq. (4) is

$$h/l+\sin\theta = \frac{\cos^2\theta}{\sin\theta} \tag{5}$$

The above equation leads to

$$\sin\theta = \frac{1}{4}\left[-\left(\frac{h}{l}\right) \pm \sqrt{\left(\frac{h}{l}\right)^2+8}\right] \tag{6}$$

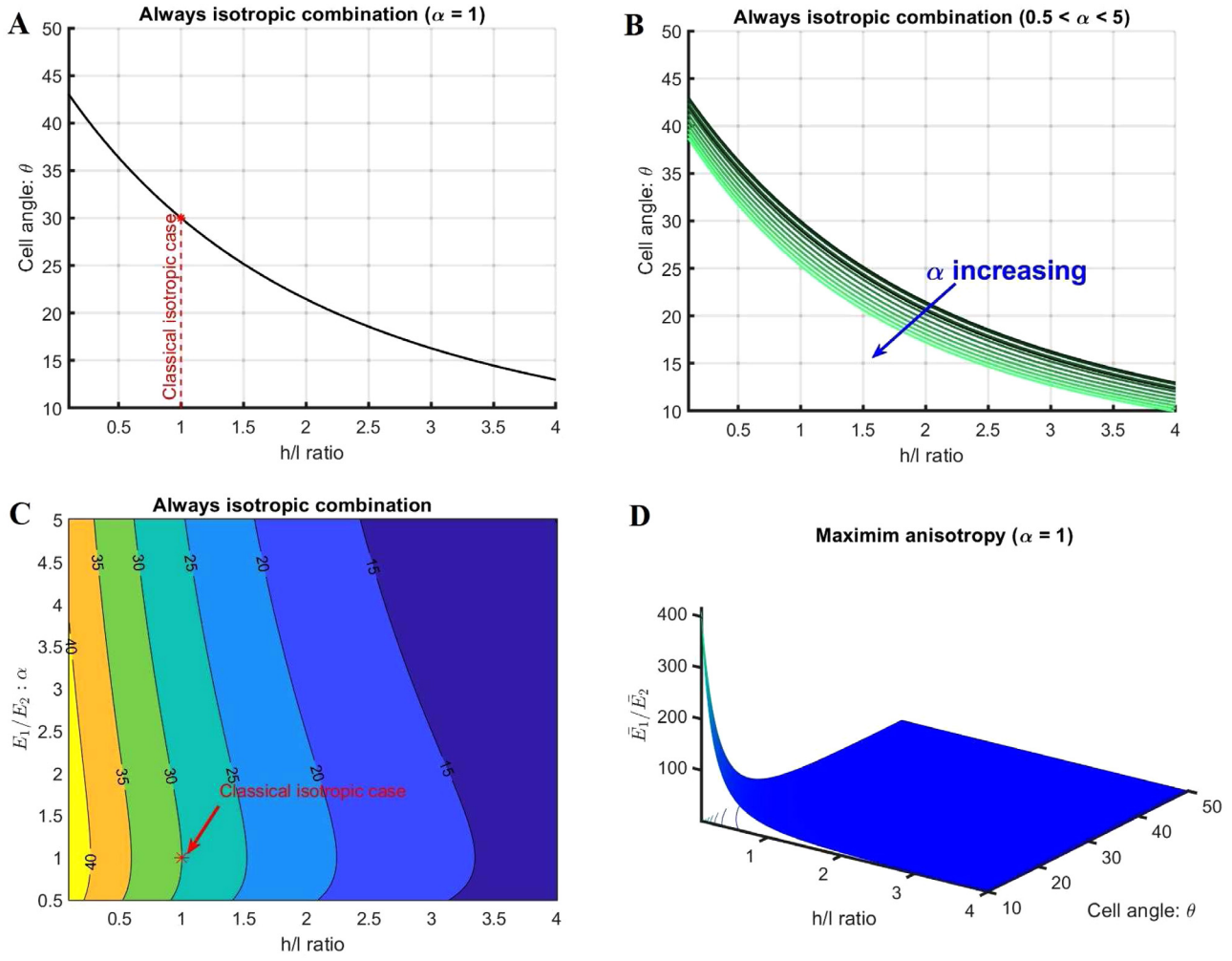

Fig. 2. Minimum and maximum anisotropy in multi-material lattices. (A) The combination of the geometric parameters, namely, the cell angle θ and $\frac{h}{l}$ resulting in effective isotropy of a mono-material lattice at macro-scale. The classical case when $h/l = 1$, $\theta = 30°$ and $\alpha = 1$ is shown by a star. **(B)** The combination of the cell angle θ and $\frac{h}{l}$ resulting in effective isotropy of multi-material lattices with $\alpha = \frac{E_1}{E_2}$ varying from 0.5 to 5. **(C)** Isotropy contour of the cell angle θ for multi-material lattices as a function of the multi-material parameter (α) and $\frac{h}{l}$. The point corresponding to the classical isotropic case when $h/l = 1$, $\theta = 30°$ and $\alpha = 1$ is shown by a star. **(D)** Maximum degree of effective anisotropy (corresponding to $\alpha = 1$) as a function of the geometric parameters θ and $\frac{h}{l}$.

Eq. (6) provides a set of solutions involving h/l and θ that will lead to isotropy in mono-material hexagonal lattices (refer to Fig. 2A). Out of this set, only one solution is widely acknowledged in the scientific literature corresponding to the case of $h/l = 1$ and $\theta = 30°$. It is important to note that the possibility of physical structural configuration of a honeycomb should always be kept in mind. For example, the two solutions of Eq. (6) corresponding to $h/l = 1$ are $\theta = 30°$ and $\theta = -90°$, among which the latter one is physically impossible.

The second solution of Eq. (4) is

$$h/l + \sin\theta = -\frac{\cos^2\theta}{\sin\theta} \tag{7}$$

The above equation leads to

$$\sin\theta = -\frac{l}{h} \tag{8}$$

Here h and l are both positive; thus θ must be negative, i.e. the solution corresponds to auxetic configurations. The possibility of physical structural configuration of a honeycomb should be kept in mind. For example, the following inequality must be satisfied for an auxetic hexagonal configuration ($\theta \leqslant 0$)

$$h \geqslant 2l\sin\theta \tag{9}$$

A closed-form solution for Young's moduli can be readily obtained corresponding to Eq. (8) as

$$\bar{E_1} = \bar{E_2} = -\frac{E_s}{\sin\theta\cos\theta}\left(\frac{t}{l}\right)^3 \tag{10}$$

Note that θ is negative in the above equation (i.e. corresponding to the auxetic configuration) and subsequently $\bar{E_1}$ and $\bar{E_2}$ are positive.

The issue of geometrically isotropic lattice requires further explanation to convey the thought of the authors with more clarity. By geometrically isotropic lattice, we refer to a particular microstructural geometry of mono-material lattices where isotropy in the Young's modulus can be achieved at macroscale. In the context of hexagonal lattice microstructures, it is a general wisdom in the field of lattice metamaterials that such isotropy in the elastic properties can be achieved when the cell angle $\theta = 30°$ and $h = l$. Thus, for a hexagonal lattice, we refer to this particular microstructural configuration as the commonly known 'geometrically isotropic' configuration. However, in the preceding paragraphs, we have shown that there are multiple other solutions for an isotropic lattice (including re-entrant microstructure) with mono-material configuration besides the conventionally reported solution corresponding to $h/l = 1$ and $\theta = 30°$. The domain of

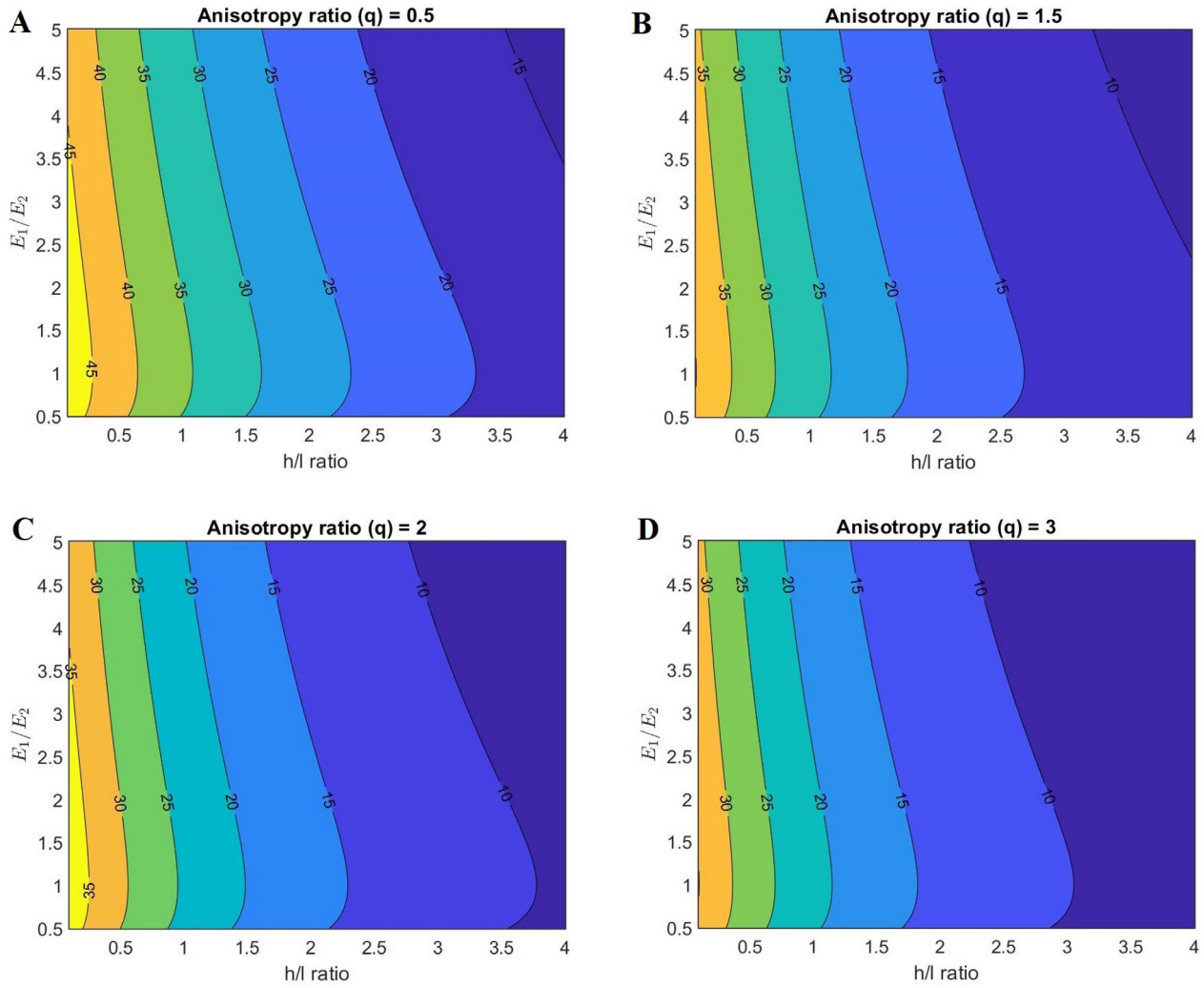

Fig. 3. Realization of fixed degree of anisotropy. **(A)** Anisotropy contour for $q = 0.5$. **(B)** Anisotropy contour for $q = 1.5$. **(C)** Anisotropy contour for $q = 2$. **(D)** Anisotropy contour for $q = 3$. Here the fixed degree of anisotropy values ($q = \frac{\bar{E}_1}{\bar{E}_2}$) are realized as a function of the intrinsic multi-material parameter $\alpha = \frac{E_1}{E_2}$ and geometric parameters θ and $\frac{h}{l}$. The contour lines in this figure show the values of the cell angle θ.

such an isotropic solution can be increased by many folds if we consider multi-material configuration. In case of multi-material lattices, we rewrite Eq. (3) as

$$\frac{4\alpha}{(1+\alpha)^2} = \frac{1}{K} \tag{11}$$

where $\frac{1}{K} = \frac{\sin^2\theta}{\cos^4\theta}\left(\frac{h}{l} + \sin\theta\right)^2$ is a function of only structural geometry. The Eq. (11) leads to the condition of isotropy in multi-material lattices as

$$\alpha = \frac{E_1}{E_2} = -1 + 2K \pm 2\sqrt{-K + K^2} \tag{12}$$

where, $K^2 - K \geqslant 0$ and the honeycomb structure should be physically achievable. The above equation provides a non-dimensional measure of the multi-material parameters (α) in terms of the microstructural geometry. Fig. 2B and 2C show the isotropy contour in a restricted domain of the multi-material and geometric parameters.

2.2. Maximum anisotropy

In this section, we aim to maximize $q = \left(\frac{\bar{E}_1}{\bar{E}_2}\right)$ and obtain the relationship among the multi-material and geometric parameters of the lattice. Based on Eqs. (1) and (2), we can write

$$q = \left(\frac{\bar{E}_1}{\bar{E}_2}\right) = \frac{\alpha}{(1+\alpha)^2} m \tag{13}$$

Here $m = \frac{4\cos^4\theta}{(h/l+\sin\theta)^2\sin^2\theta}$, which represents a purely microstructural geometric function. For maximizing the value of q, we solve the differential equation $\frac{dq}{d\alpha} = 0$ for α. The solution comes out to be $\alpha = 1$, which yields $\left(\frac{d^2q}{d\alpha^2}\Big|_{\alpha=1} < 0\right)$, indicating maxima. Thus, the condition of maximum isotropy can be obtained in the special case of mono-material lattice (i.e. $E_1 = E_2$). The corresponding value of maximum anisotropy is given by

$$\left(q^{\alpha}_{max}\big|_{\alpha=1}\right) = \frac{\cos^4\theta}{\left(\frac{h}{l} + \sin\theta\right)^2 \sin^2\theta} \tag{14}$$

From the above expression, it can be found that q is purely a function of the geometric parameters, where it increases monotonically as $\frac{h}{l}$ and θ decrease (refer to Fig. 2D).

2.3. Fixed anisotropy

In this section we try to find out the ratio $\frac{E_1}{E_2} = \alpha$ which will lead to a desired degree of anisotropy q. Thus, for the condition of $\frac{\tilde{E}_1}{\tilde{E}_2} = q$, we can write (refer to Eq. (13))

$$\frac{\alpha}{(1+\alpha)^2} = \frac{q}{m} \tag{15}$$

The above equation leads to the solution in terms of multi-material parameters as

$$\alpha = \frac{E_1}{E_2} = \frac{1}{2}\left[-\left(2-\frac{q}{m}\right) \pm \sqrt{\left(2-\frac{q}{m}\right)^2 - 4}\right] \tag{16}$$

Considering that E_1 and E_2 are both positive, in addition to the constraint of a physically achievable lattice structure, we get the following two conditions for real solutions from the above equation

$$\left[-\left(2-\frac{q}{m}\right) \pm \sqrt{\left(2-\frac{q}{m}\right)^2 - 4}\right] > 0 \tag{17}$$

$$\left(2-\frac{q}{m}\right)^2 - 4 \geqslant 0 \tag{18}$$

Fig. 3 shows the contours of θ for achieving different degrees of anisotropy (q) in terms of the geometric and multi-material parameters. It is interesting to note that the maximum value of anisotropy occurs corresponding to $\alpha = \frac{E_1}{E_2} = 1$, which is in agreement with our findings corresponding to the case of maximum isotropy as presented in the preceding section.

As explained in the introduction section, a hexagonal lattice could show negative Poisson's ratio when the cell angle θ becomes negative (refer to figure 1(C–D) of the supplementary material). This fact is evident from the closed-form expressions of Poisson's ratios (refer to equations 17 and 20 of the supplementary material) and the physical geometric constraints of a hexagonal re-entrant structure. However, from the expressions it is noted that the Poisson's ratios are not dependent on the multi-material parameters, which are the main focus of this study. The current paper primarily deals with degree of anisotropy as a function of the two Young's moduli. For this reason, we have not presented any numerical results specifically for the auxetic configurations (i.e. negative cell angle). The closed form formulae for effective Young's moduli of multi-material lattices are valid for any value of cell angle (positive, or negative), meaning that the proposed concept of anisotropy tailoring can also be directly applied to auxetic configurations. In fact, we have shown a particular family of structural configurations to achieve isotropy that is only valid for auxetic structures (refer to (8)). It can be noted in this context that the current analytical derivation and the following investigation are carried out in the linear regime of elastic analysis.

In summary, we have discussed the aspect of anisotropy tailoring in this section through the introduction of multi-material periodic systems. We start by considering a special case of hexagonal lattice, wherein the results reveal that there are multiple structural geometries in mono-material configurations that could lead to isotropy besides the conventionally considered microstructure with $h/l = 1$, $\theta = 30°$, $\alpha = 1$ for this purpose. It is shown that the design space for isotropy can be expanded by multiple folds when more than one intrinsic material is introduced in the unit cell of a lattice. We explicitly demonstrate different degrees of anisotropy in regular geometrically isotropic lattices by introducing the multi-material architecture in the design domain of geometric and material parameters. Noteworthy is that the physical models at industry-scale of such multi-material lattices are viably manufacturable following the tremendous recent advancements in additive manufacturing technology. Though we have primarily concentrated on two dimensional hexagonal lattices in this article, the concept of anisotropy tailoring using multiple intrinsic materials in the unit cell could potentially be extended to other lattice forms and three dimensional microstructures.

3. Conclusions and perspective

This article presents physics-based insights on the possibilities of having anisotropy in geometrically isotropic lattices and isotropy in geometrically anisotropic lattices. Novelty and impact of the paper lie in both conceptual development and analytical formulation. We have systematically demonstrated the aspect of tailoring anisotropy in lattice microstructures by effectively decoupling the existing knowledge on the relationship between (an)isotropy and microstructural geometry. The theoretical contours of having minimum anisotropy (i.e. isotropy), maximum anisotropy and any fixed value of anisotropy are presented in closed-form in terms of the geometric and multi-material parameters. The conventional wisdom of having limited microstructural configuration space for obtaining isotropy (or a specific degree of anisotropy) restricts the scope of many multi-functional applications such as space filling in 3D printing. Anisotropy tailoring is an important design parameter for various mechanical systems under static and dynamic conditions, where different stiffness components are necessary along different directions. Thus, it is necessary to develop the capability of achieving different degree of effective anisotropy in microstructured materials with sufficient options of microstructural configurations, from which a designer can choose the most suitable one based on various functional demands along with geometrical design and manufacturing constraints. The disseminated generic concepts of this article on anisotropy tailoring would be crucial in innovating next-generation of multi-functional materials across different length-scales without the constraint of fixed micro-structural geometry.

Declaration of competing interest

The authors declare that they have no known competing financial interests or personal relationships that could have appeared to influence the work reported in this paper.

Acknowledgements

TM acknowledges the initiation grant from IIT Kanpur. SN acknowledges the initiation grant from IIT Bombay. SA acknowledges financial support from the European Commission through Marie Sklodowska-Curie Actions, grant no: 799201. The authors would like to thank Mr. Aryan Sinha (SURGE, IIT Kanpur) for supporting the numerical validation using finite element modelling.

Appendix A. Supplementary data

Supplementary material related to this article can be found online at https://doi.org/10.1016/j.eml.2020.100934.

References

[1] A.A. Zadpoor, Mechanical meta-materials, Mater. Horiz. 3 (5) (2016) 371–381.
[2] N.A. Fleck, V.S. Deshpande, M.F. Ashby, Micro-architectured materials: Past, present and future, Proc. R. Soc. Lond. Ser. A Math. Phys. Eng. Sci. 466 (2121) (2010) 2495–2516.
[3] S.A. Cummer, J. Christensen, A. Alù, Controlling sound with acoustic metamaterials, Nat. Rev. Mater. 1 (3) (2016) 16001.
[4] Y. Lai, Y. Wu, P. Sheng, Z.-Q. Zhang, Hybrid elastic solids, Nat. Mater. 10 (8) (2011) 620.
[5] S. Khakalo, V. Balobanov, J. Niiranen, Modelling size-dependent bending, buckling and vibrations of 2D triangular lattices by strain gradient elasticity models: Applications to sandwich beams and auxetics, Internat. J. Engrg. Sci. 127 (2019) 33–52.
[6] G.W. Hunt, T.J. Dodwell, Complexity in phase transforming pin-jointed auxetic lattices, Proc. R. Soc. Lond. Ser. A Math. Phys. Eng. Sci. 475 (2019) 20180720.
[7] T. Mukhopadhyay, S. Adhikari, A. Alu, Theoretical limits for negative elastic moduli in subacoustic lattice materials, Phys. Rev. B 99 (2019) 094108.
[8] H. Wang, D. Zhao, Y. Jin, M. Wang, T. Mukhopadhyay, Z. You, Modulation of multi-directional auxeticity in hybrid origami metamaterials, Appl. Mater. Today 20 (2020) 100715.
[9] T. Mukhopadhyay, J. Ma, H. Feng, D. Hou, J.M. Gattas, Y. Chen, Z. You, Programmable stiffness and shape modulation in origami materials: Emergence of a distant actuation feature, Appl. Mater. Today 19 (2020) 100537.
[10] T. Mukhopadhyay, S. Adhikari, Stochastic mechanics of metamaterials, Compos. Struct. 162 (2017) 85–97.
[11] T. Mukhopadhyay, S. Adhikari, Effective in-plane elastic properties of auxetic honeycombs with spatial irregularity, Mech. Mater. 95 (2016) 204–222.
[12] M.A. Wadee, A.T.M. Phillips, A. Bekele, Effects of disruptive inclusions in sandwich core lattices to enhance energy absorbency and structural isolation performance, Front. Mater. 7 (2020) http://dx.doi.org/10.3389/fmats.2020.00134.
[13] S. Janbaz, K. Narooei, T. van Manen, A.A. Zadpoor, Strain rate–dependent mechanical metamaterials, Sci. Adv. 6 (25) (2020) eaba0616.
[14] A.R. Champneys, T.J. Dodwell, R.M.J. Groh, G.W. Hunt, R.M. Neville, A. Pirrera, A.H. Sakhaei, M. Schenk, M.A. Wadee, Happy catastrophe: recent progress in analysis and exploitation of elastic instability, Front. Appl. Math. Stat. 5 (2019) http://dx.doi.org/10.3389/fams.2019.00034.
[15] J. Li, C.T. Chan, Double-negative acoustic metamaterial, Phys. Rev. E 70 (2004) 055602.
[16] Z. Liu, X. Zhang, Y. Mao, Y.Y. Zhu, Z. Yang, C.T. Chan, P. Sheng, Locally resonant sonic materials, Science 289 (5485) (2000) 1734–1736.
[17] S. Adhikari, T. Mukhopadhyay, A. Shaw, N.P. Lavery, Apparent negative values of Young's moduli of lattice materials under dynamic conditions, Internat. J. Engrg. Sci. 150 (2020) 103231.
[18] Y. Wu, Y. Lai, Z.-Q. Zhang, Elastic metamaterials with simultaneously negative effective shear modulus and mass density, Phys. Rev. Lett. 107 (2011) 105506.
[19] G.W. Milton, M. Briane, J.R. Willis, On cloaking for elasticity and physical equations with a transformation invariant form, New J. Phys. 8 (10) (2006) 248.
[20] L. Gibson, M.F. Ashby, Cellular Solids Structure and Properties, Cambridge University Press, Cambridge, UK, 1999.
[21] T. Mukhopadhyay, S. Adhikari, A. Alu, Probing the frequency-dependent elastic moduli of lattice materials, Acta Mater. 165 (2019) 654–665.
[22] T. Mukhopadhyay, S. Adhikari, A. Batou, Frequency domain homogenization for the viscoelastic properties of spatially correlated quasi-periodic lattices, Int. J. Mech. Sci. 150 (2019) 784–806.
[23] C. Zschernack, M.A. Wadee, C. Vollmecke, Nonlinear buckling of fibre-reinforced unit cells of lattice materials, Compos. Struct. 136 (2016) 217–228.
[24] H. Zhang, Y. Wang, Z. Kang, Topology optimization for concurrent design of layer-wise graded lattice materials and structures, Internat. J. Engrg. Sci. 138 (2019) 26–49.
[25] M.A. Wagner, T.S. Lumpe, T. Chen, K. Shea, Programmable, active lattice structures: Unifying stretch-dominated and bending-dominated topologies, Extreme Mech. Lett. 29 (2019) 100461.
[26] T. Mukhopadhyay, S. Adhikari, Effective in-plane elastic moduli of quasi-random spatially irregular hexagonal lattices, Internat. J. Engrg. Sci. 119 (2017) 142–179.
[27] H. Ding, Z. Zhen, H. Imtiaz, W. Guo, H. Zhu, B. Liu, Why are most 2D lattices hexagonal? The stability of 2D lattices predicted by a simple mechanics model, Extreme Mech. Lett. 32 (2019) 100507.
[28] T. Mukhopadhyay, A. Mahata, S. Adhikari, M.A. Zaeem, Effective elastic properties of two dimensional multiplanar hexagonal nanostructures, 2D Mater. 4 (2) (2017) 025006.
[29] T. Mukhopadhyay, S. Adhikari, Free vibration analysis of sandwich panels with randomly irregular honeycomb core, J. Eng. Mech. 142 (11) (2016) 06016008.
[30] K.K. Gupta, T. Mukhopadhyay, A. Roy, S. Dey, Probing the compound effect of spatially varying intrinsic defects and doping on mechanical properties of hybrid graphene monolayers, J. Mater. Sci. Technol. 50 (2020) 44–58.
[31] Y. Chandra, T. Mukhopadhyay, S. Adhikari, F. Figiel, Size-dependent dynamic characteristics of graphene based multi-layer nano hetero-structures, Nanotechnology 31 (2020) 145705.
[32] A. Mahata, T. Mukhopadhyay, Probing the chirality-dependent elastic properties and crack propagation behavior of single and bilayer stanene, Phys. Chem. Chem. Phys. 20 (2018) 22768–22782.
[33] T. Mukhopadhyay, A. Mahata, S. Adhikari, M. Asle Zaeem, Probing the shear modulus of two-dimensional multiplanar nanostructures and heterostructures, Nanoscale 10 (2018) 5280–5294.
[34] T. Mukhopadhyay, A. Mahata, S. Adhikari, M. Asle Zaeem, Effective mechanical properties of multilayer nano-heterostructures, Nature Sci. Rep. 7 (15818) (2018).
[35] T. Mukhopadhyay, A. Mahata, S. Naskar, S. Adhikari, Probing the effective Young's modulus of 'magic angle' inspired multi-functional twisted nano-heterostructures, Advanced Theory and Simulations (2020) http://dx.doi.org/10.1002/adts.202000129.
[36] T. Tancogne-Dejean, D. Mohr, Elastically-isotropic elementary cubic lattices composed of tailored hollow beams, Extreme Mech. Lett. 22 (2018) 13–18.
[37] D. Chen, X. Zheng, Multi-material additive manufacturing of metamaterials with giant, tailorable negative Poisson's ratios, Sci. Rep. 8 (2018) 1–8.
[38] A. Bandyopadhyay, B. Heer, Additive manufacturing of multi-material structures, Mater. Sci. Eng. R 129 (2018) 1–16.
[39] T. Skylar, 4D printing: Multi-material shape change, Archit. Design 84 (2014) 116–121.
[40] D. Kang, S. Park, Y. Son, S. Yeon, S.H. Kim, I. Kim, Multi-lattice inner structures for high-strength and light-weight in metal selective laser melting process, Mater. Des. 175 (2019) 107786.
[41] M.J. Mirzaali, A. Caracciolo, H. Pahlavani, S. Janbaz, L. Vergani, A.A. Zadpoor, Multi-material 3D printed mechanical metamaterials: Rational design of elastic properties through spatial distribution of hard and soft phases, Appl. Phys. Lett. 113 (2018) 241903.
[42] P. Vogiatzis, S. Chen, X. Wang, T. Li, W. Lifeng, Topology optimization of multi-material negative Poisson's ratio metamaterials using a reconciled level set method, Comput. Aided Des. 83 (2017) 15–32.
[43] E. Boatti, N. Vasios, K. Bertoldi, Origami metamaterials for tunable thermal expansion, Adv. Mater. 29 (2017) 1700360.
[44] H. Xu, D. Pasini, Structurally efficient three-dimensional metamaterials with controllable thermal expansion, Sci. Rep. 6 (34924) (2016).

Computational Materials Science 177 (2020) 109507

Contents lists available at ScienceDirect

Computational Materials Science

journal homepage: www.elsevier.com/locate/commatsci

Buckling of 2D nano hetero-structures with moire patterns

Y. Chandra[a], E.I. Saavedra Flores[b,*], S. Adhikari[a]

[a] Zienkiewicz Centre for Computational Engineering, Swansea University, Swansea SA1 8EN, UK
[b] Departamento de Ingeniería en Obras Civiles, Universidad de Santiago de Chile, Av. Ecuador 3659, Estación Central, Santiago, Chile

ARTICLE INFO

Keywords:
Buckling instability
Nano hetero-structures
Graphene
Hexagonal Boron Nitride
Molybdenum disulphide
Moire angle

ABSTRACT

Moire pattern arises from the lattice mismatch between two different nanosheets. The discovery of the Moire pattern has resulted in breakthrough properties in 2D carbon-based nanostructures such as graphene. Here we investigate the impact of a Moire pattern on mechanical properties of bi-layer 2D nanosheets. In particular, buckling instability of 2D carbon-based nano hetero-structures is investigated using atomistic finite element approaches. Nano hetero-structures considered are graphene-hBN (hexagonal Boron Nitride) and graphene-MoS_2 (Molybdenum disulphide). Bilayer graphene has also been considered in the buckling analysis, by orienting the individual sheets at moire angle. Atomistic simulation methodology uses elastic beams to represent intra-sheet atomic bonds and elastic springs to represent inter-sheet atomic interactions. The influence of different boundary conditions and sheet length on the buckling of nano hetero-structures has been investigated. The bridged nano hetero-structures are found be displaying higher buckling strength as compared to cantilever sheets.

1. Introduction

Since the revolutionary discovery of graphene in 2004 [1], a progressively increasing interest by 2D nanomaterials has been observed within scientific and engineering communities. Currently, various types of 2D nanomaterials are under investigation in order to exploit their extraordinary potential as the next generation of super materials with remarkable physical properties. For instance, graphene shows great buckling strength [2,3], hexagonal Boron Nitride (hBN) [4] possesses outstanding spin-polarized states [5] and Molybdenum Disulphide (MoS_2) [6] offers exceptional electrical transport properties [7]. If different 2D nanomaterials are combined into one single nano hetero-structure, all these properties can be harnessed. Such hetero-structures are also referred to as van der Waals hetero-structures. The lattice mismatch that occurs between the lattices of nanosheets within the van der Waals hetero-structures leads to unique properties [8]. Similar lattice mismatch has also been observed in multilayer graphene sheets twisted at moire angles [9]. Such moire patterns in twisted bilayer graphene, overlaid graphene-hBN and overlaid graphene-MoS_2 are shown in Fig. 1. The relevance of moire angles between offset layers of different atoms lies in the fact that they produce changes in their electrical properties, which can result in the synthesis of new materials with potentially tailored properties. For instance, it has been found that graphene turns superconducting when two stacked graphene layers rotate by an angle of 1.1°, which represents an example of how atomically thin materials can produce completely new electrical properties [10].

Recent advances in this area, worth mentioning are the references [11–13]. Nika et al. [11] studied specific heat of twisted bilayer graphene at an angle of 21.8 °, and compared its performance against that of graphite and untwisted bilayer graphene. This article concluded that the phonon specific heat is highly dependent on a twist angle under low-temperature conditions. This means phonon engineering of thermal properties of layered materials is possible by twisting the basal atomic planes. Especially, the authors suggested that the specific heat of bilayer graphene can decrease by up to 15% when a twist angle is introduced at a temperature of 1 K. Mortazavi et al. [12] performed a mechanical analysis of a nano hetero-structure consisting of a single layer $MoTe_2$. This nanomaterial $MoTe_2$ belong to the class of transition metal dichalcogenides. These authors [12] quantified elastic modulus, Poisson's ratio, strain at the ultimate tensile strength point and the ultimate tensile strength of $MoTe_2$ under various atomic configurations, with the aid of first-principles density functional theory. These authors [12] suggested anisotropic mechanical properties, bandgap under tension, auxetic Poisson's ratio and remarkable tensile strength, for $MoTe_2$. Vargas et al. [13] studied thermal and electrical transport in a polycrystalline graphene-hBN hetero-structure, with the aid of tight-binding simulations and combined molecular dynamics-finite element simulations. This study showed a significant influence of hBN content on the thermal conductivity of the graphene-hBN hetero-structure.

* Corresponding author.
E-mail address: erick.saavedra@usach.cl (E.I. Saavedra Flores).

https://doi.org/10.1016/j.commatsci.2019.109507
Received 14 September 2019; Received in revised form 8 December 2019; Accepted 26 December 2019

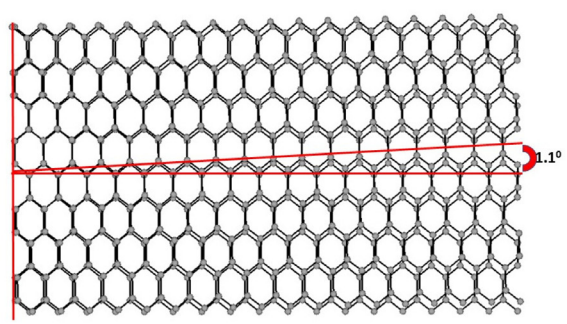

(a) Mismatch in bilayer graphene introduced by twisting at an angle of 1.1°

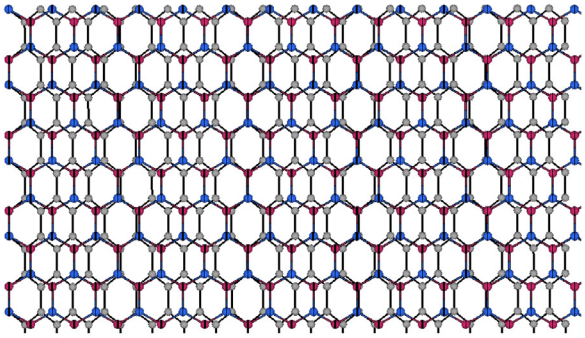

(b) Lattice mismatch in graphene-hBN bilayer sheet leading to moire pattern

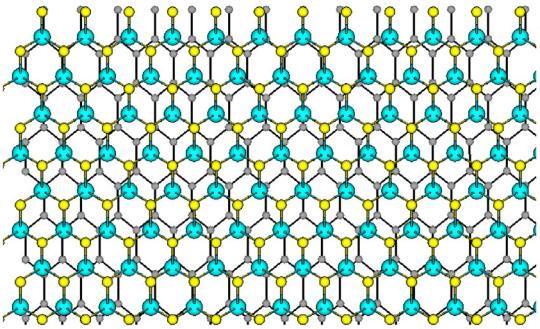

(c) Lattice mismatch in graphene-MoS_2 bilayer sheet leading to moire pattern

Fig. 1. Lattice mismatch in overlapped nanosheets leading to a moire pattern.

Furthermore, this study concluded that the graphene-hBN heterostructure could be a conductor or a semiconductor, depending on the content of hBN.

In the present work, a new contribution is made in order to provide further insight into the linear buckling of bilayer graphene sheets with sheet alignment at a moire angle of 1.1°, and graphene-hBN and graphene-MoS_2 bilayer sheets. The isometric views of graphene-graphene, graphene-hBN and graphene-MoS_2 bilayer systems are shown in Fig. 2. In this paper, we compute the critical buckling loads by means of a finite element (FE) based lattice approach. This numerical strategy establishes a linkage between the actual atomistic system and an equivalent mechanical model at the atomic bond level and provides a way to capture the atomistic response by means of conventional FE analyses and classical beam elements. Furthermore, we investigate the influence of boundary conditions and lengths of nanosheets on their buckling capacity by means of a detailed set of numerical experiments. We must note that nonlinear buckling analyses on carbon-based nanostructures have been performed in the past [3,14], however, such simulations are complex and computationally demanding and are normally justified when a post-buckling response is investigated. At present, we find it more convenient to perform linear simulations in view of our interest in the eigenvalues and eigenvectors of the nanosheet configurations studied here.

The paper is organized as follows. Section 2 presents the description of the equivalent mechanical model of nano hetero-structures by means of the finite element method (FEM). The results and discussions of the present work are given in Section 3. Finally, Section 4 summarizes our main conclusions.

2. Atomistic FE models of nano hetero-structures using FEM

The atomistic models deployed here are based on the FE methodologies developed by the authors to study graphene and its associated nanostructures [2,15–18,3]. In this research work, the FE analysis tool OPTISTRUCT has been used to model the dynamic behaviour of nano hetero-structures. The covalent bonds are represented by equivalent 3D Timoshenko FE beams and the atoms are represented by FE nodes. Within OPTISTRUCT, the element type CBEAM has been used to represent beams. The diameter and Young's modulus of the beam elements are computed by using the following equations of force constants K_r and k_θ shown below:

$$K_r = \frac{EA}{L}, \quad \text{and} \tag{1}$$

$$K_\theta = \frac{EI}{L}. \tag{2}$$

In the above equation, E is Young's modulus of the beams, I is the area moment of inertia of the beams, A is the cross-section of the beams and L is the length of the beams. The above two equations are derived from stretching and bending interatomic potentials [19,20]. The numerical values of force constants K_r and K_θ for atomic interactions such as C–C, B-N and Mo-S are available in the literature [19,20]. By substituting these values in Eq. 1 and Eq. 2, essential parameters to model covalent bond beams, such as beam diameter d and beam Young's modulus E can be calculated.

The equivalent axial force for a L-J potential between a pair of atoms i and j belonging to different nanosheets can be defined as [21]

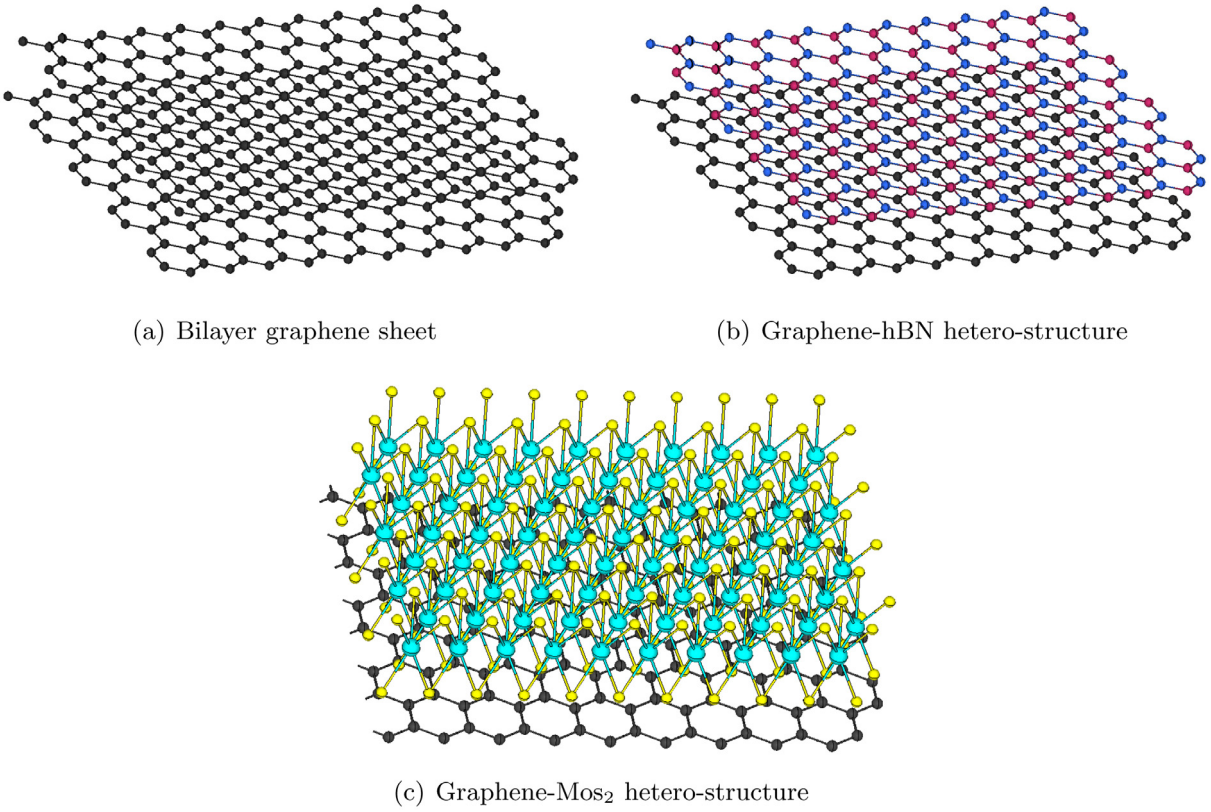

(a) Bilayer graphene sheet

(b) Graphene-hBN hetero-structure

(c) Graphene-Mos_2 hetero-structure

Fig. 2. Isometric views of bilayer graphene, graphene-hBN and graphene-MoS_2 sheets.

$$F_{ij} = \frac{\partial V_{ij}}{\partial r}, \tag{3}$$

where, r is the atomic displacement between i and j (layer-layer length). As per Girifalco et al. [22], the force between the atoms i and j can also be represented by

$$F_{ij} = -12 \in \left[\left(\frac{r_{min}}{y} \right)^{13} - \left(\frac{r_{min}}{y} \right)^{7} \right], \tag{4}$$

where, $y = r_{min} + \delta r$, δr is the atomic displacement along the length ij. The r_{min} (in Å) is given by $2^{\frac{1}{6}}\sigma$, with $\sigma = (A/B)^{1/6}$. The B and A are attractive and repulsive constants, respectively. In the current research work, three different nanosheets have been considered, namely graphene, hBN and MoS_2. Hetero-structures of graphene-hBN and graphene-MoS_2 have been studied under buckling loads. These hetero-structures lead to C-C,C-B,C-N,C-M and C-S interlayer atomic interactions, where C, B, N, M and S are carbon, boron, nitrogen, molybdenum and sulphide atoms, respectively. The values of σ and $\in$ for each individual van der Waals atomic interactions are obtained from various references [23–26]. In the atomistic FE models, we have used spring elements to form a connection between two layers of the bilayer structure representing L-J interactions. The force deflection curve for L-J springs has been calculated by using the relation in Eq. 4. Within the FE analysis tool OPTISTRUCT, the L-J springs of interlayer interactions are modelled by the element type CBUSH and by using the curves of Eq. 4 as input properties.

2.1. Validity of atomistic models

The idea of performing atomistic simulations using the finite element method has evolved since 2003 [20]. Deriving equivalent mechanical properties of atomic interactions using harmonic potentials (K_r and K_θ) is a well established concept [27,28]. Such an approach will establish near-perfect equivalence between molecular mechanics and nanostructure mechanics. Furthermore, in such simulations, the most important bond deformation modes such as bond stretching and angle variations are accurately captured. The current authors have validated the finite element approach of atomistic simulations against analytical models [15,16], experimental observations [17] and also molecular dynamic simulations [18]. The accuracy of the atomistic finite element model is found to be as high as 3.8 % in the case of nanosheets and 5 % in the case of nanocomposites. Furthermore, the results of finite element based atomistic simulation are found to close to experimental results with a very low margin difference (1.8 %). It is important to note that the prediction of buckling strength of nanostructures such as single-layer graphene, bilayer graphene, single-wall carbon nanotube, and nanocomposites, using finite element based atomistic method by current authors [2,3,14] has been widely accepted by the nanomaterials research community. The current research involves applications of same well established method [2,3,14] to explore the buckling characteristics of nano hetero-structures. The current research work can serve as a benchmark for researchers intending to introduce high fidelity into the buckling models of nano hetero-structures, in the future.

We must note that in the present FE modelling approach, an explicit expression for a potential energy function is required in order to establish an equivalence between the mechanical and atomic bond energies. Such bonds can stretch, rotate or twist between neighbouring atoms or molecules and eventually, produce a global deformation response. However, the modelling of re-formed molecular bonds due to chemical reactions is a challenging task of difficult implementation within the present computational simulation framework. Some examples of these chemical reactions can be found in pyrolysis and combustion of hydrocarbon systems where large molecules breakdown into smaller molecules in the presence of heat. For the modelling of such complex reactions, the use of reactive force-field such as ReaxFF [29] is recommended, particularly when new bonds are chemically

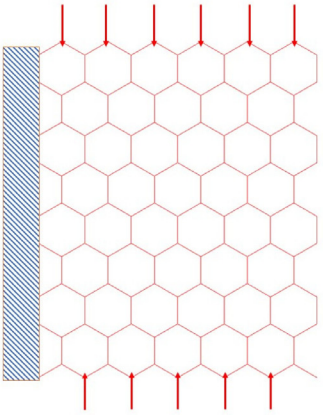

(a) Cantilever boundary condition

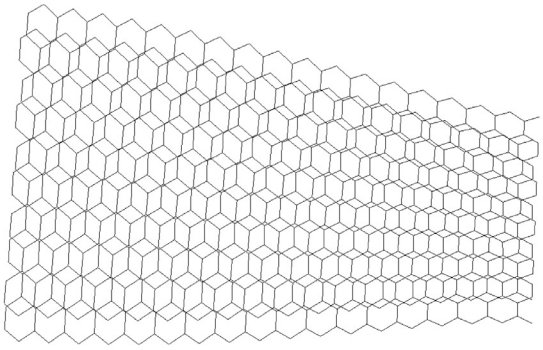

(b) First buckling mode shape of bilayer graphene

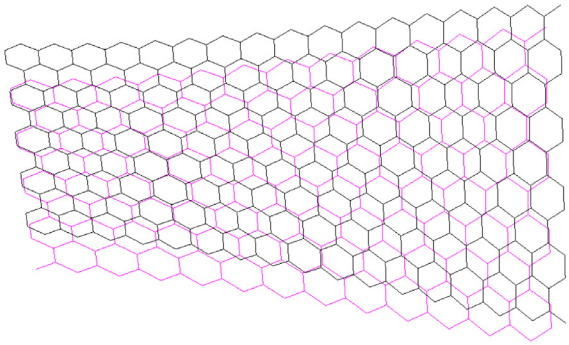

(c) First buckling mode shape of graphene-hBN hetero-structure

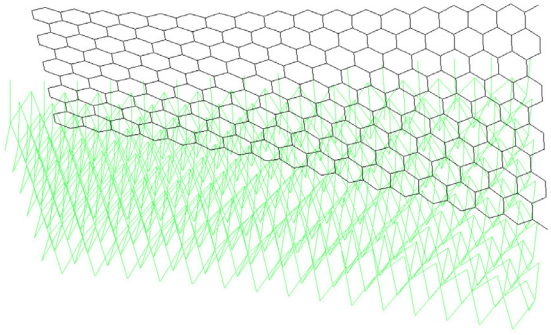

(d) First buckling mode shape of graphene-MoS_2 hetero-structure

Fig. 3. Cantilever boundary conditions and resulting buckling modes.

generated. We remark that the present FE approach is more suitable to capture the physical deformation process of atoms or molecules instead of describing the chemical reaction kinetics of atomic systems.

2.2. Stability of nanosheets

In the Moire pattern of 2-dimensional multi-layered nanosheets, it is a challenging task to keep an inter sheet angle without fixing the system. Therefore, the sheets tend to re-rotate to the original positions, when a boundary fixing is absent. However, in the current work, the sheets have been placed at an angle of 1.1° against each other, before the analysis is performed. Furthermore, in the numerical models of nanosheets, stability is ensured due to the enforcement of mechanical constraints in all six degrees of freedom, as shown in 3(a) and 4(a). It is also important to note that the relevant works [30,11,31,32] did not consider the issue of angular stability of the twisted sheets. Furthermore, Cao et al. [33] manually rotated individual sheets of bilayer graphene at an angle higher than the magic angle but did not report the issue of angular stability. Although, various types of interlayer interactions are possible between individual sheets, including van der Waals, covalent, part covalent, electrostatic(Columb), ionic and $\pi - \pi$. Only van der Waals interactions modelled by LJ-potentials are found to be effective in representing interlayer force transfer while calculating structural properties of multi-layered nanosheets [2,15,21,22].

3. Results and discussions

As the buckling capacity of nanosheets is greatly influenced by their boundary conditions, we investigate here the eigenvalues and eigenvectors of cantilevered and bridged nanosheets. The variation of the aspect ratio by changing the length is also studied. The cantilever boundary condition involves constraining all the degrees of freedom located at one edge of the sheet (Fig. 3(a)). Bridged boundary condition involves constraining all the degrees of freedom at two opposite edges (Fig. 4(a)). The two-layer nanosheet structure undergoes buckling when a unit compressive load is applied at opposite sides (Refer to Fig. 3(a) and Fig. 4(a)). Buckling analysis has been performed using the atomistic finite element approach explained in the previous section. The solution process within the FE code OPTISTRUCT involves the generation of a geometric stiffness matrix based on a unit force in the direction of buckling, followed by the numerical prediction of the eigenvalues and eigenvectors by means of a standard Lanczos solver. The buckling mode shapes for nanosheets under cantilevered boundary conditions are shown in Fig. 3(b), Fig. 3(c) and Fig. 3(d) for bilayer graphene, graphene-hBN and graphene-MoS_2, respectively. The buckling mode shapes for nanosheets under bridged boundary conditions for bilayer graphene, graphene-hBN and graphene-MoS_2 are shown in Fig. 4(b), Fig. 4(c) and Fig. 4(d), respectively. These buckling mode shapes for double layer systems are found to be identical to those of single-layer graphene (Figure not shown here).

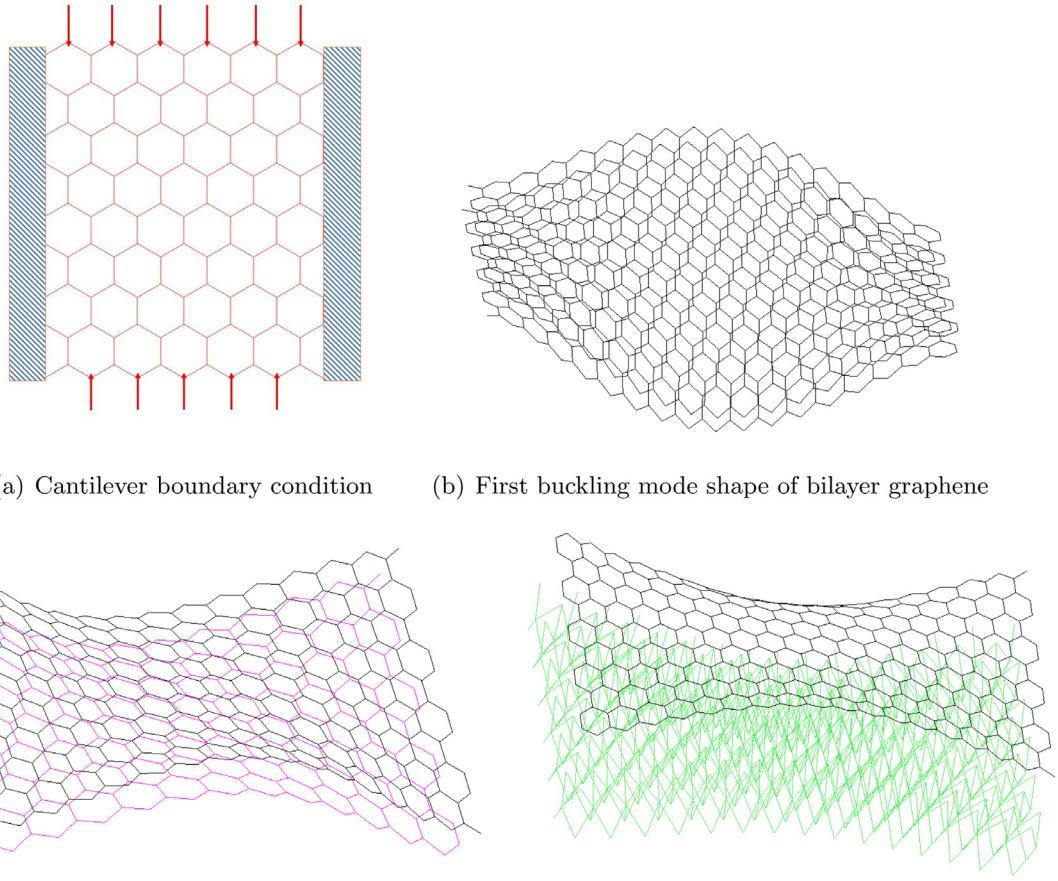

(a) Cantilever boundary condition (b) First buckling mode shape of bilayer graphene

(c) First buckling mode shape of graphene-hBN hetero-structure (d) First buckling mode shape of graphene-MoS_2 hetero-structure

Fig. 4. Bridged boundary conditions and resulting buckling modes.

3.1. Dependence of buckling loads on length

The variation of single layer critical buckling load with length is shown in Fig. 5. In order to understand the influence of the lattice mismatch on the buckling behaviour of nanosheets, Fig. 6 plots the variation of the buckling capacity in double-layered nanostructures. We can observe here that the critical buckling load decreases when the sheet length increases. Such a variation is comparable with analytical calculations reported for elastic plates [34,35]. For bridged single-layer graphene with a length increasing from 2.3 nm to 20 nm, the critical buckling load decreases from 6.2 N to 1.0 N. Within the same length range, the bridged single-layer hBN shows a decreasing critical buckling load from 4.7 N to 0.7 N. For bridged single-layer hBN, the critical buckling load decreases from 3.4 N to 0.5 N. For bridged double-layer graphene, the buckling load decreases from 179.3 N to 77.6 N. For bridged graphene-hBN, the critical load decreases from 139.1 N to

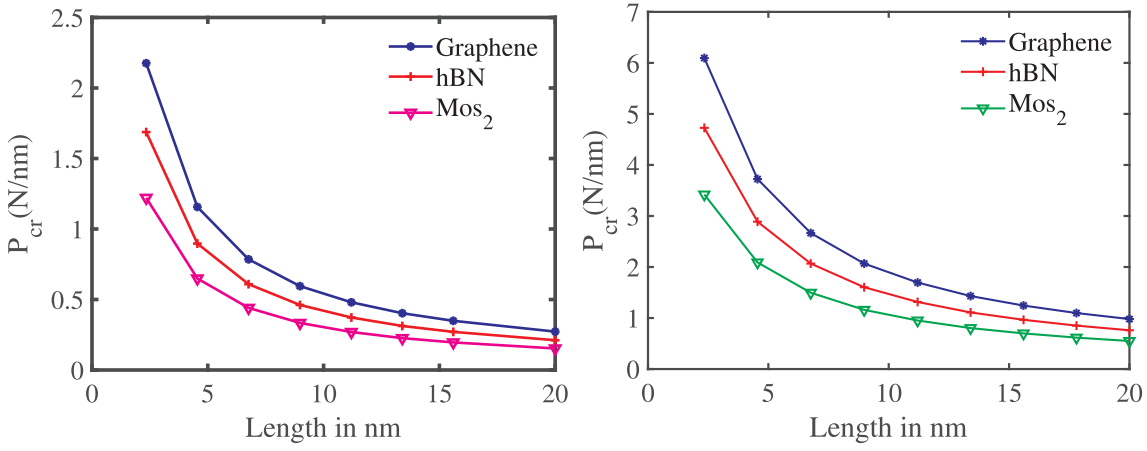

(a) Buckling loads - cantilevered single layer (b) Buckling loads - bridged single layer

Fig. 5. Variation of buckling loads with length for single layers of graphene, hBN and MoS_2.

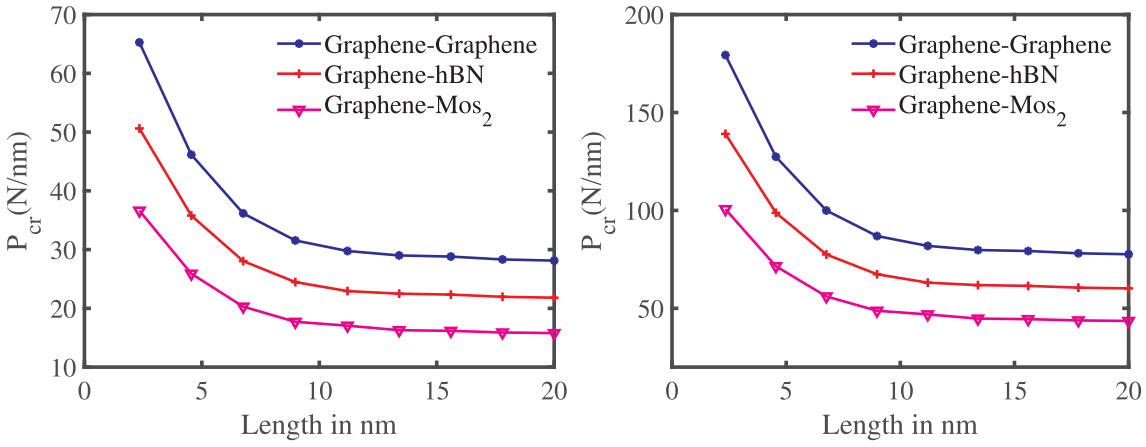

Fig. 6. Variation of buckling loads with length for double layer nanosheets of graphene-graphene, graphene-hBN and graphene-MoS_2.

Table 1
Buckling load capacities for single layer graphene, hBN and MoS_2. The single layer sheets considered here are bridged. Graphene offers higher buckling strength among the three types of nanosheets considered.

Length (nm)	$P_{Graphene}$(N)	P_{hBN}(N)	P_{MoS_2} (N)
2.3	6.2	4.7	3.4
4.5	4.1	2.9	2.1
6.7	2.9	2.1	1.5
8.9	2.2	1.61	1.2
11.2	1.9	1.3	0.9
13.4	1.6	1.1	0.8
15.6	1.4	1.0	0.7
17.8	1.2	0.8	0.6
20.0	1.1	0.7	0.5

Table 2
Comparison of bilayer graphene buckling loads against graphene-hBN and graphene-MoS_2 buckling loads. The boundary condition considered here is the bridged type. Graphene-graphene offers higher buckling strength among the three different combinations of double layers.

Length (nm)	$P_{Graphene-Graphene}$ (N)	$P_{Graphene-hBN}$ (N)	$P_{Graphene-MoS_2}$ (N)
2.3	179.3	139.1	100.6
4.5	127.4	98.8	71.5
6.7	99.9	77.5	56.1
8.9	86.9	67.4	48.8
11.2	81.8	63.1	46.9
13.4	79.7	61.9	44.8
15.6	79.3	61.5	44.5
17.8	78.1	60.6	43.8
20.0	77.6	60.2	43.6

60.2 N, and for bridged graphene-MoS_2, the buckling load decreases from 100.6 N to 43.6 N. From these observations, it can be concluded that, at a given length and under buckling loads, a double layer is stronger than the single-layer system by a factor of more than 30. Among the three combinations considered here, namely graphene-graphene, graphene-hBN and graphene-MoS_2, the homogenous graphene offers the highest buckling strength for a given length. For instance, the buckling strength of the graphene combination is found to be 79% higher than that of graphene-MoS_2, for the sheet size 2.3 nm × 9.4 nm. The quantitative data showing buckling strength at various lengths, for each single and double layer type nanosheet is shown in Table 1 and Table 2. The data listed in these two tables corresponds to the bridged boundary condition. As per Fig. 5 and Fig. 6, the variation pattern of the critical buckling loads for double layer systems is found to be dissimilar to that of single layer system. Such a dissimilarity in the pattern is due to the involvement of the interlayer L-J potential found in the double layer system.

3.2. Dependence of critical buckling load on boundary conditions

From all the plots shown in the present work, it can be observed that the bridged nanostructures offer higher buckling strength than that of cantilever nanostructures, irrespective of the number of layers. As per the continuum mechanics of elastic plates [34,35], a bridged plate structure offers higher stiffness as compared to a cantilever structure. Therefore, a bridged elastic plate or sheet will be stronger under buckling as compared to a cantilevered plate or sheet. A comparison between the bridged and cantilevered nanosheets can be found in the plots shown in Fig. 5. These plots indicate that by changing the boundary condition from cantilever to bridge type the critical buckling load increases up to about three times in the case of single-layer graphene. A similar level of enhancement is also observed for single layers of hBN and MoS_2. For double layer systems (Fig. 6), the trend is similar. For single-layer sheet models, the slope observed in the curves of cantilever and bridge sheets is found to be identical at lower lengths (< 10 nm). Whereas for double-layer sheets, the slope of the curves of cantilever sheets is found to be higher as compared to the slope of bridged sheet curves, at lower lengths (< 10 nm). Such a discrepancy is the result of the interlayer L-J potential present in the double layer system.

3.3. Enhancement in buckling capacity of graphene sheet due to the addition of another graphene, hBN or MoS_2 sheet

The variation of the ratio between the critical buckling loads of the double ($P_{Graphene-Graphene}$) and single-layer graphene ($P_{Graphene}$) is given in Fig. 7(a). The buckling load ratio between the combined graphene-hBN sheet ($P_{Graphene-hBN}$) and the single-layer graphene ($P_{Graphene}$) is given in Fig. 7(b). For the combined graphene-MoS_2 sheet ($P_{Graphene-MoS_2}$) and the single-layer graphene ($P_{Graphene}$), the critical load ratio is given in Fig. 7(c). Since the ratio remains higher than one in all the plots, it can be concluded that the addition of another layer (of any of the three nanomaterials studied here), always results in an increase in the buckling strength of the graphene sheet. As per the plots (Fig. 7) and sheet sizes considered in the current work, it is possible to observe that the addition of a nanosheet on top of the graphene sheet, leading to a lattice mismatch, results in a buckling strength increase up to 75 times. Such a great enhancement is due to the additional graphene nanosheet. If the additional sheet is of hBN or MoS_2 type, then the enhancement in buckling strength can be up to 59 times or 43 times, respectively.

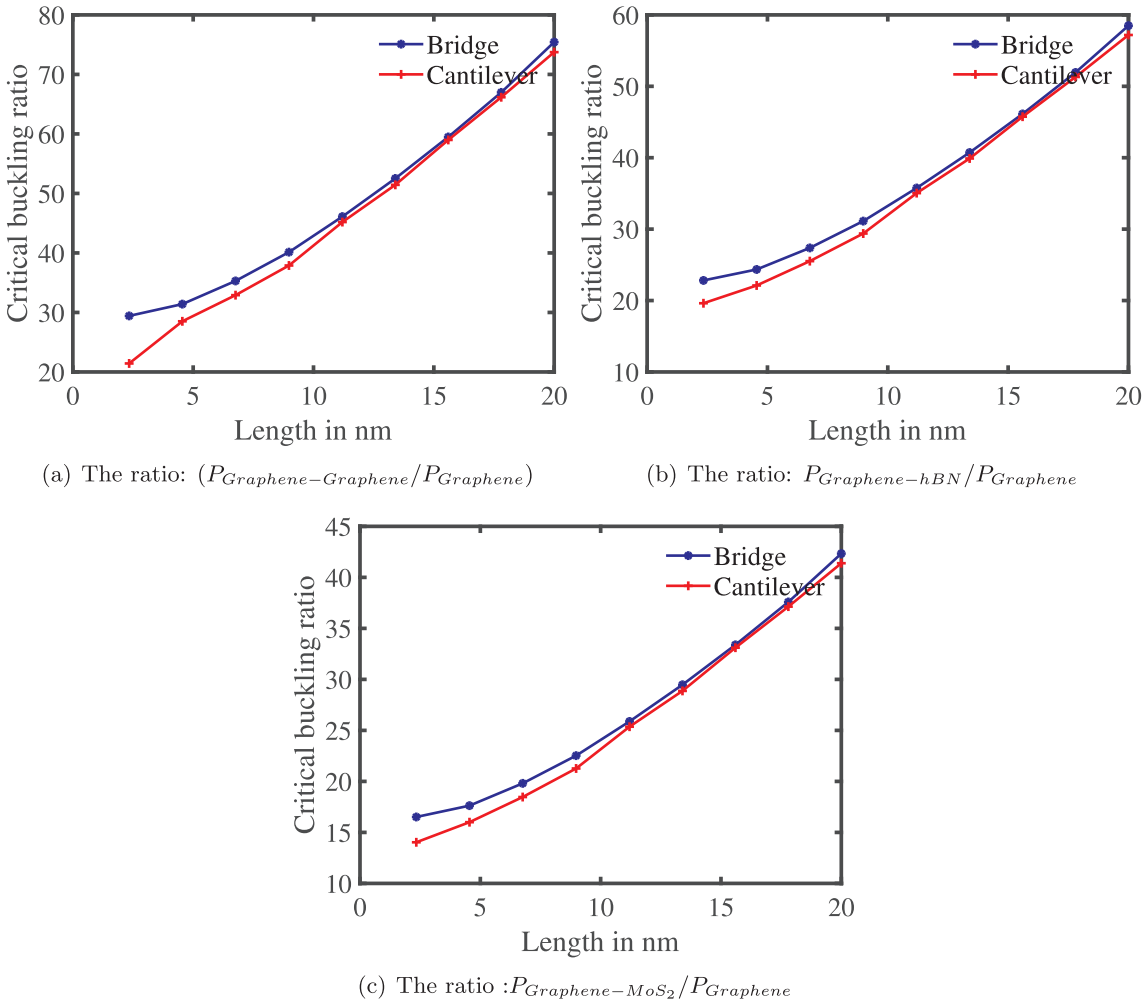

Fig. 7. Comparison between single layer graphene and double layer combinations.

The addition of another layer of a nanosheet to a graphene sheet results in higher buckling strength as compared to that of a graphene sheet alone. In order to quantify such an enhancement, buckling strength data are presented in Table 1 and Table 2. Table 1 shows values of buckling strength of single-layer of graphene, hBN and MoS_2 for various lengths, under bridged boundary conditions. As per this table, single-layer graphene offers the highest buckling strength at a given length, as compared to that of single layers of hBN and MoS_2. Among the three single-layer nanosheets considered, MoS_2 offers the least buckling strength. Table 2 shows values of buckling strength of graphene-graphene, graphene-hBN and graphene-MoS_2 double-layer nanosheets at various lengths and under bridged boundary conditions. This table proves that for a graphene sheet, the addition of another graphene sheet offers the highest buckling strength when compared to the addition of hBN or MoS_2 sheets. The inclusion of further layers leading to a three- or four-layer system, further enhances the buckling strength of the nanostructure. As compared to the bilayer graphene presented in the literature [2], the current configuration with 1.1° interlayer twist is found to be offering slightly lower (~2%) buckling capacity at a given sheet length.

Table 1 and Table 2 indicate that the variation of the single layer critical load is found to be identical with that of double layered sheets (i.e. decreasing with length). However, there is an observable difference in slopes. The slope for single layer graphene is found to be higher in regards to single layer hBN and MoS_2. The slope for double layer graphene is found to be higher in regards to graphene-hBN and graphene-MoS_2.

4. Conclusions

The buckling strength of homogeneous and heterogenous carbon-based nanostructures has been investigated by means of an atomistic finite element approach. In particular, homogeneous graphene-graphene along with heterogeneous graphene-hBN and graphene-MoS_2 nanosheets have been studied. Lattice mismatch was present in all of the double-layer configurations considered in the current study. Lattice mismatch was attained in graphene-graphene sheets by aligning the sheets at an angle of 1.1°. For the case of bilayer graphene, the introduction of such a twist angle has led to a slight decrease in buckling strength. This investigation confirmed that the bridged nanosheets offer higher buckling strength as compared to that of cantilevered nanosheets. For all of the nanosheet types studied, the critical buckling load reduced for a length increase. The addition of nanosheets such as graphene, hBN and MoS_2 on top of a single layer graphene sheet led to a significant increase in buckling strength. Among the three types of nanosheet, considered here as the addition, namely graphene, hBN and MoS_2, graphene showed the highest buckling strength. The current analysis considered lattice-mismatched double layers of nanosheets. It is estimated that the involvement of more layers can further enhance the buckling strength.

Declaration of Competing Interest

The authors declare that they have no known competing financial interests or personal relationships that could have appeared to

influence the work reported in this paper.

References

[1] K.S. Novoselov, A.K. Geim, S.V. Morozov, D. Jiang, Y. Zhang, S.V. Dubonos, I.V. Grigorieva, A.A. Firsov, Electric field effect in atomically thin carbon films, Science 306 (5696) (2004) 666–669, https://doi.org/10.1126/science.1102896 arXiv: https://science.sciencemag.org/content/306/5696/666.full.pdf , URL:https://science.sciencemag.org/content/306/5696/666.

[2] Y. Chandra, R. Chowdhury, S. Adhikari, F. Scarpa, Elastic instability of bilayer graphene using atomistic finite element, Physica E 44 (1) (2011) 12–16, https://doi.org/10.1016/j.physe.2011.06.020 URL: http://www.sciencedirect.com/science/article/pii/S1386947711002232.

[3] Y. Chandra, E.I. Saavedra Flores, F. Scarpa, S. Adhikari, Buckling of hybrid nano composites with embedded graphene and carbon nanotubes, Physica E 83 (2016) 434–441, https://doi.org/10.1016/j.physe.2016.01.021.

[4] L. Song, L. Ci, H. Lu, P.B. Sorokin, C. Jin, J. Ni, A.G. Kvashnin, D.G. Kvashnin, J. Lou, B.I. Yakobson, P.M. Ajayan, Large scale growth and characterization of atomic hexagonal boron nitride layers, Nano Lett. 10 (8) (2010) 3209–3215, https://doi.org/10.1021/nl1022139 pMID: 20698639. arXiv: https://doi.org/10.1021/nl1022139 , URL:https://doi.org/10.1021/nl1022139.

[5] V. Barone, J.E. Peralta, Magnetic boron nitride nanoribbons with tunable electronic properties, Nano Lett. 8 (8) (2008) 2210–2214, https://doi.org/10.1021/nl080745j pMID: 18624385. arXiv: https://doi.org/10.1021/nl080745j , URL:https://doi.org/10.1021/nl080745j.

[6] Z. He, W. Que, Molybdenum disulfide nanomaterials: structures, properties, synthesis and recent progress on hydrogen evolution reaction, Appl. Mater. Today 3 (2016) 23–56, https://doi.org/10.1016/j.apmt.2016.02.001 URL: http://www.sciencedirect.com/science/article/pii/S2352940716300014.

[7] S. Najmaei, M. Amani, M.L. Chin, Z. Liu, A.G. Birdwell, T.P. O'Regan, P.M. Ajayan, M. Dubey, J. Lou, Electrical transport properties of polycrystalline monolayer molybdenum disulfide, ACS Nano 8 (8) (2014) 7930–7937, https://doi.org/10.1021/nn501701a pMID: 25019978. arXiv: https://doi.org/10.1021/nn501701a.

[8] Y. Gao, Q. Liu, B. Xu, Lattice mismatch dominant yet mechanically tunable thermal conductivity in bilayer heterostructures, ACS Nano 10 (5) (2016) 5431–5439, https://doi.org/10.1021/acsnano.6b01674 pMID: 27093571. arXiv: https://doi.org/10.1021/acsnano.6b01674.

[9] S. Bertolazzi, J. Brivio, A. Kis, Stretching and breaking of ultrathin mos2, ACS Nano 5 (12) (2011) 9703–9709, https://doi.org/10.1021/nn203879f pMID: 22087740. arXiv: https://doi.org/10.1021/nn203879f.

[10] L. Wang, S. Zihlmann, M.-H. Liu, P. Makk, K. Watanabe, T. Taniguchi, A. Baumgartner, C. Schonenberger, New generation of moire superlattices in doubly aligned hbn/graphene/hbn heterostructures, Nano Lett. 19 (4) (2019) 2371–2376.

[11] D.L. Nika, A.I. Cocemasov, A.A. Balandin, Specific heat of twisted bilayer graphene: engineering phonons by atomic plane rotations, Appl. Phys. Lett. 105 (3) (2014) 031904, https://doi.org/10.1063/1.4890622 arXiv: https://doi.org/10.1063/1.4890622.

[12] B. Mortazavi, G.R. Berdiyorov, M. Makaremi, T. Rabczuk, Mechanical responses of two-dimensional mote2; pristine 2h, 1t and 1t and 1t/2h heterostructure, Extreme Mech. Lett. 20 (2018) 65–72, https://doi.org/10.1016/j.eml.2018.01.005 URL: http://www.sciencedirect.com/science/article/pii/S2352431617302213.

[13] J.E. Barrios-Vargas, B. Mortazavi, A.W. Cummings, R. Martinez-Gordillo, M. Pruneda, L. Colombo, T. Rabczuk, S. Roche, Electrical and thermal transport in coplanar polycrystalline graphene-HBN heterostructures, Nano Lett. 17 (3) (2017) 1660–1664, https://doi.org/10.1021/acs.nanolett.6b04936 pMID: 28195494. https://doi.org/10.1021/acs.nanolett.6b04936.

[14] E.I. Saavedra Flores, S. Adhikari, M. Friswell, F. Scarpa, Hyperelastic axial buckling of single wall carbon nanotubes, Physica E 44 (2) (2011) 525–529, https://doi.org/10.1016/j.physe.2011.10.006 URL: http://www.sciencedirect.com/science/article/pii/S1386947711003687.

[15] Y. Chandra, R. Chowdhury, F. Scarpa, S. Adhikari, Vibrational characteristics of bilayer graphene sheets, Thin Solid Films 519 (18) (2011) 6026–6032, https://doi.org/10.1016/j.tsf.2011.04.012 URL: http://www.sciencedirect.com/science/article/pii/S0040609011008248.

[16] Y. Chandra, R. Chowdhury, F. Scarpa, S. Adhikari, J. Sienz, C. Arnold, T. Murmu, D. Boulda, Vibration frequency of graphene based composites: a multiscale approach, Mater. Sci. Eng., B 177 (2012) 303–310, https://doi.org/10.1016/j.mseb.2011.12.024.

[17] Y. Chandra, F. Scarpa, R. Chowdhury, S. Adhikari, J. Sienz, Multiscale hybrid atomistic-fe approach for the nonlinear tensile behaviour of graphene nanocomposites, Compos. Part A 46 (2013) 147–153, https://doi.org/10.1016/j.compositesa.2012.11.006.

[18] Y. Chandra, F. Scarpa, S. Adhikari, J. Zhang, E.I. Saavedra Flores, H. Peng, Pullout strength of graphene and carbon nanotube/epoxy composites, Compos. Part B 102 (1–8) (2016), https://doi.org/10.1016/j.compositesb.2016.06.070.

[19] T. Mukhopadhyay, A. Mahata, S. Adhikari, M.A. Zaeem, 2D Mater. 4 (2) (2017) 025006, https://doi.org/10.1088/2053-1583/aa551c.

[20] C. Li, T.-W. Chou, A structural mechanics approach for the analysis of carbon nanotubes, Int. J. Solids Struct. 40 (10) (2003) 2487–2499, https://doi.org/10.1016/S0020-7683(03)00056-8 URL: http://www.sciencedirect.com/science/article/pii/S0020768303000568.

[21] F. Scarpa, S. Adhikari, R. Chowdhury, The transverse elasticity of bilayer graphene, Phys. Lett. A 374 (19) (2010) 2053–2057, https://doi.org/10.1016/j.physleta.2010.02.063 URL: http://www.sciencedirect.com/science/article/pii/S0375960110002240.

[22] L.A. Girifalco, M. Hodak, R.S. Lee, Carbon nanotubes, buckyballs, ropes, and a universal graphitic potential, Phys. Rev. B 62 (2000) 13104–13110, https://doi.org/10.1103/PhysRevB.62.13104.

[23] J.-W. Jiang, H.S. Park, Mechanical properties of mos2/graphene heterostructures, Appl. Phys. Lett. 105 (3) (2014) 033108, https://doi.org/10.1063/1.4891342.

[24] R.M. Elder, M.R. Neupane, T.L. Chantawansri, Stacking order dependent mechanical properties of graphene/mos2 bilayer and trilayer heterostructures, Appl. Phys. Lett. 107 (7) (2015) 073101, https://doi.org/10.1063/1.4928752.

[25] A.J. Pak, G.S. Hwang, Theoretical analysis of thermal transport in graphene supported on hexagonal boron nitride: the importance of strong adhesion due to π-bond polarization, Phys. Rev. Appl. 6 (2016) 034015, https://doi.org/10.1103/PhysRevApplied.6.034015.

[26] M. Neek-Amal, F.M. Peeters, Graphene on boron-nitride: Moir pattern in the van der waals energy, Appl. Phys. Lett. 104 (4) (2014) 041909, https://doi.org/10.1063/1.4863661.

[27] F. Scarpa, S. Adhikari, A mechanical equivalence for poisson's ratio and thickness of c-c bonds in single wall carbon nanotubes, J. Phys. D: Appl. Phys. 41 (8) (2008) 085306 URL: http://stacks.iop.org/0022-3727/41/i=8/a=085306.

[28] F. Scarpa, S. Adhikari, Uncertainty modeling of carbon nanotube terahertz oscillators, J. Non-Cryst. Solids 354 (35) (2008) 4151–4156, https://doi.org/10.1016/j.jnoncrysol.2008.06.065 functional and Nanostructured Materials. URL:http://www.sciencedirect.com/science/article/pii/S0022309308003840.

[29] K. Chenoweth, A.C.T. van Duin, W.A. Goddard, Reaxff reactive force field for molecular dynamics simulations of hydrocarbon oxidation, J. Phys. Chem. A 112 (5) (2008) 1040–1053.

[30] Y. Cao, V. Fatemi, S. Fang, K. Watanabe, T. Taniguchi, E. Kaxiras, P. Jarillo-Herrero, Unconventional superconductivity in magic-angle graphene superlattices, Nature 556 (7699) (2018) 43–50, https://doi.org/10.1038/nature26160.

[31] R. Bistritzer, A.H. MacDonald, Moiré bands in twisted double-layer graphene, Proc. Nat. Acad. Sci. 108 (30) (2011) 12233–12237, https://doi.org/10.1073/pnas.1108174108 arXiv: https://www.pnas.org/content/108/30/12233.full.pdf , URL:https://www.pnas.org/content/108/30/12233.

[32] S. Shallcross, S. Sharma, O.A. Pankratov, Quantum interference at the twist boundary in graphene, Phys. Rev. Lett. 101 (2008) 056803, https://doi.org/10.1103/PhysRevLett. 101.056803.

[33] Y. Cao, V. Fatemi, A. Demir, S. Fang, S.L. Tomarken, J. Luo, J.D. Sanchez-Yamagishi, K. Watanabe, T. Taniguchi, E. Kaxiras, R. Ashoori, P. Jarillo-Herrero, Correlated insulator behaviour at half-filling in magic-angle graphene superlattices, Nature 556 (2018) 80–84.

[34] S.P. Timoshenko, Theory of Plates and Shells, McGraw-Hill, New York, 1940.

[35] S.P. Timoshenko, J.M. Gere, Theory of Elastic Stability, McGraw-Hill, New York, 1961.

THEORETICAL AND APPLIED MECHANICS
Volume 47 (2020) Issue 1, 81–97 DOI: https://doi.org/10.2298/TAM200117003C

A FRACTIONAL CALCULUS APPROACH TO METADAMPING IN PHONONIC CRYSTALS AND ACOUSTIC METAMATERIALS

Milan Cajić, Danilo Karličić, Stepa Paunović, and Sondipon Adhikari

Abstract. Research on phononic and acoustic materials and structures emerged in the recent decade as a result of switching from theoretical physics to applications in various engineering fields. Periodicity is the main characteristic of the phononic medium stemming from periodic material phases, geometry or the boundary condition with wave propagation properties analysed through frequency band structure. To obtain these characteristics, the generalized Bloch theorem is usually applied to obtain the dispersion relations of viscously damped resonant metamaterials. Here we develop a novel analytical approach to analyse the fractionally damped model of phononic crystals and acoustic metamaterials introduced through the fractional-order Kelvin–Voigt and Maxwell damping models. In the numerical study, the results obtained using the proposed models are compared against the elastic cases of the phononic crystal and locally resonant acoustic metamaterial, where significant differences in dispersion curves are identified. We show that the fractional-order Maxwell model is more suitable for describing the dissipation effect throughout the spectrum due to the possibility of fitting both, the order of fractional derivative and the damping parameter.

1. Introduction

Wave propagation analysis of different materials can provide us with important information about their mechanical and dynamic properties or even existence of defects and inclusions. Waves can be of different nature, such as mechanical, electronic or electromagnetic, and they can encompass several length scales, from atomic to macro scales, such as seismic waves. The propagation of elastic waves in periodic heterogeneous materials, also known as phononic crystals, belongs to a special class of problems [1], which has received considerable attention in the scientific community in recent years [2–4]. From the physical viewpoint, periodicity in material causes destructive interference of elastic waves by forbidding them to propagate

2010 *Mathematics Subject Classification:* 34A08; 15A18.
Key words and phrases: phononic crystals, acoustic metamaterials, dissipation, fractional viscoelasticity, dispersion relations.

within the structure in certain directions and frequency ranges called band gaps [5]. In the case of locally resonant acoustic metamaterials, internal resonators play a major role in generating band gaps with associated wavelengths that are orders of magnitude longer than the periodicity of the metamaterial. This enables one to design small structures to absorb low frequency vibrations or sound. The concept of band structure, providing the relationship between frequency and the wavenumber, is well known in physics, but in mechanics it represents a dispersion relation describing the free wave propagation in some medium. Therefore, examining the band structure properties of periodic structures or metamaterials is significant from the viewpoint of their application in acoustic wave attenuation, filters for mechanical waves, noise and vibration isolation [6]. In addition, phononic crystals can be used in waveguides to open band gaps for undesired excitation modes in ultrasonic experiments [7].

The problem of wave propagation in viscoelastic materials was analysed in a number of studies [8–10]. It was demonstrated experimentally and theoretically that the presence of dissipation in PCs at lower frequencies widens the bandgaps and decreases the initial forbidden frequency [11]. Since the modulus of viscoelastic materials is frequency dependent, it is shown that the dispersion effect becomes more evident at relatively higher frequencies. Periodic materials with low-frequency bandgaps are usually made of polymers [12], which requires introduction of viscoelastic models to describe a strong damping effect in such materials. Hussein and Fraizer [13] developed the methodology to analyse general damping in phononic crystals and acoustic metamaterials by employing the generalized form of Bloch's theorem [14, 15]. One of the aims was to design an acoustic metamaterial in such a manner to achieve a high level of dissipation while keeping the high stiffness properties. The authors' main idea was to use the feature that damping is most profound at resonance frequency, which is a well known fact from linear vibration analysis in structural mechanics. They observed the frequency band structure to reveal the effect of metadamping not only near resonant frequencies but for the entire frequency-wavenumber spectrum. Chen et al. [16] applied a similar methodology to examine metadamping in a dissipative mass-in-mass lattice system with multiple resonators. In [17] the authors demonstrated that the generalized linear Maxwell model allows an accurate description of nonlinear frequency dependent elastic properties as opposed to the classic Kelvin–Voigt model, and it is widely applied to model the behaviour of many polymeric materials in a realistic manner. Recently, Alamri et al. [18] introduced a Maxwell-type damper to study wave attenuation in dissipative elastic metamaterials. Due to the band gaps merging effect induced by the Maxwell-type damper, a significant improvement of stress wave mitigation in the proposed dissipative metamaterial was demonstrated in both time and frequency domains. Application of the linear viscoelastic models and frequency domain analysis to observe the dispersion characteristics implies linearity of the system, which was justified in [17] based on the generalized Maxwell model. Moreover, in [19] the authors studied wave propagation in a two-dimensional phononic crystal with viscoelasticity based on the fractional-order Kelvin–Voigt model and

finite-difference-time-domain method. However, as discussed in [20], frequency domain analysis of the fractional-order Kelvin–Voigt model reveals unusual behaviour of increased frequency for an increase in damping in the system, which cannot be seen by the time domain analysis only. Thus, frequency domain analysis of linear fractional-order derivative viscoelastic models is also required in order to achieve reliable results for their dispersion characteristics.

Besides choosing the appropriate damping model, it is important to choose whether the frequency or the wavenumber is set to be real or complex values. Based on this, Frazier and Hussein [21] defined two classes of problems dealing with damped phononic materials. If the frequencies are assumed to be real, the damping effect is manifested in the form of complex wavenumbers defining one class of problems. This case could be physically represented by the wave propagation in a medium due to a sustained driving frequency and dissipation only in the form of spatial attenuation, which results in a linear or a quadratic eigenvalue problem. If the frequencies are permitted to be complex and wavenumbers are real, the dissipation effect is represented in the form of temporal attenuation [22]. For example, this class of problems can be physically represented by a free dissipative wave motion in a medium due to impulse loading [21]. The problem considered in this study belongs to the second class of the aforementioned problems with a specified real wavenumber and complex frequency as a solution, where the real part represents the damping factor and the imaginary part is the damped frequency. Moreover, the solution to the fractional-order differential equations sought in the frequency domain yields a characteristic polynomial with noninteger exponents, which can be solved by using the methodology from [23].

The aim of this work is to provide the framework to study the complex-eigenfrequency band structure of phononic crystals (PCs) and acoustic metamaterials (AMs) using the fractional-order general damping models. In the developed methodology, simple two-mass unit cell systems are employed for two different fractional-order viscoelastic models. The first model is the fractional Kelvin–Voigt model, and the second one is the fractional Maxwell model, both of which are the fractional-order derivative counterparts of the well known models from the linear theory of viscoelasticity with classical derivatives. Such models can exhibit a wide range of damping behaviours depending on the value of the considered retardation/relaxation times and fractional-order derivative parameters. The solution procedure for obtaining the corresponding dispersion relations is based on the temporal Fourier transform and Bloch theory. The obtained results yield new insights into the wave propagation behaviour of the aforementioned periodic structures described via fractional-order damping models.

2. Analytical models

2.1. Fractional-order dissipative models of lattice systems. A one-dimensional model of the fractionally damped diatomic *phononic crystal* (PC) can be formulated by using the lumped masses connected through elements represented by force-displacement relationships of the fractional-order Kelvin–Voigt or Maxwell

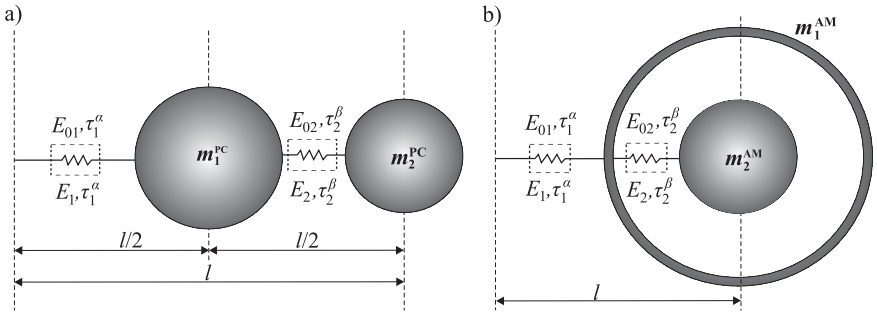

FIGURE 1. Unit cells of periodic chains consisting of masses connected with fractional-order elements a) phononic crystal b) acoustic metamaterial.

type phenomenological models (see Figure 1), which are analogous to the corresponding fractional-order stress-strain constitutive equations [20, 24]. Similar to this, fractional viscoelastic relationships can be used for the *acoustic metamaterial* (AM). Both PC and AM models are represented by a unit cell that is periodically repeated in both directions towards infinity. The equation of motion for the PC unit cell can be written as:

$$m_1\ddot{u}_1^j + f_{j,j-1}^{PC} - f_j^{PC} = 0, \tag{2.1}$$

$$m_2\ddot{u}_2^j + f_j^{PC} - f_{j,j+1}^{PC} = 0, \tag{2.2}$$

and for the AM unit cell as:

$$m_1\ddot{u}_1^j + f_{j,j-1}^{AM} - f_j^{AM} + f_{j,j+1}^{AM} = 0, \tag{2.3}$$

$$m_2\ddot{u}_2^j + f_j^{AM} = 0, \tag{2.4}$$

with u_γ^j denoting the displacement of mass m_γ, $\gamma = 1, 2$, in an arbitrary unit-cell. Forces due to viscoelastic coupling between masses and adjacent cells for the fractional Kelvin–Voigt PC and AM models are defined as:

$$f_{j,j+1}^{PC} = E_{01}[1+\tau^\alpha D^\alpha](u_1^{j+1} - u_2^j), \qquad f_j^{PC} = E_{02}[1+\tau^\beta D^\beta](u_2^j - u_1^j),$$
$$f_{j,j-1}^{PC} = E_{01}[1+\tau^\alpha D^\alpha](u_1^j - u_2^{j-1}), \qquad f_{j,j\pm1}^{AM} = \pm E_{01}[1+\tau^\alpha D^\alpha](u_1^{j\pm1} - u_1^j),$$
$$f_j^{AM} = E_{02}[1+\tau^\beta D^\beta](u_2^j - u_1^j),$$

and for the fractional Maxwell PC and AM models as:

$$f_{j,j+1}^{PC} + \tau^\alpha D^\alpha f_{j,j+1}^{PC} = E_1[1+\tau^\alpha D^\alpha](u_1^{j+1} - u_2^j),$$
$$f_j^{PC} + \tau^\beta D^\beta f_j^{PC} = E_2[1+\tau^\beta D^\beta](u_2^j - u_1^j),$$
$$f_{j,j-1}^{PC} + \tau^\alpha D^\alpha f_{j,j-1}^{PC} = E_1[1+\tau^\alpha D^\alpha](u_1^j - u_2^{j-1}),$$
$$f_{j,j\pm1}^{AM} + \tau^\alpha D^\alpha f_{j,j\pm1}^{AM} = \pm E_1[1+\tau^\alpha D^\alpha](u_1^{j\pm1} - u_1^j),$$
$$f_j^{AM} + \tau^\beta D^\beta f_j^{AM} = E_2[1+\tau^\beta D^\beta](u_2^j - u_1^j),$$

where D^α, D^β are the operators of the Riemann–Liouville derivative (see [25]), τ is the retardation/relaxation time and E_{0i} and E_i for $i = 1, 2$ are prolonged and instantaneous stiffness moduli of the fractional-order Kelvin–Voigt and Maxwell models, respectively. Bearing in mind that the Fourier transform of a fractional derivative is defined as $F[D^\alpha(u(t))] = (i\omega)^\alpha U(i\omega)$ for $i = \sqrt{-1}$, one first needs to perform the temporal Fourier transform [26] over force-displacement relationships of the fractional Kelvin–Voigt model and Eqs. (2.1)–(2.4). After taking that $p = i\omega$, one obtains the following equation for the fractional Kelvin–Voigt PC model:

$$p^2\bar{u}_1^j + \frac{E_{01}}{m_1}[1+\tau^\alpha p^\alpha](\bar{u}_1^j - \bar{u}_2^{j-1}) - \frac{E_{02}}{m_1}[1+\tau^\beta p^\beta](\bar{u}_2^j - \bar{u}_1^j) = 0, \tag{2.5}$$

$$p^2\bar{u}_2^j + \frac{E_{02}}{m_2}[1+\tau^\beta p^\beta](\bar{u}_2^j - \bar{u}_1^j) - \frac{E_{01}}{m_2}[1+\tau^\alpha p^\alpha](\bar{u}_1^{j+1} - \bar{u}_2^j) = 0, \tag{2.6}$$

and for the fractional Kelvin–Voigt AM model:

$$p^2\bar{u}_1^j + \frac{E_{01}}{m_1}[1+\tau^\alpha p^\alpha](2\bar{u}_1^j - \bar{u}_1^{j-1} - \bar{u}_1^{j+1}) + \frac{E_{02}}{m_1}[1+\tau^\beta p^\beta](\bar{u}_1^j - \bar{u}_2^j) = 0, \tag{2.7}$$

$$p^2\bar{u}_2^j + \frac{E_{02}}{m_2}[1+\tau^\beta p^\beta](\bar{u}_2^j - \bar{u}_1^j) = 0. \tag{2.8}$$

In [18], the authors introduced some additional degrees of freedom (and therefore equations) and the principle of virtual work to derive the system's equations and obtain corresponding dispersion relations of the acoustic metamaterial. In this study, there are no additional degrees of freedom since fractional force-displacement relations can be used directly in motion equations after moving to the frequency domain. After performing the temporal Fourier transform over the corresponding force-displacement relations, they are substituted into Eqs. (2.1)–(2.4) for AM and PC models. Therefore, the equation for the fractional Maxwell PC model in the frequency domain is given as:

$$p^2\bar{u}_1^j + \frac{E_1\tau^\alpha p^\alpha(\bar{u}_1^j - \bar{u}_2^{j-1})}{m_1(1+\tau^\alpha p^\alpha)} - \frac{E_2\tau^\beta p^\beta(\bar{u}_2^j - \bar{u}_1^j)}{m_1(1+\tau^\beta p^\beta)} = 0, \tag{2.9}$$

$$p^2\bar{u}_2^j + \frac{E_2\tau^\beta p^\beta(\bar{u}_2^j - \bar{u}_1^j)}{m_2(1+\tau^\beta p^\beta)} - \frac{E_1\tau^\alpha p^\alpha(\bar{u}_1^{j+1} - \bar{u}_2^j)}{m_2(1+\tau^\alpha p^\alpha)} = 0, \tag{2.10}$$

and for the fractional Maxwell AM model as:

$$p^2\bar{u}_1^j + \frac{E_1\tau^\alpha p^\alpha}{m_1(1+\tau^\alpha p^\alpha)}(2\bar{u}_1^j - \bar{u}_1^{j-1} - \bar{u}_1^{j+1}) + \frac{E_2\tau^\beta p^\beta(\bar{u}_1^j - \bar{u}_2^j)}{m_1(1+\tau^\beta p^\beta)} = 0, \tag{2.11}$$

$$p^2\bar{u}_2^j + \frac{E_2\tau^\beta p^\beta(\bar{u}_2^j - \bar{u}_1^j)}{m_2(1+\tau^\beta p^\beta)} = 0. \tag{2.12}$$

2.2. Dispersion relations using the Bloch solution. Let us assume the solution to Eqs. (2.5)–(2.12) using the Bloch's theorem [13] as:

$$\bar{u}_\gamma^{j+n} = U_\gamma e^{i(\kappa x_\gamma^j + n\kappa L)}, \quad \gamma = 1, 2, \tag{2.13}$$

with $\bar{u}_\gamma^{j+n}$ representing the displacement of mass γ in the $(j+n)$-th unit-cell of the periodic chain (here $n = -1, 0, 1$ denote the previous, present and subsequent unit cells), κ is the wavenumber, U_γ is the complex wave amplitude, L is the length of the unit-cell and $x_\gamma^j = j + L$ for the AM and $x_\gamma^j = j + \gamma L/2$ for the PC model. By substituting Eq. (2.13) in each of Eqs. (2.5)–(2.12) one obtains the system of equations in the matrix form:

$$\begin{bmatrix} S_{11}^{PC,AM} & S_{12}^{PC,AM} \\ S_{21}^{PC,AM} & S_{22}^{PC,AM} \end{bmatrix} \begin{Bmatrix} U_1^{PC,AM} \\ U_2^{PC,AM} \end{Bmatrix} = 0, \tag{2.14}$$

for both fractional Kelvin–Voigt and Maxwell models, where elements of matrices $S_{i,j}^{PC,AM}$ are given in the Appendix A. Here we prescribe the real wavenumbers $0 \leqslant \kappa L \leqslant \pi$ spanning the first irreducible Brillouin zone, which yields wavenumber-dependent complex roots. These roots can be obtained from the characteristic equation found by solving the determinant of matrix S_{ij}, which for the fractional Kelvin–Voigt PC model is given as:

$$\begin{aligned} p^4 + p^2\big[(\omega_{11}^2 + \omega_{12}^2)(1 + \tau^\alpha p^\alpha) + (\omega_{21}^2 + \omega_{22}^2)(1 + \tau^\beta p^\beta)\big] \\ + 2\omega_{11}^2\omega_{22}^2(1 - \cos\kappa L)(1 + \tau^\beta p^\beta)(1 + \tau^\alpha p^\alpha) = 0, \end{aligned} \tag{2.15}$$

and for the fractional Kelvin–Voigt AM as

$$\begin{aligned} p^4 + p^2\big[2\omega_{11}^2(1 - \cos\kappa L)(1 + \tau^\alpha p^\alpha) + (\omega_{21}^2 + \omega_{22}^2)(1 + \tau^\beta p^\beta)\big] \\ + 2\omega_{11}^2\omega_{22}^2(1 - \cos\kappa L)(1 + \tau^\beta p^\beta)(1 + \tau^\alpha p^\alpha) = 0. \end{aligned} \tag{2.16}$$

Further, for the fractional Maxwell PC model we have

$$\begin{aligned} p^4 + p^2\Big[\frac{(\tilde{\omega}_{11}^2 + \tilde{\omega}_{12}^2)\tau^\alpha p^\alpha}{(1 + \tau^\alpha p^\alpha)} + \frac{(\tilde{\omega}_{21}^2 + \tilde{\omega}_{22}^2)\tau^\beta p^\beta}{(1 + \tau^\beta p^\beta)}\Big] \\ + \frac{2\tilde{\omega}_{11}^2\tilde{\omega}_{22}^2(1 - \cos\kappa L)(\tau p)^{\alpha+\beta}}{(1 + \tau^\alpha p^\alpha)(1 + \tau^\beta p^\beta)} = 0, \end{aligned} \tag{2.17}$$

and for the fractional Maxwell AM model as

$$\begin{aligned} p^4 + p^2\Big[\frac{2\tilde{\omega}_{11}^2\tau^\alpha p^\alpha(1 - \cos\kappa L)}{(1 + \tau^\alpha p^\alpha)} + \frac{(\tilde{\omega}_{21}^2 + \tilde{\omega}_{22}^2)\tau^\beta p^\beta}{(1 + \tau^\beta p^\beta)}\Big] \\ + \frac{2\tilde{\omega}_{11}^2\tilde{\omega}_{22}^2(1 - \cos\kappa L)(\tau p)^{\alpha+\beta}}{(1 + \tau^\alpha p^\alpha)(1 + \tau^\beta p^\beta)} = 0, \end{aligned} \tag{2.18}$$

where $\omega_{11}^2 = E_{01}/m_1$, $\omega_{12}^2 = E_{01}/m_2$, $\omega_{21}^2 = E_{02}/m_1$, $\omega_{22}^2 = E_{02}/m_2$, for the fractional Kelvin–Voigt model while for the Maxwell it is given as $\tilde{\omega}_{11}^2 = E_1/m_1$, $\tilde{\omega}_{12}^2 = E_1/m_2$, $\tilde{\omega}_{21}^2 = E_2/m_1$, $\tilde{\omega}_{22}^2 = E_2/m_2$. In comparison to the work by Hussein and Frazier [13], where characteristic equations are fourth-order polynomials, one can notice that in this work the characteristic equations have noninteger exponents

due to the introduced fractional-order damping terms. The solutions cannot be obtained in the classical manner and some other techniques from the literature need to be adopted. The above characteristic equations have two pairs of complex conjugate roots that can be obtained in a manner similar to [23]. A detailed procedure of obtaining the roots of the characteristic equation is given in the Appendix B, where one first introduces the replacement $p = re^{i\psi}$ and separates the real and imaginary parts. After some algebra one can obtain corresponding transcendental equations having two zeros for some fixed value of angle ψ given in the range $\pi/2 < \psi < \pi$, while there are no stable roots in the range $0 \leqslant \psi \leqslant \pi/2$. After finding the unknown r, two pairs of complex conjugate roots of the characteristic equation can be obtained as

$$p_s = r_s e^{\pm i\psi} = \delta_s \pm \Omega_s i, \quad s = 1, 2, \tag{2.19}$$

representing the complex frequency function of the presented fraction-order system, thus permitting the wave attenuation in time. In the above equation, the imaginary part of the complex conjugate roots Ω_s represents the damped frequency and the real part δ_s is the damping factor. Therefore, the imaginary part of the complex root obtained in terms of the wavenumber represents the dispersion relation of the observed PC or AM structure with fractional-order damping. The limiting case with no damping, where the frequency of the fractionally damped system is approaching the one corresponding to the equivalent elastic system, occurs for the values $\psi \to \pi/2$. One should state that fractional derivative viscoelastic models undergo certain limitations in the values of fractional-order parameters coming from the second law of thermodynamics. However, these limitations do not apply to the fractional Maxwell and Kelvin–Voigt models since they belong to groups of diffusion-wave and diffusion type rheological models, respectively.

3. Numerical results

In the numerical study, we perform the parametric study and compare the results obtained by the herein presented fractional viscoelastic models of phononic crystal and acoustic metamaterial against those for the elastic case. For this reason, in the following numerical experiment we adopted the values of ratios of elastic coefficients and masses the same as in the paper by Hussein et al. [13] i.e. we adopted the ratios of prolonged elasticity coefficients given in the fractional derivative model and masses as $\omega_{11}^2 = (250000)^{1/2}$, $\omega_{12}^2 = E_{01}/m_2 = (50000)^{1/2}$, $\omega_{21}^2 = (50000)^{1/2}$, $\omega_{22}^2 = 100$, and similar for the Maxwell model as $\tilde{\omega}_{11}^2 = (250000)^{1/2}$, $\tilde{\omega}_{12}^2 = (50000)^{1/2}$, $\tilde{\omega}_{21}^2 = (50000)^{1/2}$, $\tilde{\omega}_{22}^2 = 100$, with the length of unit cells $L = 1$. We should note that the parameters in this work can be read in any consistent system of physical units. For the numerical study we adopted the values of fractional parameters in the range $0 < \alpha, \beta < 1$ while instead of choosing the retardation/relaxation times we used fixed values of angle $\psi > \pi/2$ (since no stable roots are available for $\psi < \pi/2$), which, after solving the transcendent equation numerically, yields two roots X_1 and X_2. Introducing these two roots into the equations for r and Eq. (2.19) gives two pairs of complex conjugate poles of

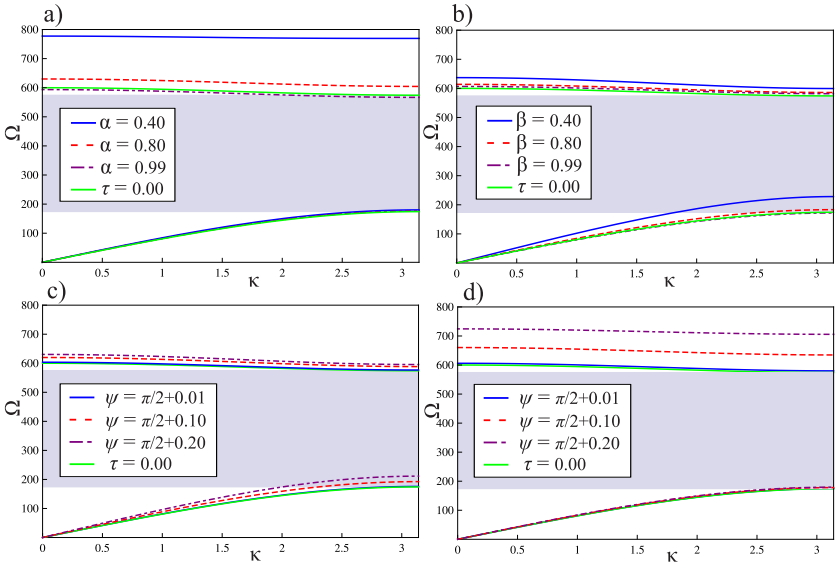

FIGURE 2. Dispersion curves of the elastic system (green lines) with the corresponding gap (gray colored square) and fractional-order viscoelastic Kelvin–Voigt phononic crystal for varying model parameters and fixed values of a) $\psi = \pi/2 + 0.2$ and $\beta = 0.9$, b)$\psi = \pi/2 + 0.2$ and $\alpha = 0.9$, c) $\alpha = 0.9$ and $\beta = 0.5$,d) $\alpha = 0.5$ and $\beta = 0.9$

the system as roots of the characteristic equation i.e. damped frequency Ω_s and damping factor δ_s.

Figure 2 shows the dispersion curves of the fractional PC Kelvin–Voigt model for different values of fractional-order derivative parameters, and damping parameters corresponding to angle ψ. In all figures one can notice two sets of dispersion curves where the upper ones belong to optical and the lower ones to acoustic branches. One can notice an obvious frequency shift due to the change of damping parameter and orders of fractional derivatives, which is more obvious in the optical branch. The dispersion curves of the equivalent elastic phononic structure are represented by the green lines while the corresponding band gaps are marked by squares coloured in grey. One can notice significantly higher frequencies in the optical branches for lower values of the fractional derivative order. This effect is more pronounced for changes of fractional parameter α. This is also noticed for the changes of the damping parameter (by changes of angle ψ), which yields higher frequencies and band gaps for an increase in damping and fixed values of fractional-order derivatives. Therefore, elastic waves cannot propagate through the system within the obtained frequency band gap region. The results for the fractional-order Kelvin–Voigt model lack physical interpretation since frequency increases with an increase in the damping parameter at lower values of the fractional derivative order.

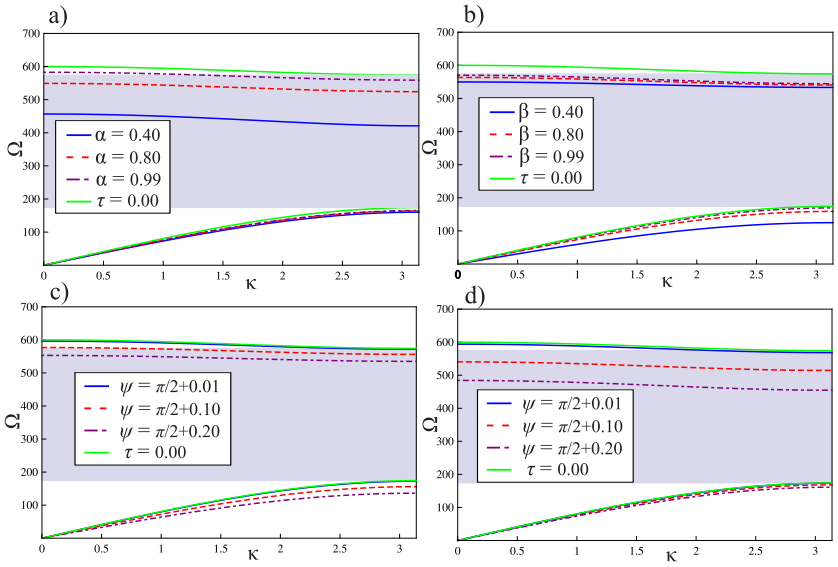

FIGURE 3. Dispersion curves of the elastic system (green lines) with the corresponding band gap (gray colored square) and fractional-order viscoelastic Maxwell phononic crystal for varying model parameters and fixed values of a) $\psi = \pi/2{+}0.2$ and $\beta = 0.9$, b)$\psi = \pi/2 + 0.2$ and $\alpha = 0.9$, c) $\alpha = 0.9$ and $\beta = 0.5$,d) $\alpha = 0.5$ and $\beta = 0.9$

This feature of the fractional Kelvin–Voigt model is attributed to its diffusion type nature and instability and sensitivity to small variations in the damping parameter as discussed in [20].

Figure 3 shows the dispersion curves for the phononic crystal fractional Maxwell model. One can observe lower values of frequency, especially in the optical branch, and narrower band gaps for lower values of the fractional-order parameter compared to the elastic case (green line). This effect is more pronounced for the changes of fractional parameter α while a decrease in β is more visible in the acoustic branch together with the overall shift of the band gap. However, as expected for dissipation models, in the increase of damping parameter (through an increase in the angle ψ) causes a decrease in frequency. This effect is more pronounced for the case when $\alpha < \beta$.

In the following, the dispersion curves for the acoustic metamaterials with the fractional Kelvin–Voigt and Maxwell damping models are given in Figures 4 and 5, respectively. In Figure 4 one can observe much different dispersion curves of acoustic metamaterials compared to the phononic crystals in both acoustic and optical branches. The obtained band gaps are at lower frequencies and narrower than for the phononic crystals. However, for lower values of fractional parameter β one can notice an increase in frequency and band gap widening. Similar behaviour

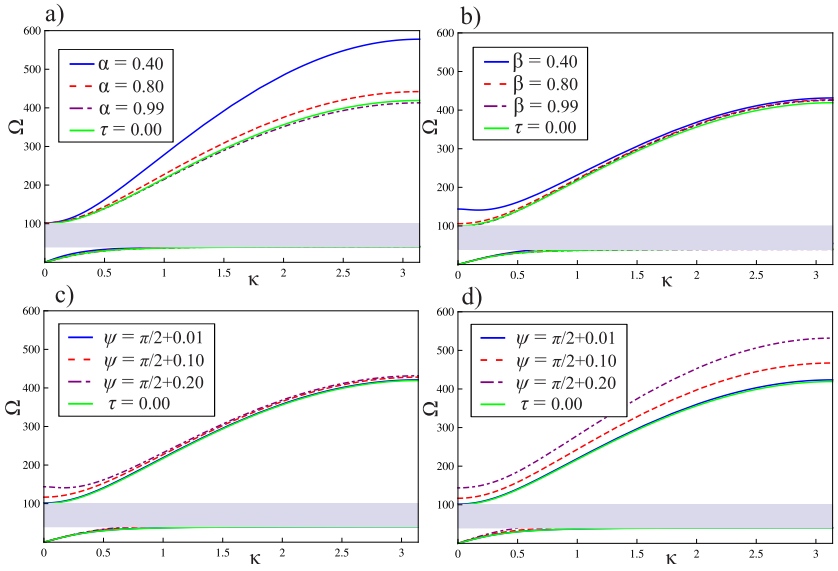

FIGURE 4. Dispersion curves of the elastic system (green lines) with the corresponding band gap (gray colored square) and fractional-order viscoelastic Kelvin–Voigt acoustic metamaterial for varying model parameters and fixed values of a) $\psi = \pi/2 + 0.2$ and $\beta = 0.9$, b)$\psi = \pi/2 + 0.2$ and $\alpha = 0.9$, c) $\alpha = 0.9$ and $\beta = 0.5$,d) $\alpha = 0.5$ and $\beta = 0.9$

can be noticed for an increase in the damping parameter in Figure 4 c) and d). However, this behaviour lacks physical interpretation since in this case we use the diffusion type fractional Kelvin–Voigt model as mentioned before. In addition, Figure 5 shows the dispersion curves for the acoustic metamaterial fractional Maxwell model. It can be noticed that the band gap is narrower at lower values of fractional parameter β. However, changes of dispersion curves are more pronounced in the optical branch where frequency decreases with an increase in the damping parameter (angle ψ). One can observe that the main dissipation effect occurs outside the band gap, where frequency in the optical branch is significantly damped compared to the elastic case. Consequently, dissipation models show that damping can affect the band gap width but the main dissipation is outside this region. Potential application of acoustic metamaterials is in the blast wave mitigation and wave isolation. This was demonstrated in [18] based on the classical Maxwell damping model of acoustic metamaterial, where broadband acoustic wave attenuation was achieved based on the system with several resonators. Since the relationship between the damping ratio, frequency and damping factor cannot be established in the classical sense, we have omitted the analyses of real parts (damping factors) of complex roots for the fractional viscoelastic models. An advantage of fractional viscoelastic models lies in the fact that they have been proven in the literature as

superior to the conventional models in fitting the damping behaviour of variety of materials. However, for wave attenuation in a broader frequency spectrum it would be necessary to introduce more resonators or hierarchical design [28] of the metamaterial structure.

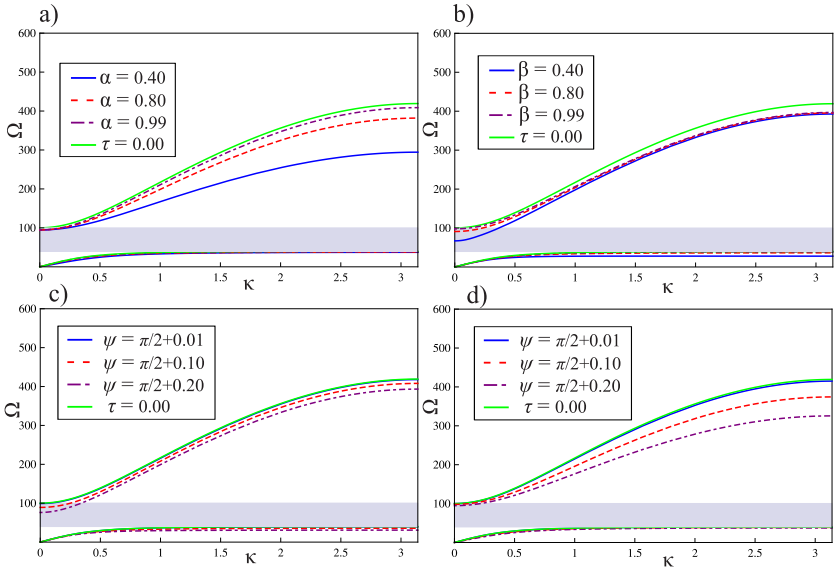

FIGURE 5. Dispersion curves of the elastic system (green lines) with the corresponding band gap (gray colored square) and fractional-order viscoelastic Maxwell acoustic metamaterial for varying model parameters and fixed values of a) $\psi = \pi/2 + 0.2$ and $\beta = 0.9$, b)$\psi = \pi/2 + 0.2$ and $\alpha = 0.9$, c) $\alpha = 0.9$ and $\beta = 0.5$,d) $\alpha = 0.5$ and $\beta = 0.9$

4. Conclusions

In this communication, we studied general fractional-order derivative models of a two-mass phononic crystal and acoustic metamaterial. The fractional Kelvin–Voigt and Maxwell viscoelasticity models are introduced through corresponding force-displacement relationships to account for the dissipation effects due to temporal attenuation of waves. It was demonstrated that the proposed models exhibit different dissipation behaviour from the conventional viscoelastic and elastic models. In the case of the fractional Kelvin–Voigt model, anomalous behaviour of increased frequency for an increase in the damping parameter was revealed in the dispersion curves at lower values of fractional parameters. However, the fractional Maxwell model exhibited larger dissipation for AMs and band gap narrowing for PCs in the entire spectrum. In conclusion, we can state that the fractional-order dissipation models of PCs and AMs can simulate a wide range of behaviours and dissipation in the entire frequency-wavenumber spectrum, which can fit some of the

possible behaviours of real-world phononic structures and acoustic metamaterials. The presented methodology can be extended to study metamaterials with a more complex unit cell hierarchy.

Appendix A. Matrix elements

Elements of matrix S_{ij}^{PC} for the fractional Kelvin–Voigt PC model are given as

$$S_{11}^{PC} = p^2 + \frac{E_{01}}{m_1}(1+\tau^\alpha p^\alpha) + \frac{E_{02}}{m_1}(1+\tau^\beta p^\beta),$$

$$S_{12}^{PC} = -\frac{E_{01}}{m_1}(1+\tau^\alpha p^\alpha)e^{-i\kappa L} - \frac{E_{02}}{m_1}(1+\tau^\beta p^\beta),$$

$$S_{21}^{PC} = -\frac{E_{01}}{m_2}(1+\tau^\alpha p^\alpha)e^{i\kappa L} - \frac{E_{02}}{m_2}(1+\tau^\beta p^\beta),$$

$$S_{22}^{PC} = p^2 + \frac{E_{01}}{m_2}(1+\tau^\alpha p^\alpha) + \frac{E_{02}}{m_2}(1+\tau^\beta p^\beta).$$

Elements of matrix S_{ij}^{PC} for the fractional Kelvin-Voigt PC model are given as

$$S_{11}^{PC} = p^2 + \frac{E_{01}}{m_1}(1+\tau^\alpha p^\alpha) + \frac{E_{02}}{m_1}(1+\tau^\beta p^\beta),$$

$$S_{12}^{PC} = -\frac{E_{01}}{m_1}(1+\tau^\alpha p^\alpha)e^{-i\kappa L} - \frac{E_{02}}{m_1}(1+\tau^\beta p^\beta),$$

$$S_{21}^{PC} = -\frac{E_{01}}{m_2}(1+\tau^\alpha p^\alpha)e^{i\kappa L} - \frac{E_{02}}{m_2}(1+\tau^\beta p^\beta),$$

$$S_{22}^{PC} = p^2 + \frac{E_{01}}{m_2}(1+\tau^\alpha p^\alpha) + \frac{E_{02}}{m_2}(1+\tau^\beta p^\beta).$$

Similarly, by substituting the Eq. (2.13) in each of the Eqs. (2.7)–(2.12) one can obtain elements of matrix S_{ij}^{PC} for the Maxwell model and elements of matrices S_{ij}^{AM} for both, fractional-order Kelvin–Voigt and Maxwell models.

Appendix B. Roots of the characteristic equations

Here, the procedure for obtaining the roots of polynomials with noninteger exponents in an analytical manner is presented. After using the following replacement $p = re^{i\psi}$ in Eqs. (2.5)–(2.8) and separating the real and imaginary parts, one obtains the following relations for the fractional Kelvin–Voigt PC model:

$$\begin{aligned}(\text{B.1})\quad & r^4\cos 4\psi + (\omega_{11}^2+\omega_{12}^2)r^2R_\alpha\cos(2\psi+\phi_\alpha) + (\omega_{21}^2+\omega_{22}^2)r^2R_\beta\cos(2\psi+\phi_\beta)\\ &+ 2\omega_{11}^2\omega_{22}^2(1-\cos\kappa L)R_\alpha R_\beta\cos(\phi_\alpha+\phi_\beta) = 0\end{aligned}$$

$$\begin{aligned}(\text{B.2})\quad & r^4\sin 4\psi + (\omega_{11}^2+\omega_{12}^2)r^2R_\alpha\sin(2\psi+\phi_\alpha) + (\omega_{21}^2+\omega_{22}^2)r^2R_\beta\sin(2\psi+\phi_\beta)\\ &+ 2\omega_{11}^2\omega_{22}^2(1-\cos\kappa L)R_\alpha R_\beta\sin(\phi_\alpha+\phi_\beta) = 0,\end{aligned}$$

and for the fractional Kelvin–Voigt AM model as:

$$\begin{aligned}(\text{B.3})\quad & r^4\cos 4\psi + 2\omega_{11}^2 r^2 R_\alpha(1-\cos\kappa L)\cos(2\psi+\phi_\alpha)\\ &+(\omega_{21}^2+\omega_{22}^2)r^2R_\beta\cos(2\psi+\phi_\beta)\\ &+2\omega_{11}^2\omega_{22}^2(1-\cos\kappa L)R_\alpha R_\beta\cos(\phi_\alpha+\phi_\beta)=0,\end{aligned}$$

$$\begin{aligned}(\text{B.4})\quad & r^4\sin 4\psi + 2\omega_{11}^2 r^2 R_\alpha(1-\cos\kappa L)\sin(2\psi+\phi_\alpha)\\ &+(\omega_{21}^2+\omega_{22}^2)r^2R_\beta\sin(2\psi+\phi_\beta)\\ &+2\omega_{11}^2\omega_{22}^2(1-\cos\kappa L)R_\alpha R_\beta\sin(\phi_\alpha+\phi_\beta)=0,\end{aligned}$$

where R_α, R_β, ϕ_α and ϕ_β are polar coordinates for bracket terms in (2.5)–(2.8) given as:

$$R_\alpha=\sqrt{1+X^\alpha+X^{2\alpha}},\quad R_\beta=\sqrt{1+X^\beta+X^{2\beta}},$$

$$\tan\phi_\alpha=\frac{X^\alpha\sin\alpha\psi}{1+X^\alpha\cos\alpha\psi},\quad \tan\phi_\beta=\frac{X^\beta\sin\beta\psi}{1+X^\beta\cos\beta\psi},$$

where the replacement $X=r\tau$ is used. First, one should multiply Eqs. (B.1) and (B.2) with $\sin 4\psi$ and $\cos 4\psi$, respectively, and subtracting one from another eliminate the term r^4. The same equations should be multiplied again with $\sin\phi_\alpha+\phi_\beta$ and $\cos\phi_\alpha+\phi_\beta$ and then subtracted one from another to eliminate the last terms in equations. After taking into account some trigonometric identities, for the fractional Kelvin–Voigt PC model one can obtain two equations in terms of r^2 as:

$$r^2=-\frac{2\omega_{11}^2\omega_{22}^2(1-\cos\kappa L)R_\alpha R_\beta\sin(\gamma_\alpha+\gamma_\beta)}{(\omega_{11}^2+\omega_{12}^2)R_\alpha\sin\gamma_\alpha+(\omega_{21}^2+\omega_{22}^2)R_\beta\sin\gamma_\beta},$$

$$r^2=-\frac{(\omega_{11}^2+\omega_{12}^2)R_\alpha\sin\gamma_\beta+(\omega_{21}^2+\omega_{22}^2)R_\beta\sin\gamma_\alpha}{\sin(\gamma_\alpha+\gamma_\beta)},$$

where $\gamma_\alpha=\phi_\alpha-2\psi$ and $\gamma_\beta=\phi_\beta-2\psi$. Using the same procedure over Eqs. (B.3) and (B.4) the following equations in terms of r^2 can be obtained for the fractional Kelvin–Voigt AM model:

$$r^2=-\frac{2\omega_{11}^2\omega_{22}^2(1-\cos\kappa L)R_\alpha R_\beta\sin(\gamma_\alpha+\gamma_\beta)}{2\omega_{11}^2R_\alpha(1-\cos\kappa L)\sin\gamma_\alpha+(\omega_{21}^2+\omega_{22}^2)R_\beta\sin\gamma_\beta},$$

$$r^2=-\frac{2\omega_{11}^2R_\alpha(1-\cos\kappa L)\sin\gamma_\beta+(\omega_{21}^2+\omega_{22}^2)R_\beta\sin\gamma_\alpha}{\sin(\gamma_\alpha+\gamma_\beta)}.$$

By equating the equations for r^2 obtained for the fractional Kelvin–Voigt PC or AM models one can obtain the corresponding transcendent equation with two zeros defining the unknown X for the fixed values of angle ψ, which are denoted as X_s, $s=1,2$. Further, by substituting X_s in any of the equations for r and then in Eq. (2.19), one can find four roots of the characteristic polynomial with fractional exponents.

After using the same replacement $p=re^{i\psi}$ in Eqs. (2.9)–(2.12) and separating real and imaginary parts, for the Maxwell PC model one obtains:

$$r^4\cos 4\psi+(\omega_{11}^2+\omega_{12}^2)r^2R_\alpha^{-1}X^\alpha\cos(2\psi-\phi_\alpha+\alpha\psi)+2\omega_{11}^2\omega_{22}^2R_\alpha^{-1}R_\beta^{-1}X^{\alpha+\beta}(1-\cos\kappa L)\cos(\psi\alpha+\psi\beta-\phi_\alpha-\phi_\beta)+(\omega_{21}^2+\omega_{22}^2)r^2R_\beta^{-1}X^\beta\cos(2\psi-\phi_\beta+\beta\psi)=0, \tag{B.5}$$

$$r^4\sin 4\psi+(\omega_{11}^2+\omega_{12}^2)r^2R_\alpha^{-1}X^\alpha\sin(2\psi-\phi_\alpha+\alpha\psi)+2\omega_{11}^2\omega_{22}^2R_\alpha^{-1}R_\beta^{-1}X^{\alpha+\beta}(1-\cos\kappa L)\sin(\psi\alpha+\psi\beta-\phi_\alpha-\phi_\beta)+(\omega_{21}^2+\omega_{22}^2)r^2R_\beta^{-1}X^\beta\sin(2\psi-\phi_\beta+\beta\psi)=0, \tag{B.6}$$

and for the Maxwell AM model as:

$$r^4\cos 4\psi+2\omega_{11}^2r^2R_\alpha^{-1}X^\alpha(1-\cos\kappa L)\cos(2\psi-\phi_\alpha+\alpha\psi)+2\omega_{11}^2\omega_{22}^2R_\alpha^{-1}R_\beta^{-1}X^{\alpha+\beta}(1-\cos\kappa L)\cos(\psi\alpha+\psi\beta-\phi_\alpha-\phi_\beta)+(\omega_{21}^2+\omega_{22}^2)r^2R_\beta^{-1}X^\beta\cos(2\psi-\phi_\beta+\beta\psi)=0, \tag{B.7}$$

$$r^4\sin 4\psi+2\omega_{11}^2r^2R_\alpha^{-1}X^\alpha(1-\cos\kappa L)\sin(2\psi-\phi_\alpha+\alpha\psi)+2\omega_{11}^2\omega_{22}^2R_\alpha^{-1}R_\beta^{-1}X^{\alpha+\beta}(1-\cos\kappa L)\sin(\psi\alpha+\psi\beta-\phi_\alpha-\phi_\beta)+(\omega_{21}^2+\omega_{22}^2)r^2R_\beta^{-1}X^\beta\sin(2\psi-\phi_\beta+\beta\psi)=0, \tag{B.8}$$

where replacements for X, R_α, R_β, ϕ_α and ϕ_β are the same as for the fractional Kelvin–Voigt model. One should now multiply Eqs. (B.5) and (B.6) with $\sin 4\psi$ and $\cos 4\psi$, respectively, and subtract one from another to eliminate the term with r^4. Then the same equations should be multiplied again with $\sin -\phi_\alpha-\phi_\beta+\alpha\psi+\beta\psi$ and $\sin -\phi_\alpha-\phi_\beta+\alpha\psi+\beta\psi$ and subtracted one from another to eliminate the last terms in equations. The same procedure is repeated for Eqs. (B.7) and (B.8). After taking into account some trigonometric identities, one obtains two equations in terms of r^2 for the Maxwell PC model as:

$$r^2=-\frac{2\omega_{11}^2\omega_{22}^2(1-\cos\kappa L)R_\alpha^{-1}R_\beta^{-1}X^{\alpha+\beta}\sin(\theta_\alpha+\theta_\beta)}{(\omega_{11}^2+\omega_{12}^2)R_\alpha^{-1}X^\alpha\sin\theta_\alpha+(\omega_{21}^2+\omega_{22}^2)R_\beta^{-1}X^\beta\sin\theta_\beta}$$

$$r^2=-\frac{(\omega_{11}^2+\omega_{12}^2)R_\alpha^{-1}X^\alpha\sin\theta_\beta+(\omega_{21}^2+\omega_{22}^2)R_\beta^{-1}X^\beta\sin\theta_\alpha}{\sin(\theta_\alpha+\theta_\beta)}$$

and for the Maxwell AM model as

$$r^2=-\frac{2\omega_{11}^2\omega_{22}^2(1-\cos\kappa L)R_\alpha^{-1}R_\beta^{-1}X^{\alpha+\beta}\sin(\theta_\alpha+\theta_\beta)}{2\omega_{11}^2R_\alpha^{-1}X^\alpha(1-\cos\kappa L)\sin\theta_\alpha+(\omega_{21}^2+\omega_{22}^2)R_\beta^{-1}X^\beta\sin\theta_\beta},$$

$$r^2=-\frac{2\omega_{11}^2R_\alpha^{-1}X^\alpha(1-\cos\kappa L)\sin\theta_\beta+(\omega_{21}^2+\omega_{22}^2)R_\beta^{-1}X^\beta\sin\theta_\alpha}{\sin(\theta_\alpha+\theta_\beta)},$$

where $\theta_\alpha=\phi_\alpha-\alpha\psi+2\psi$ and $\theta_\beta=\phi_\beta-\beta\psi+2\psi$. In the same manner as above, by equating the equations for r^2 of the fractional Maxwell PC or AM models, one can obtain the corresponding transcendent equation with two zeros defining the unknown X for fixed values of angle ψ, which are denoted as X_s, $s=1,2$.

References

1. M. I. Hussein, M. J. Leamy, M. Ruzzene, *Dynamics of phononic materials and structures: Historical origins, recent progress, and future outlook*, App. Mech. Rev. **66** (2014), 040802.
2. D. Krattiger, M. I. Hussein, *Generalized Bloch mode synthesis for accelerated calculation of elastic band structures*, J. Comput. Phys. **357** (2018), 183–205.
3. J. Lou, L. He, J. Yang, S. Kitipornchai, H. Wu, *Wave propagation in viscoelastic phononic crystal rods with internal resonators*, Appl. Acoust. **141** (2018), 382–392.
4. P. G. Martinsson, A. B. Movchan, *Vibrations of lattice structures and phononic band gaps*, Q. J. Mech. Appl. Math. **56** (2003), 45–64.
5. K. H. Matlack, S. Krödel, A. Bauhofer, D. Chiara, *Advanced structured composites as novel phononic crystals and acoustic metamaterials*, in: C. Ralph, M. Silberstein, P. Thakre, R. Singh, (ed.), *Mechanics of Composite and Multi-functional Materials*, Springer, Cham, 2016, 155–162.
6. J. Lee, J. P. Singer, E. L. Thomas, *Micro-/nanostructured mechanical metamaterials*, Adv. Mater. **24** (2012), 4782–4810.
7. P. S. Y. E. Kwon, E. Kwon, Y. Y. Kim, *Wave dispersion tailoring in an elastic waveguide by phononic crystals*, Adv. Mater. **103** (2013), 151901.
8. W. Gang, Y. Liu, J. Wen, D. Yu, *Visco-elastic effects on wave dispersion in three-phase acoustic metamaterials*, J. Mech. Phys. Solids. **96** (2016), 29–47.
9. B. Merheb, P. A. Deymier, M. Jain, M. Aloshyna-Lesuffleur, S. Mohanty, A. Berker, R. W. Greger, *Elastic and viscoelastic effects in rubber/air acoustic band gap structures: A theoretical and experimental study*, J. App. Phys. **104** (2008), 064913.
10. Y-F. Wang, Y-S. Wang, V. Laude, *Wave propagation in two-dimensional viscoelastic metamaterials*, Phys. Rev. B **92** (2015), 104110.
11. X. Zhu, S. Zhong, H. Zhao, *Band gap structures for viscoelastic phononic crystals based on numerical and experimental investigation*, App. Acoust. **106** (2016), 93–104.
12. W. Gang, Y. Liu, J. Wen, D. Yu, *Formation mechanism of the low-frequency locally resonant band gap in the two-dimensional ternary phononic crystals*, Chinese Phys. **15** (2006), 407.
13. M. I. Hussein, M. J. Frazier, *Metadamping: An emergent phenomenon in dissipative metamaterials*, J. Sound. Vib. **332** (2013), 4767–4774.
14. M. I. Hussein, *Theory of damped Bloch waves in elastic media*, Phys. Rev. B **80** (2009), 212301.
15. M. I. Hussein, M. J. Frazier, *Band structure of phononic crystals with general damping*, J. App. Phys. **108** (2010), 093506.
16. Y. Y. Chen, M. V. Barnhart, J. K. Chen, G. K. Hu, C. T. Sun, G. L. Huang, *Dissipative elastic metamaterials for broadband wave mitigation at subwavelength scale*, Compos. Struct. **136** (2016), 358–371.
17. M. A. Lewińska, V. G. Kouznetsova, J. A. W. van Dommelen, A. O. Krushynska, M. G. D. Geers, *The attenuation performance of locally resonant acoustic metamaterials based on generalised viscoelastic modelling*, Int. J. Solids Struct. **126** (2017), 163–174.
18. S. Alamri, B. Li, K. T. Tan, *Dynamic load mitigation using dissipative elastic metamaterials with multiple Maxwell-type oscillators*, J. Appl. Phys. **123** (2018), 095111.
19. Y. Liu, D. Yu, H. Zhao, J. Wen, X. Wen, *Theoretical study of two-dimensional phononic crystals with viscoelasticity based on fractional derivative models*, J. Phys. D Appl. Phys. **41** (2008), 065503.
20. Y. A. Rossikhin, M. V. Shitikova, *Application of fractional calculus for dynamic problems of solid mechanics: novel trends and recent results*, Appl. Mech. Rev. **63** (2010), 010801.
21. M. J. Frazier, M. I. Hussein, *Generalized Bloch's theorem for viscous metamaterials: Dispersion and effective properties based on frequencies and wavenumbers that are simultaneously complex*, C. R. Phys. **17** (2016), 565–577.
22. D. DePauw, H. Al Ba'ba'a, M. Nouh, *Metadamping and energy dissipation enhancement via hybrid phononic resonators*, Extreme Mech. Lett. **18** (2018), 36–44.

23. Y. A. Rossikhin, M. V. Shitikova, *A new method for solving dynamic problems of fractional derivative viscoelasticity*, Int. J. Eng. Sci. **39** (2001), 149–176.
24. Y. A. Rossikhin, *Reflections on two parallel ways in the progress of fractional calculus in mechanics of solids*, Appl. Mech. Rev. **63** (2010), 010701.
25. T. M. Atanacković, S. Pilipović, B. Stanković, D. Zorica, *Fractional calculus with applications in mechanics: wave propagation, impact and variational principles*, John Wiley & Sons, City, 2014.
26. S. Holm, S. P. Näsholm, *A causal and fractional all-frequency wave equation for lossy media*, J. Acoust. Soc. Am. **130** (2011), 2195–2202.
27. Y. Wang, *A causal and fractional all-frequency wave equation for lossy media*, J. Acoust. Soc. Am. **204** (2015), 1216–1221.
28. C. Liu, C. Reina, *Broadband locally resonant metamaterials with graded hierarchical architecture*, J. Appl. Phys. **123** (2018), 095108.

ПРИСТУП БАЗИРАН НА ФРАКЦИОНОМ РАЧУНУ ЗА ОПИСИВАЊЕ МЕТА-ПРИГУШЕЊА У ФОНОНСКИМ КРИСТАЛИМА И АКУСТИЧНИМ МЕТАМАТЕРИЈАЛИМА

Резиме. У последњој деценији, истраживања на тему фононских и акустичних материјала и структура су у успону као резултат примене резултата истраживања из теоријске физике у разним областима инжењерства. Главна карактеристика фононског медијума је периодичност која произилази из периодичности материјалних фаза, геометрије или граничних услова са особинама пропагације таласа анализираним преко зонске структуре (подручја забрањених и допуштених фреквенција пропагације таласа). За добијање наведених карактеристика и дисперзних релација резонантих метаматеријала са вискозним пригушењем у литертури се најчешће примењује Блохова теорема. У овом раду предложен је нов приступ за теоријску анализу модела фононских кристала и акустичних метаматеријала са фракционим пригушењем уведеним преко фракционог Келвин-Војтовог и Максвеловог модела. У нумеричкој анализи, резултати добијени за предложене моделе са пригушењем су упоређени са резултатима добијеним за еквивалентне еластичне моделе фононских кристала и локално резонантних акустичних метаматеријала и показана је знатна разлика у вредностима дисперзних криви у ова два случаја. Показано је да је фракциони Максвелов модел погоднији за описивање ефекта пригушења због могућности фитовања два параметра, реда фракционог извода и параметра пригушења.

Mathematical Institute SANU
Belgrade
Serbia
mcajic@mi.sanu.ac.rs

(Received 17.01.2020.)
(Available online 25.05.2020.)
(corresponding author)

Swansea University
Swansea
United Kingdom;
Mathematical Institute SANU
Belgrade
Serbia
danilok@mi.sanu.ac.rs, danilo.karlicic@swansea.ac.uk

Mathematical Institute SANU
Belgrade
Serbia
stepa.paunovic@gmail.com

Swansea University
Swansea
United Kingdom
s.adhikari@swansea.ac.uk